

Muonic Processes in Solid Hydrogen Films

BY

PAUL EVAN KNOWLES

B.Sc.H., ACADIA UNIVERSITY, 1990

A DISSERTATION SUBMITTED IN PARTIAL FULFILMENT
OF THE REQUIREMENTS FOR THE DEGREE OF
DOCTOR OF PHILOSOPHY
IN THE DEPARTMENT OF PHYSICS AND ASTRONOMY.

WE ACCEPT THIS DISSERTATION AS CONFORMING
TO THE REQUIRED STANDARD.
JANUARY 17th, 1996

Dr. G. A. Beer, *Co-supervisor (Department of Physics)*

Dr. G. M. Marshall, *Co-supervisor (Department of Physics)*

Dr. M. Lefebvre, *Department Member (Department of Physics)*

Dr. R. Sobiech, *Department Member (Department of Physics)*

Dr. S. K. Stobart, *Outside Member (Department of Chemistry)*

Dr. K. M. Crowe, *External Examiner (Department of Physics, Berkeley)*

© PAUL EVAN KNOWLES, 1996,
UNIVERSITY OF VICTORIA.

All rights reserved. Dissertation may not be reproduced in whole or in part, by mimeograph or other means, without the permission of the author.

Co-Supervisors: Dr. G. A. Beer, Dr. G. M. Marshall.

Abstract

Muon catalyzed fusion, a process known ever since the introduction of muons to bubble chambers, is a field which still poses unanswered questions. The multitude of physical conditions for the many possible combinations of different hydrogen isotopes have made the field rich in physics, but sometimes difficult to study experimentally. This dissertation presents a measurement of muon catalyzed fusion reactions in deuterium at 3 K, and introduces a new technique based on the use of solid layers of hydrogen maintained in vacuum to allow experimentation with muonic deuterium and muonic tritium atoms.

Examiners:

Dr. G. A. Beer, *Co-supervisor (Department of Physics)*

Dr. G. M. Marshall, *Co-supervisor (Department of Physics)*

Dr. M. Lefebvre, *Department Member (Department of Physics)*

Dr. R. Sobie, *Department Member (Department of Physics)*

Dr. S. R. Stobart, *Outside Member (Department of Chemistry)*

Dr. K. M. Crowe, *External Examiner (Department of Physics, Berkeley)*

Table of Contents

Abstract	ii
Table of Contents	iii
List of Tables	iv
List of Figures	vi
Acknowledgements	ix
Frontispiece	x
1 Introduction	1
1.1 Reactions of Muons in Hydrogen Isotope Mixtures	1
1.1.1 Muon Capture and Transfer	2
1.1.2 Muonic Atom Interactions	3
1.1.3 Muonic Molecules	5
1.1.4 Nuclear Physics	6
1.1.5 Fusion Cycling and Sticking	7
1.2 Experiments with Hydrogen Layers	7
2 Theory Specific to Muonic Deuterium	10
2.1 Solid Deuterium	10
2.1.1 Molecular Formation	10
2.1.2 Spin Exchange Rate	13
2.1.3 Branching Ratio	16
2.1.4 Effects of the Solid State	17
2.1.5 Reaction Rates and Physical Measurements	18
2.1.6 Time Spectra of Fusion Products	20
2.1.7 Comparison With Other Kinetic Models	21
2.2 Emission Physics	21
2.2.1 Cross Sections and Attenuation Measurements	22
2.2.2 Emission Time Parameters	24
3 Experimental Equipment	28
3.1 Muons and Beam Lines	28
3.2 The Cryogenic Target	29
3.2.1 Design and Construction	29
3.2.2 The Cryostat	30
3.2.3 The Deposition System	33
3.2.4 The Target Vacuum System	36

	iv
3.2.5	The Gas Mixing System 38
3.2.6	Operation 39
3.3	Electronics and Data Collection 40
3.3.1	The Trigger 40
3.4	Detectors 43
3.4.1	Neutron Detection 45
3.4.2	Silicon Charged-Particle Detectors 47
3.4.3	Germanium Counter 48
3.4.4	Multi-Wire Proportional Chambers and Imaging 48
4	Data 51
4.1	Solid Deuterium Runs 51
4.2	Muonic Deuterium Emission Data 53
4.3	Histogram Collection 53
5	Analysis 54
5.1	Detector Calibration and Efficiencies 54
5.1.1	Neutron Detector 54
5.1.2	Silicon Detector 57
5.2	Solid Deuterium 59
5.2.1	Neutron Spectra 59
5.2.2	Proton Spectra 64
5.2.3	Fit Methods 70
5.2.4	Fit Results 71
5.3	Emitted Muonic Deuterium 77
5.3.1	Proton Energy Spectra Features 77
5.3.2	Proton Time Spectra Features 85
5.4	Monte Carlo Simulations 91
5.4.1	Monte Carlo of the Solid Deuterium 92
5.4.2	Monte Carlo of the Emission Process 96
6	Discussion and Conclusions 100
6.1	Results for Solid Deuterium 100
6.2	Results from the Emission Measurements 104
6.3	Improvements and Future Directions 105
	Bibliography 107
A	Notation for the Rates 111
B	Matrix Exponentiation 114
C	Resolution Functions 116
D	Calibration Data 117
D.1	Neutron Detector Calibration 117
D.2	Silicon Detector Calibration 119
E	List of Abbreviations 121

List of Tables

I	Summary of the $x\mu y$ Coulomb bound state energies, in electron volts, for different isotopic forms of the muonic hydrogen molecule. Note the weakly bound $(J, \nu) = (1, 1)$ states for the $d\mu d$ and $d\mu t$ molecules. The table is taken from Ref. [18].	6
II	Table of the fusion reactions between hydrogen isotopes.	7
III	Rotational energy levels for $D_2(\nu_i=0)$ and $[(d\mu d)dee]_{(\nu_f=7)}$ in meV. The E_0 value is with respect to the $D + D$ dissociation threshold. The table is taken from Ref. [23].	12
IV	Summary table for the solid deuterium data of August 1992.	51
V	Summary table of the emission data. SET stands for Standard Emission Target, which in this case was 1040 Tl of deuterium doped protium mixture with $c_d = 10^{-3}$. The SET was deposited on the upstream foil; the downstream was bare. The \oplus is used to indicate that the D_2 layer was frozen on the surface in the increments summed in parenthesis. The column labeled S_{i2} refers to the position of the second silicon detector, and is important since the 'in' position interfered with the solid angle of the side-mounted detector.	52
VI	Table of standard values passed to the fitting routine. The fits to the data required the first six values but were unable to return any measurements of those values. The last four values in the table were required in the kinetics, but were also measurable depending on the number of available free parameters.	71
VII	The kinetics values resulting from fits to the thick deuterium neutron spectrum.	72
VIII	The values resulting from fits to the proton time spectra taken from both the thick (1560 Tl) and thin (312 Tl) deuterium targets.	74
IX	The kinetics values resulting from fits to the thick (1560 Tl) deuterium spectrum for both neutron and proton data. The value of $\tilde{\lambda}_{\frac{1}{2}} (= 0.044 \mu s^{-1})$ was fixed during the fit.	75
X	The kinetics values resulting from fits to the thick deuterium spectrum for both neutron and proton data, with the goal of measuring $\tilde{\lambda}_{\frac{1}{2}}$	75
XI	A comparison of the Gaussian (G) and asymmetric (A) fit values for the key parameters of yield and centroid. The confidence levels (cl) for the fits are also given (probability of obtaining a worse value of χ^2/dof).	81

XII	The effective interaction length derived from fits to the yield data for fixed values of the direct stop contribution A_2 [cf. Eq. (5.13)]. The addition of the small variation in the layer thickness has a dominant effect on the evaluation of the fits.	82
XIII	Values of the linear coefficients derived from fits to the data in Fig. 5.3.5. The fits are reasonably insensitive to the uncertainty in the layer thickness. The uncertainty in the slope does not include the systematic uncertainty in the conversion from Tl to $\mu\text{g} \cdot \text{cm}^{-2}$	83
XIV	A summary of the results from the figure of merit cut on the energy selection window. The values in the table denote energy channel number, and the column headings are explained in the text.	87
XV	A summary of the fits of a single exponential to the emission data.	88
XVI	The time signal background fit results. The time zero, t_0 , and detector resolution, σ , are accurately defined by this fit. The curiously low χ^2/dof , partially due to the uncertainty in the scaling factor in Eq. (5.18), implies that the uncertainties in the data are somehow overestimated by a factor of 2. The t_0 and σ values are independent of global scaling in the uncertainties.	88
XVII	A summary of the attempts to fit the toy model to the emission data. The Gaussian amplitude referred to a Gaussian centered at the t_0 value; δt was an offset allowing the proton signal growth to begin later than the t_0 value; bgs was a multiplier on the amount of background τ_{sbg} permitted in the fit; and $acorr$ is the relative ratio of the amplitudes of the two exponentials. A number presented without an uncertainty was held fixed during the fit.	89
XVIII	A summary of the attempts to fit the toy model to the Monte Carlo simulations.	99
XIX	The kinetics values resulting from the simultaneous fits to both neutron and proton data from solid deuterium. The value of $\tilde{\lambda}_{\frac{1}{2}}$ ($= 0.044 \mu\text{s}^{-1}$) was fixed for all of the fits.	100
XX	The measurement of $\tilde{\lambda}_{\frac{1}{2}}$ from the simultaneous fits of neutron and proton spectra.	100
XXI	Gamma source photon energies, Compton energies, and equivalent detector energies at the half-maximum intensity point. Energies are given in keV. Note that ^{60}Co has two lines of equal strength which are averaged to get the detector response.	118
XXII	Centroid values and widths from the FEB92 pulser data. The Fit 0 value indicates where the scale begins, the σ measures the intrinsic width of the electronics.	119
XXIII	Abbreviations used in the thesis.	121

List of Figures

1.1.1	A simplified schematic showing the permitted states which can form when a negative muon is introduced into a mixture of the three isotopes of hydrogen.	2
1.1.2	A plot of the theoretical elastic scattering cross sections $\sigma(\mu d + ^1\text{H}_2)$, $\sigma(\mu t + ^1\text{H}_2)$, which exhibit the Ramsauer-Townsend effect.	4
1.2.1	Schematic target arrangement for time-of-flight reactions using the layered solid hydrogen target method.	8
2.1.1	The detailed energy level structure of the molecular formation process in D_2 .	11
2.1.2	The formation rate of the $d\mu d$ complex as a function of incident μd energy for the two lowest rotational states of D_2 .	13
2.1.3	The formation rate of the $d\mu d$ complex as a function of incident $\mu d_{\frac{3}{2}}$ energy for different D_2 target temperatures.	14
2.1.4	The temperature dependence of the $\tilde{\lambda}_{\frac{1}{2}}$ and $\tilde{\lambda}_{\frac{3}{2}}$ effective formation rates in liquid and gas.	15
2.1.5	The measured values of the spin exchange rate, $\tilde{\lambda}_{\frac{3}{2}\frac{1}{2}}$, as a function of the target temperature.	16
2.1.6	The two-node approximation kinetics model of the muonic states in deuterium.	19
2.2.1	A very simplified picture of the emission process.	21
2.2.2	A plot of the various reaction rates for a μd as a function of the μd lab energy.	23
2.2.3	The simplified (toy) model of the emission time spectrum.	24
3.1.1	The layout of the M20-B secondary beam line at TRIUMF.	28
3.2.1	A schematic view of the cryostat portion of the target system.	31
3.2.2	A cross section of a thermal load attachment point.	32
3.2.3	A view of the gas deposition diffuser.	34
3.2.4	A vertical-section view of the gas diffusion assembly.	35
3.2.5	A perspective view of the assembled target system.	37
3.2.6	Layout of the gas mixing and deposition system in use during the operation of the target.	39
3.3.1	The schematic electronics diagram for the trigger circuit.	41
3.3.2	The timing schematic for the trigger circuit.	42
3.4.1	A top view of the detectors and their positions with respect to the target.	44
3.4.2	The electronics diagram for the neutron circuit.	45
3.4.3	The electronics diagram for the delayed electron circuit.	47
3.4.4	The electronics diagram for the silicon circuit.	48
3.4.5	The electronics diagram for the germanium circuit.	49

3.4.6	The electronics diagram for the wire-chamber circuit.	50
5.1.1	A PSD verses pulse height density plot taken from the solid deuterium data.	55
5.1.2	A pictorial representation of the biasing of the del_e events caused by the closing of the global event gate EVG.	56
5.1.3	A plot of the measured time zero position versus energy channel extracted from the fusion time spectra in thick deuterium (time walk).	59
5.2.1	A plot of counts versus energy pulse height for singles and del_e neutrons.	60
5.2.2	A plot of neutron time spectra for singles and del_e data.	61
5.2.3	A plot of the silicon energy spectrum for solid deuterium.	64
5.2.4	A plot of the silicon energy spectrum for the bare gold target.	65
5.2.5	Plots of the silicon time spectrum from the l and h regions in thick solid deuterium.	66
5.2.6	Plots of the time spectrum for the l and h regions from the bare target.	67
5.2.7	Plots of the silicon time spectrum for the l and h regions from the thick protium target.	68
5.2.8	Neutron time data, and the fit to the data.	73
5.2.9	Proton time data for the thick deuterium, and the fit to the data.	74
5.3.1	The energy spectra taken from the emission targets in the region containing the 3 MeV proton signal for times $t > 20$ ns.	78
5.3.2	A comparison of the Gaussian and asymmetric fits to the 24 Tl surface layer energy spectrum.	79
5.3.3	A plot of the curves fitted to the energy distributions for the successive surface layers.	80
5.3.4	A plot of the yield as a function of the surface layer thickness.	82
5.3.5	A plot of the energy distribution centroids as a function of the surface layer thickness.	83
5.3.6	A plot of the signal and background curves found by the fit to the 24 Tl ($154 \mu\text{g} \cdot \text{cm}^{-2}$) data.	85
5.3.7	The τ_s and τ_{sbg} data, along with the best fit to the data.	90
5.4.1	A plot of the neutron time distribution predicted by the Monte Carlo using the nuclear scattering cross sections.	92
5.4.2	A plot of the response function for reactions in solid D_2	93
5.4.3	A comparison of the measured and simulated fusion neutron spectra in D_2 for the Monte Carlo of Adamczak.	95
5.4.4	The Monte Carlo simulation of the proton yield as a function of the surface layer thickness.	97
5.4.5	Time distributions of the protons produced by emitted muonic deuterium as predicted by the Monte Carlo.	98
6.1.1	A graph of molecular formation rates as measured in solid, liquid and gas, and calculations for liquid and gas.	101
6.1.2	The comparison of $\tilde{\lambda}_{\frac{3}{2}}^{\frac{1}{2}}$ to previously measured values.	102
D.1.1	The ^{60}Co photon energy spectrum as seen by the neutron detector.	117
D.1.2	A plot of the equivalent light output for NE-213 scintillator.	118
D.2.1	The pulser and americium spectrum in the silicon detector for the FEB92 run period.	120

Acknowledgements

This page has gone through several incarnations, each one containing more names than the last until now, when I finally came to realize that there are far too many to list individually. This dissertation resulted from over five years of work at Triumf and in that time the advice, help, and guidance that I have received has been immeasurable. There is a great collection of very talented people here.

Special mentions can be made to George, Glen, and Art for putting up with my constant questions, and my all too often thick-skulled approach to many of the things I've done.

Thanks go to Donald Knuth, Leslie Lamport, and the world user community of $\text{T}_{\text{E}}\text{X}$ and $\text{L}^{\text{A}}\text{T}_{\text{E}}\text{X} 2_{\epsilon}$ for the development of such powerful document preparation systems which provided me with many happy hours spent with boxes and glue getting the figure *here* rather than *there*. J.L. Chuma and the computing support group at TRIUMF deserve kudos for PHYSICA, an excellent analysis and graphing package.

Et finalement et pour toujours, un grand merci à Fanfan.

And the man clad in black and silver with a silver rose upon him? He would like to think that he has learned something of trust, that he has washed his eyes in some clear spring, that he has polished an ideal or two. Nevermind. He may still be only a smart-mouthed meddler, skilled mainly in the minor art of survival, biind as ever the c'ungeons knew him to the finer shades of irony. Never mind, let it go, let it be. I may never be pleased with him.

Corwin, Prince of Amber

THE COURTS OF CHAOS

Roger Zelazny, 1978.

Chapter 1

Introduction

For the last fifty years it has been known that the introduction of a negative muon into a mixture of the three isotopes of hydrogen (known as protium, deuterium, and tritium, and differing only in the number of neutrons) can lead to fusion reactions between the hydrogen nuclei, a process called muon catalyzed fusion or μCF . The intricately connected molecular, atomic, and nuclear processes that occur have taken many years to identify and offer a richness of physics in both theoretical and experimental domains.

This thesis is based on data collected for μCF in deuterium under experimental conditions not previously explored. The different conditions are accessible due to the novel target system developed for the experiment. The cycling parameters for muon catalyzed fusion in the solid phase of deuterium at low temperature (3 K) have been measured.

In addition, measurements made with beams of μd atoms have illustrated a new technique which can reveal information on the scattering cross sections of muonic atoms.

Chapter 1 gives a general introduction to the types of physics involved in the field of muonic atoms, and introduces the idea of the solid layered targets. Chapter 2 will give the theory specific to muonic deuterium and the present analysis. The remaining chapters will detail the apparatus, the data, the analysis, and the results.

1.1 Reactions of Muons in Hydrogen Isotope Mixtures

Figure 1.1.1 shows, in a simplified and schematic way, the multitude of states which can form when a negative muon is introduced into a mixture of the three hydrogen isotopes. The individual states result from the different possible reactions of muon capture, transfer, muonic molecular formation, and nuclear fusion. Each of the reactions will be explained in more depth in the following sections to provide a general explanation of the physics associated with the muonic hydrogen processes. The experimental work presented herein focuses closely on only one aspect of the diagram, the molecular formation of $\text{d}/\mu\text{d}$ starting with a μd atom and a D_2 molecule.

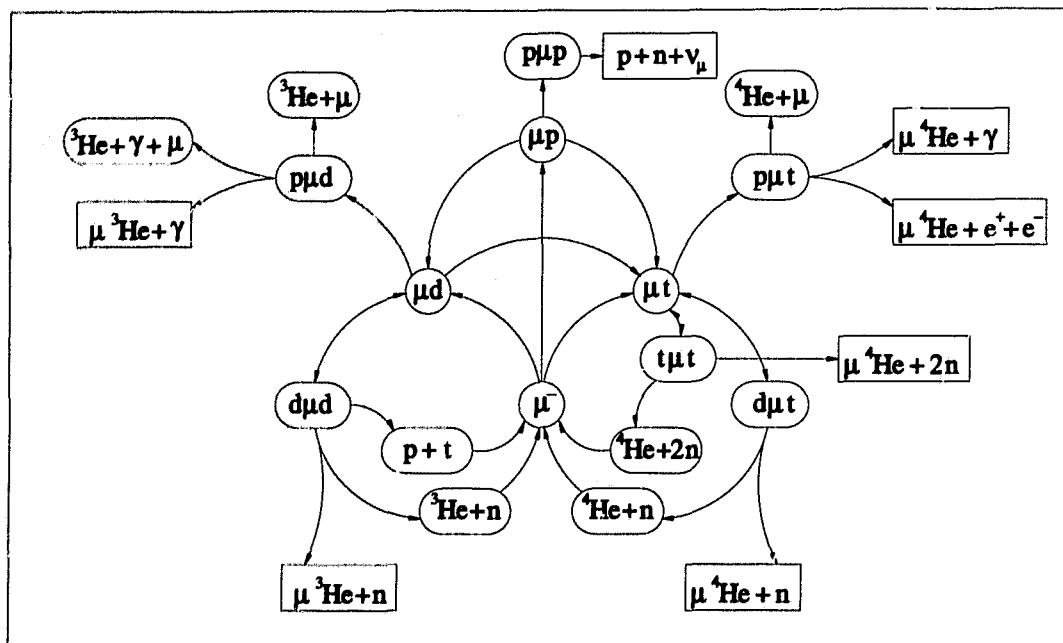


Figure 1.1.1: A simplified schematic showing the permitted states which can form when a negative muon is introduced into a mixture of the three isotopes of hydrogen.

1.1.1 Muon Capture and Transfer

The muon lifetime is long ($2.2 \mu\text{s}$) compared to the time scale of atomic and simple molecular processes. At close to 207 times the mass of the electron, a negative muon bound to a nucleus will form an atomic orbit structure similar to the one derived in any introductory quantum text¹ for the electron orbiting a nucleus, but with an increase in the energy scale of the order of the mass ratio quoted above. Likewise, the size scale of the muonic atom will be reduced by the same factor.

A negative muon introduced into matter slows and captures on an atom in a characteristic time of picoseconds. The atomic capture occurs when the muon interacts with a bound electron transferring to it an energy greater than its ionization potential and taking over the electron's physical orbit [1]. By comparing muon and electron bound state energies it is easily shown that the muon is captured in an orbital with a principal quantum number similar to the square root of the mass ratio times the initial electron level. Since $n = 1$ for the electrons in ground state hydrogen the muon initially captures in an atomic orbital with $n \approx \sqrt{m_\mu/m_e} \approx 14$. The subsequent deexcitation of the muonic atom occurs via Stark, Auger, scattering, radiative, and transfer processes, which occur on the 100 ps time scale in hydrogen. After the capture and deexcitation, the muonic atom will have a

¹The general wave function for a charged particle in a Coulomb potential can be written as $\Phi_{nlm}(t) = R_{nl}Y_l^m \exp(-iE_n t)$ where the energy of a given level n is $E_n = -\frac{m_1 m_2}{(m_1 + m_2)} \frac{Z^2 e^4}{2n^2 \hbar^2}$. Note the dependence of the energy on the reduced mass.

kinetic energy which implies an effective temperature.

The transfer process, often called Coulomb deexcitation, provides a source of acceleration for the muonic atom. The reaction is $\mu x_{n_i} + x \rightarrow \mu x_{n_f} + x$ with $n_i > n_f$. Since the final state contains only the massive particles, they share the energy released in the $n_i \rightarrow n_f$ transition. The energy released in this form of deexcitation provides an acceleration mechanism for the muonic atom, often allowing the atom to reach high kinetic energies (~ 75 eV). Since the accelerating deexcitation mechanisms are in competition with the nonaccelerating deexcitation mechanisms, the final energy distribution is believed to contain both thermal and epithermal distributions of muonic atoms relative to the remaining matter. "Thermal" is used to refer to a distribution consistent with the average energy of the surrounding material. Likewise, "epithermal" is used to refer to the muonic atoms outside of that distribution. The relative populations of the distributions reflect the conditions in which the μx deexcited (i.e., in low density gas, or in liquid) since it is these conditions which determine the strength of the Coulomb deexcitation compared to the other processes. The energy distribution has been the focus of several recent experiments and calculations working with both muonic and pionic atoms [2-5].

Muonic atoms adrift in a hydrogen mixture which happens to be contaminated by other atoms with high Z are rapidly scavenged to the tightly bound high-Z systems. The study of the muon transfer from the hydrogen to the heavy nucleus is still an active area in muon physics [6]. Except in a few rare cases, the physics of μCF occurs entirely in the three isotopes of hydrogen, i.e., $Z = 1$, and thus the transfer to heavy nuclei is an unwanted process.

The reduced mass dependence of the ground state energy implies that in a mixture of hydrogen isotopes, the muon preferentially transfers to the heavier isotope. These isotopic transfer processes $\mu p + d \rightarrow \mu d + p$ and $\mu p + t \rightarrow \mu t + p$ create muonic atoms formed with kinetic energies of 43.3 and 44.5 eV respectively, an energy equivalent to thousands of degrees of thermal excitation. However, the loss of the energy to the surrounding medium is generally too rapid to allow experimentation with the hot atoms.

An important effect is the transfer of the muon to another isotope before it has reached the ground state of the initial muonic atom. Called the " q_{1S} " problem, it is relevant for the study of μCF in triple mixtures [7]. The term q_{1S} refers to the fraction of muonic atoms which actually reach the ground state ($1S$ level) before the muon is transferred to the heavier isotope. Since the rate of transfer from an excited state is generally different than the transfer from the ground state, the kinetics of the muonic processes following the transfer can be strongly affected [8].

1.1.2 Muonic Atom Interactions

The muonic atom is a small neutral entity which interacts with its surroundings via the Coulomb force. Although electrically neutral, there are induced dipole and quadrupole

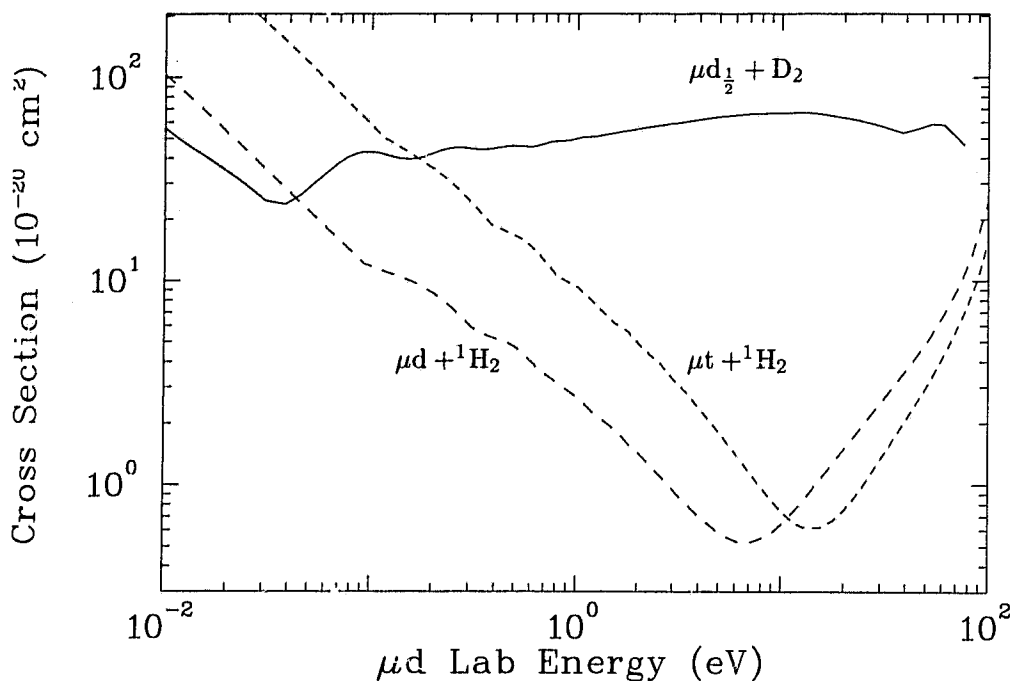


Figure 1.1.2: A plot of the theoretical elastic scattering cross sections $\sigma(\mu d + {}^1\text{H}_2)$, $\sigma(\mu t + {}^1\text{H}_2)$, which exhibit the Ramsauer-Townsend effect. A plot of the reaction $\sigma(\mu d_{\frac{1}{2}} + \text{D}_2)$ shows the comparable scattering cross section for other muonic atoms. Note the logarithmic scales.

moments associated with the atoms as they come close to charge centers.

The hyperfine structure of the muonic hydrogen atom is measured in tens of meV, the energies characteristic of hot thermal excitations ($1\text{ K} \sim 0.1\text{ meV}$). Scattering processes for a muonic atom can lead to spin realignment in the hyperfine structure, so in collections of molecules where the thermal energies are small, the collisions between the muonic atoms and the molecules tend to depopulate the highest energy hyperfine states. For each type of muonic atom there are several competing scattering processes such as the spin realignment, isotope exchange and molecular formation (see below). Calculation of the cross sections for these processes has been undertaken in the past several years [9-15].

Of some interest is the Ramsauer-Townsend scattering minimum which occurs for μd and μt incident on ${}^1\text{H}_2$ (Fig. 1.1.2). The scattering cross section undergoes a dramatic drop in magnitude over the incident energy range of a few electron volts. In essence, μd and μt in the correct energy range can travel macroscopic distances in protium without undergoing a large number of interactions. Direct evidence of the effect has been photographed in bubble chambers [16].

1.1.3 Muonic Molecules

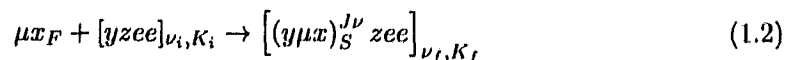
In analogy with hydrogen atoms and molecules, one would expect a muon to form a bound state between two hydrogen nuclei, and so it does. Such muo-molecules² offer an interesting connection between particle physics and molecular physics. For nuclei with $Z > 2$ the atomic bound state energy is so large that the muon cannot participate in molecular processes.

The molecular formation proceeds from a muonic hydrogen atom via two possible mechanisms. The first is the capture of the muonic atom on one nucleus of a hydrogen molecule and subsequent Auger deexcitation of the system. The reaction is written as



where x, y, and z can be any of the different isotopes of hydrogen.

A second process, a resonance mechanism first proposed by Vesman [17], is a curiously fortuitous effect that depends on the energy levels of all the involved bound states. The system has a six-body final state, with a multitude of possible spin, vibrational, and orbital angular momentum values. The existence of a loosely bound state of the $(y\mu x)$ (see Table I) implies that only a small amount of energy is liberated upon its formation. The excess energy of the system, the energy liberated in molecular formation plus the incident μx energy, can be absorbed in the excitation of rotational and vibrational states, $(\nu_f K_f)$, of the full six body system. Since the dissociation energy of the electronic bonds in a hydrogen molecule is of the order of 5 eV, the muonic system has to be weakly bound indeed on the 100 eV scale characteristic of the muonic molecular bound states. The resonance in the formation cross section occurs when the incident energy of the μx_F in hyperfine state F is such that the total initial energy of the system exactly matches the energy of some set of final state excitation parameters.



The notation J , ν , and S , refers to the orbital angular momentum, vibrational quantum number, and total angular momentum of the $y\mu x$ molecular system, while the $\nu_{i,f}, K_{i,f}$ refer to the vibrational quantum number and rotational quantum number of the full system.

The resonant formation process proceeds at least one order of magnitude faster than the Auger process and often up to three or four orders of magnitude faster, which is of great advantage to muon catalyzed fusion since the number of fusions is directly dependent on the number of muonic molecules. The excited state formed by the resonance mechanism has several paths open for deexcitation; radiative, Auger and collisional processes can all lead to a stably bound muonic molecule, while the reverse process, called back decay,

²The traditional name for muonic molecules is "meso-molecules", a holdover from the days when muons were yet another intermediate mass particle. The "muo-" prefix is a modernization; "Molecules" has been proposed, but support for the term is limited.

(J, ν)	$p\mu p$	$p\mu d$	$p\mu t$	$d\mu d$	$d\mu t$	$t\mu t$
(0, 0)	-253.15	-221.55	-213.84	-325.07	-319.14	-362.91
(0, 1)	---	---	---	-35.84	-34.83	-83.77
(1, 0)	-107.27	-97.50	-99.13	-226.68	-232.47	-289.14
(1, 1)	---	---	---	-1.9749	-0.6603	-45.21
(2, 0)	---	---	---	-86.45	-102.65	-172.65
(3, 0)	---	---	---	---	---	-48.70

Table I: Summary of the $x\mu y$ Coulomb bound state energies, in electron volts, for different isotopic forms of the muonic hydrogen molecule. Note the weakly bound $(J, \nu) = (1, 1)$ states for the $d\mu d$ and $d\mu t$ molecules. The table is taken from Ref. [18].

returns the excited six body state to a muonic atom and a hydrogen molecule. The fate of a given $y\mu x$ depends on the relative rates for each process.

Table I is a summary of the Coulomb binding energy for the bound states of the $y\mu x$ molecule [18, 19]. Only the $d\mu d$ and $d\mu t$ have loosely bound states capable of participating in resonant formation. The finite nuclear charge distribution, vacuum polarization, and hyperfine interactions give corrections to the quoted values on the order of tens of meV, while relativistic, finite molecular size, and Darwin³ terms contribute at the meV level. Resonant formation is sensitive to all meV effects, so in addition to the above corrections, it becomes important to know the incident energy of the μx to understand quantitatively the resonant formation process.

The exact energy spacing of the final six body system depends on the nucleus not involved in the muonic molecule — the z in Eq. (1.2) — so the distinct reactions that fall into the category of Eq. (1.2) will have different rates.

1.1.4 Nuclear Physics

Since the muon confines the two hydrogen nuclei in close proximity, the quantum mechanical tunneling of the nuclei through the Coulomb barrier leads to fusion reactions between the nuclei. The fusion reactions in hydrogen are summarized in Table II. Thus muonic molecules can provide a method to study the strong interaction between the nuclei at very low energies since kinetic energy is not required to overcome the Coulomb barrier. The fusion rates yield information on the few nucleon systems formed via muonic molecules [20]. The total fusion rates extracted from the muon catalyzed reactions are more accurate than the extrapolations to low energy of cross sections measured in the keV region. For the reactions involving tritium, μCF often provides the only available measurements of the reactions. The total cross sections are of importance in the study of controlled thermonuclear

³As most readers will remember from relativistic quantum mechanics, the Darwin term can be derived by applying the Foldy-Wouthuysen transformation to the Dirac equation. The resulting Hamiltonian contains the Darwin term $-\frac{e}{8m^2} \nabla \cdot \vec{E}$ which is an expression of the zitterbewegung of the charged particle sampling the local structure of the electric field.

Isotopes	Products	Q-Value (MeV)	Comment
$p + p \rightarrow$	$d + e^+ + \nu_e$	0.42	Weak interaction dominated.
$p + d \rightarrow$	${}^3\text{He} + \gamma$	5.49	
$p + t \rightarrow$	${}^4\text{He} + \gamma$	19.77	
$d + d \rightarrow$	${}^3\text{He} + n$	3.27	Asymmetric Branching ratio
	$p + t$	4.03	
$d + t \rightarrow$	${}^4\text{He} + n$	17.59	
$t + t \rightarrow$	${}^4\text{He} + 2n$	11.33	

Table II: *Table of the fusion reactions between hydrogen isotopes.*

fusion, and nuclear astrophysics.

1.1.5 Fusion Cycling and Sticking

Following molecular formation and fusion, the muon is generally set free to begin the process of forming another muonic molecule again. This leads to the idea of cycling, one muon catalyzing many reactions (cf. Fig. 1.1.1). The absolute number of reactions which a single muon can catalyze is limited by two effects, either the muon decay, or is removed from the cycle by a process known as sticking.

Since the fusion reactions often produce helium, where the nucleus is doubly charged, the muon can capture into a deeply bound orbit on the helium, removing the possibility that the muon can catalyze another fusion. This is a two step process, consisting of the initial sticking of the muon to the helium after fusion, and the probability that the muon can be stripped and set free in the subsequent collisions of the muonic helium with the surrounding matter.

For the most rapid of the μCF cycles, the $d+d$ and $d+t$ reactions, the probability that the muon is lost to the sticking process is $\sim 12\%$ and $\sim 0.5\%$ respectively. Thus the upper limit on the number of fusion cycles which a muon can catalyze for the dd reaction is about 10, and in the dt reaction it is ~ 200 . The measurements of the sticking probability in the dt system have been difficult to do, and the theory has had difficulty in matching the experimental numbers [21].

1.2 Experiments with Hydrogen Layers

Nothing has been said so far concerning the form of the hydrogen in which the muon was stopped. Until recently, only liquid and gaseous, and hence homogenous, targets were used in μCF research.

A target system was developed at TRIUMF which exploited the low vapour pressure of hydrogen at low temperatures to form solid layers of hydrogen ice which were maintained in a vacuum. Because the layers were solid, it was possible to make multilayer structures where

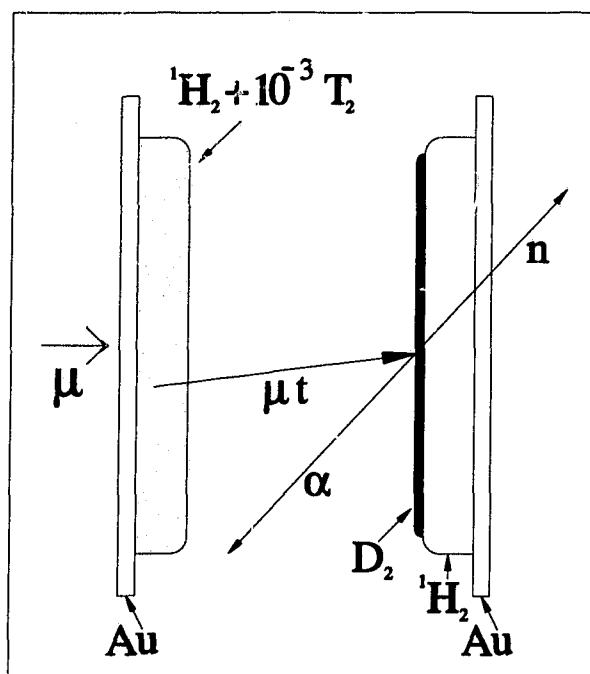


Figure 1.2.1: Schematic target arrangement for time-of-flight reactions using the layered solid hydrogen target method.

different layers had different isotope concentrations and the layers remained separate. The geometrical separation of concentrations was used to spatially confine different reactions.

Figure 1.2.1 illustrates the idea of the multilayer target. When a muon is stopped in the first layer — here composed of tritium-doped protium supported on a gold foil — the dominant reaction after the capture of the muon by a proton is the transfer of the muon to a triton. The transfer process produces a 44.5 eV μt which will proceed to interact in the layer. Because of the Ramsauer-Townsend effect, Fig. 1.1.2, the μt can escape from the first layer, since it is predominantly protium, and travel into the vacuum adjacent to the layer. When the μt reaches the second solid target, made of a thin deuterium coating on the surface of a pure protium substrate, the $d\mu t$ molecular formation reaction is possible and leads to detectable fusion products. The time between the introduction of the muon and the fusion is dominated by the μt flight time, thus it is possible to have a measure of the μt energy preceding the reactions in the deuterium layer.

During the measurements made for this work, tritium was not yet in use in the target system due to the considerable safety requirements necessary to work with radioactive gas so the experiments were done with protium and deuterium. With those two isotopes, only the $d\mu d$ muo-molecule can be resonantly formed. Two divisions in the study of muonic deuterium were made: the study of μCF in solid deuterium, a process which examined the low energy (few meV average energy) interactions, and the physics of emitted μd atoms,

which allowed measurements of processes occurring at a few eV.

For the experiments with solid deuterium, a thick layer of pure deuterium was frozen to each of the gold support foils. Muons were stopped in the layers and initiated the fusion reactions the products of which were detected. The time between the introduction of the muon and the detection of the fusion product contained information on the molecular formation leading to the fusion reaction.

The work with emitted μd atoms was done with a deuterium-doped protium layer covered with various thicknesses of pure deuterium. Unlike the time-of-flight experiment outlined above, there was no vacuum gap over which the μd had to travel, so the information on the energy of the μd prior to reacting in the thin surface layer was not measurable.

The technique of measuring the reactions of the energetic emitted muonic atoms was completely new. The first exploration of the different possible types of measurements was done to achieve the understanding necessary for further experiments. The initial measurements presented here have pointed the way toward much more extensive experimentation such as the time-of-flight measurement of the resonance structure in the $\mu t + D_2$ system as outlined above. Many of the techniques presented here have been implemented in another apparatus and used in μd emission measurements and in an attempt to generate a beam of slow negative muons [22].

Chapter 2

Theory Specific to Muonic Deuterium

The previous chapter outlined the general theory of the muon catalyzed fusion processes; the present chapter will focus on the processes specific to the experiments and analysis carried out here. Two different types of experiment were done using the target system. A measurement was made of the fusion cycle parameters in solid deuterium at low temperature. The second measurement was an exploration of the emission of μd from hydrogen layers containing a small concentration of deuterium and the subsequent fusion and scattering reactions of the epithermal muonic atoms. The rates used are explained in Appendix A, page 111.

2.1 Solid Deuterium

Pure deuterium has been well investigated for gaseous and liquid targets, see Refs. [23, 24] and references therein, where the assumption that the D_2 is not interacting with its neighbours has been used in the theoretical analysis. Although that approximation has led to generally good agreement between the theory and experiment when the deuterium is a fluid, the collective nature of the motion in crystals will certainly challenge that assumption. The data taken for this thesis from μCF in solid deuterium will yield some guidance for the understanding of the types of effects the solid phase may have on the fusion cycling.

2.1.1 Molecular Formation

In the cycling of a muon through the fusion process (cf. §2.1.5, page 18), the formation of the muonic molecule acts as the rate limiting step. Already noted is the fact that resonant formation occurs much faster than the Auger process. Calculations for the resonant and nonresonant formation rate have been made using an expansion of the potential truncated after the dipole interaction terms [25, 26]. Further refinements to include the effect of the quadrupole are being made [27, 28].

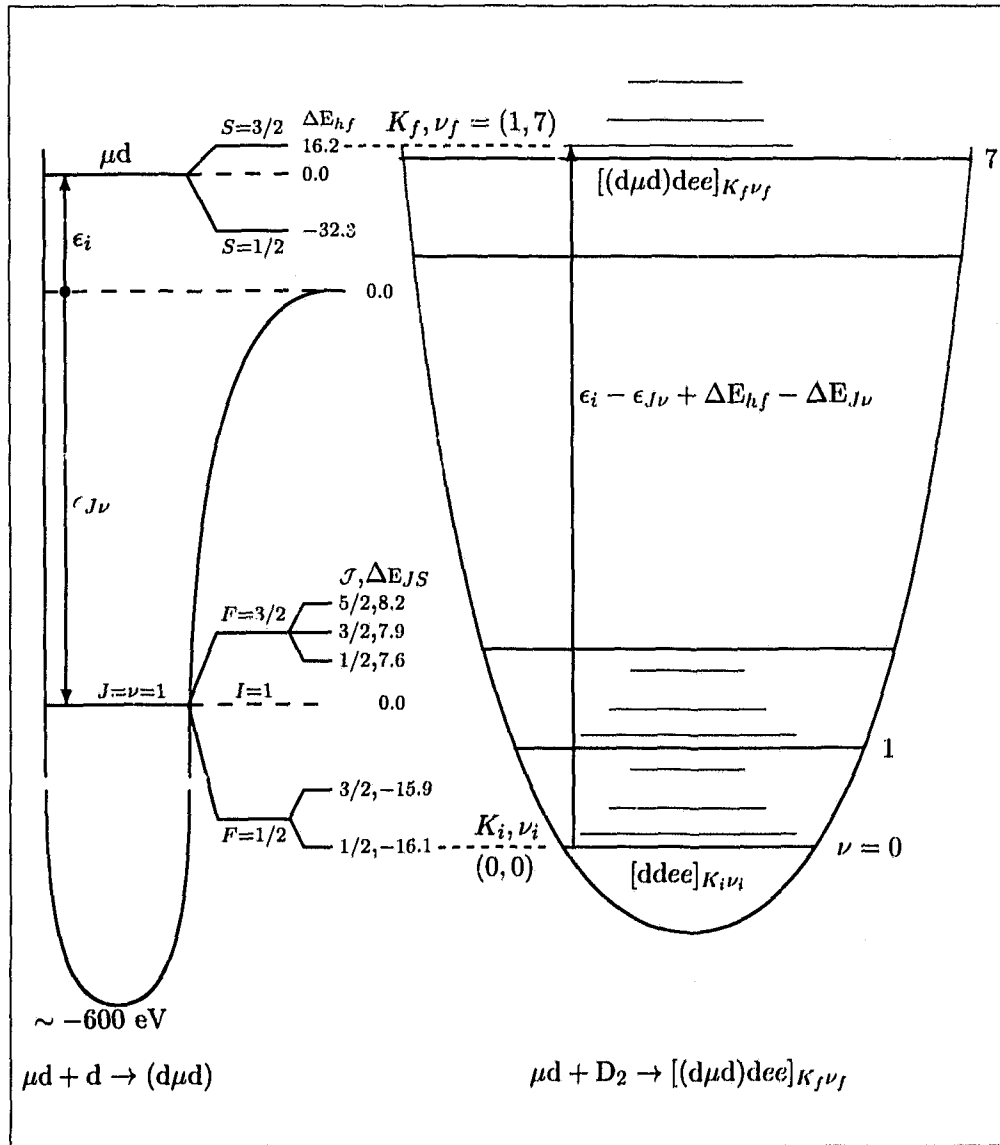


Figure 2.1.1: The detailed energy level structure of a μd_F with collision energy ϵ_i incident on a ground state D_2 compared to the bound state energies of the $d\mu d$, and a representation of the excitation spectrum of the $[(d\mu d)_{J,\nu}^S dee]_{K_f, \nu_f}$ system. The variability of ϵ_i , the collision energy, allows the overlap of initial and final levels, shown here for the molecular transition $(0, 0) \rightarrow (1, 7)$. The angular momentum level corrections, and the K, ν spacings are not to scale; the zero energy point is defined by $\epsilon_i = 0$ and an infinite separation between the μd and the D_2 . The figures are adapted from Refs. [18, 29], and ΔE corrections are given in mcV.

K	$D_2(\nu=0)$	$[(d\mu d)dee]_{K,\nu=7}$
	$E_0 = -4556.215$	$E_0 = -4584.382$
0	0.000	2026.007
1	7.412	2030.393
2	22.202	2039.150
3	44.303	2052.244
4	73.614	2069.628
5	110.005	2091.236
6	153.315	2116.992
7	203.358	2146.303
8	259.924	2180.566
9	322.782	2218.163

Table III: Rotational energy levels for $D_2(\nu_i=0)$ and $[(d\mu d)dee]_{(\nu_f=7)}$ in meV. The E_0 value is with respect to the $D + D$ dissociation threshold. The table is taken from Ref. [23].

The energy of the six body final state, that state being an excitation of a rotational and vibrational state of the molecular complex $[(d\mu d)_{J,\nu}^S dee]_{K_f,\nu_f}$, must contain all of the initial energy not only of the hyperfine structure, but also of the collisional energy between the μd and the D_2 (see Fig. 2.1.1). This requirement leads to large contributions to the formation rate for collisional energies which make the total energy of the final system identical to a molecular rovibrational state. The spacing of vibrational levels of hydrogen molecules is much like a harmonic oscillator with roughly 300 meV between levels. The rotational levels have an energy of approximately $J(J+1) \times 3.7$ meV [30]. More exact values are presented in Table III.

Calculations of the formation rates which can be compared to experiment proceed over several steps. The first step has been outlined in Fig. 2.1.1, that being the calculation of the rate as a function of incident energy ϵ_i for a single well defined initial state of the D_2 molecule. Then, for all of the possible initial states of the D_2 molecule, similar calculations must be performed. Figure 2.1.2 illustrates the difference in the formation rates between the ground state with angular momentum of zero and the first rotational level. In addition to the formation rate, the effective stabilization of the complex leading to fusion has to be considered, and this probability factored into the calculated rate [cf. Eqs. (2.2) and (A.2)].

The next effect to consider is the thermal motion of the target D_2 molecules which has the effect of smearing what was initially taken as a well defined collision energy of the μd and effectively turning it into a distribution. Figure 2.1.3 (page 14) illustrates that this effect rapidly removes any sensitivity to the individual resonances, even at low temperatures such as 30 K. As the temperature of the target changes, so does the distribution of excited states in the D_2 thus necessitating the inclusion of the many possible initial and final states already calculated.

Finally, the calculations which can be compared to experiment make assumptions

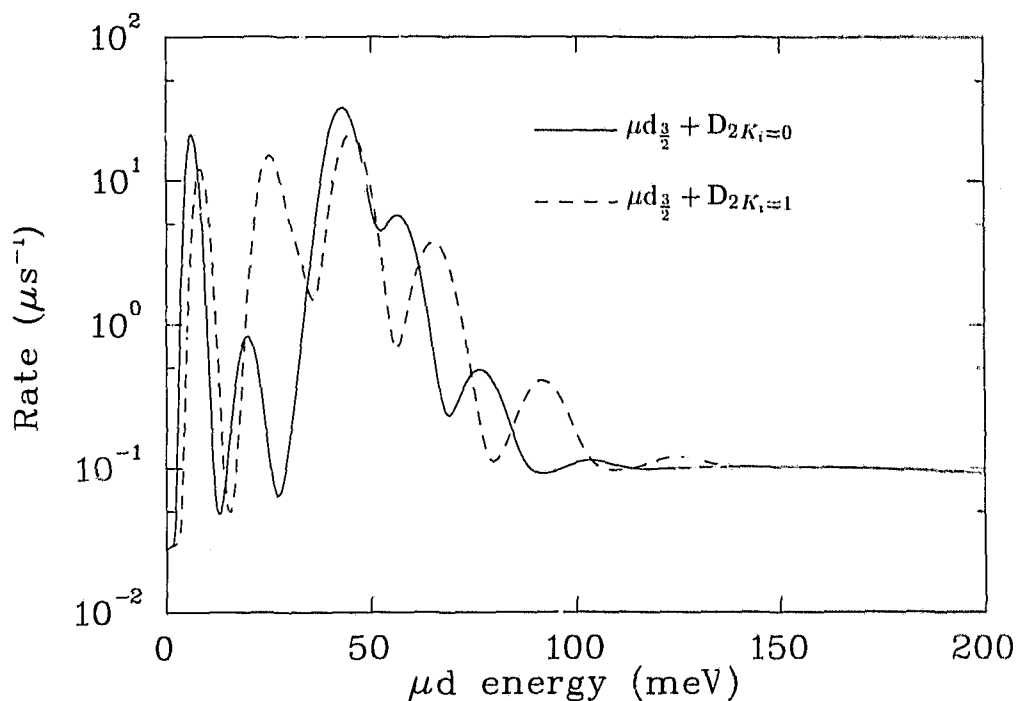


Figure 2.1.2: The formation rate of the $d\mu d$ complex as a function of incident μd energy for the two lowest rotational states of D_2 . The rate has been multiplied by the probability that the formed $d\mu d$ will fuse. Note the increase which occurs in the rate as the incident μd crosses the energy thresholds necessary to excite higher rotational bands in the final six body complex. Note: $50 \text{ meV} \approx 600 \text{ K}$.

concerning the energy distribution of the μd atoms in the D_2 target. This distribution, which is determined by the initial energy at which the μd was formed and the subsequent energy loss processes, is convoluted with the reaction rates at the appropriate temperature to produce an overall temperature dependent rate shown in Fig. 2.1.4. The agreement between theory, which predicts a rapid thermalization of the μd , and experiments in liquid and gas targets is good; results of present measurements in solids do not agree with the predictions as will be discussed later.

2.1.2 Spin Exchange Rate

The energy difference between the two hyperfine states of the μd is 48.5 meV, and this energy is readily given up to processes which depopulate the upper spin state.

There is a disagreement between theory and experiment for the hyperfine transition rate $\tilde{\lambda}_{\frac{3}{2}\frac{1}{2}}$. As indicated in Fig. 2.1.5, the shape of the temperature dependence is modelled by the theory, but the absolute rate is too high. Given the agreement between the calculated and measured formation rates (Fig. 2.1.4) and the accuracy in the calculations for the scattering reactions (which are expected to be correct to 10%), the discrepancy is curious.

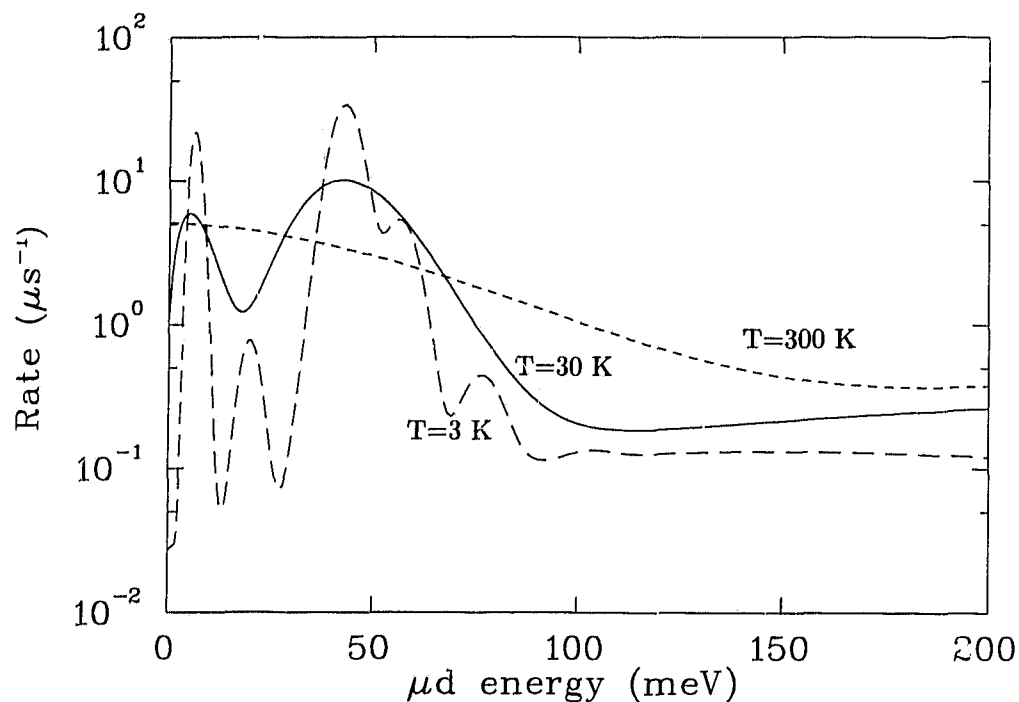
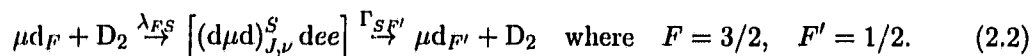


Figure 2.1.3: The formation rate of the $d\mu d$ complex as a function of incident $\mu d_{3/2}$ energy for different D_2 target temperatures. As the target D_2 temperature increases, the smearing effect removes the detailed structure of the resonances. Note: $50 \text{ meV} \approx 600 \text{ K}$.

The theoretical rate is composed of two parts, the ordinary scattering spin flip reaction



and a contribution coming from the resonant formation and decay¹ of a $d\mu d$ molecular complex via the reaction



The good agreement, Fig. 2.1.4, between measurement and theory for the formation rates leading to fusion *implies* that there is a good understanding of the matrix elements for the formation, and hence the time reversed decay reaction². The scattering reactions rely on the well understood adiabatic representation of the Coulomb three-body problem, so it is surprising that the theory predicts rates roughly 35% higher than the measured values. It is possible to scale the two contributions to the total rate separately by assuming that the shape of the curve results mainly from the back decay, and the contribution of

¹Although the reaction is really a resonance in the scattering cross section, the common name for the process is *back decay*. The term may be used here on occasion with the understanding that it is a shorthand way of talking about the resonance scattering channel.

²In fact, the decay rate $\Gamma_{SF'}$ is calculated and detailed balance used to get λ_{FS} .

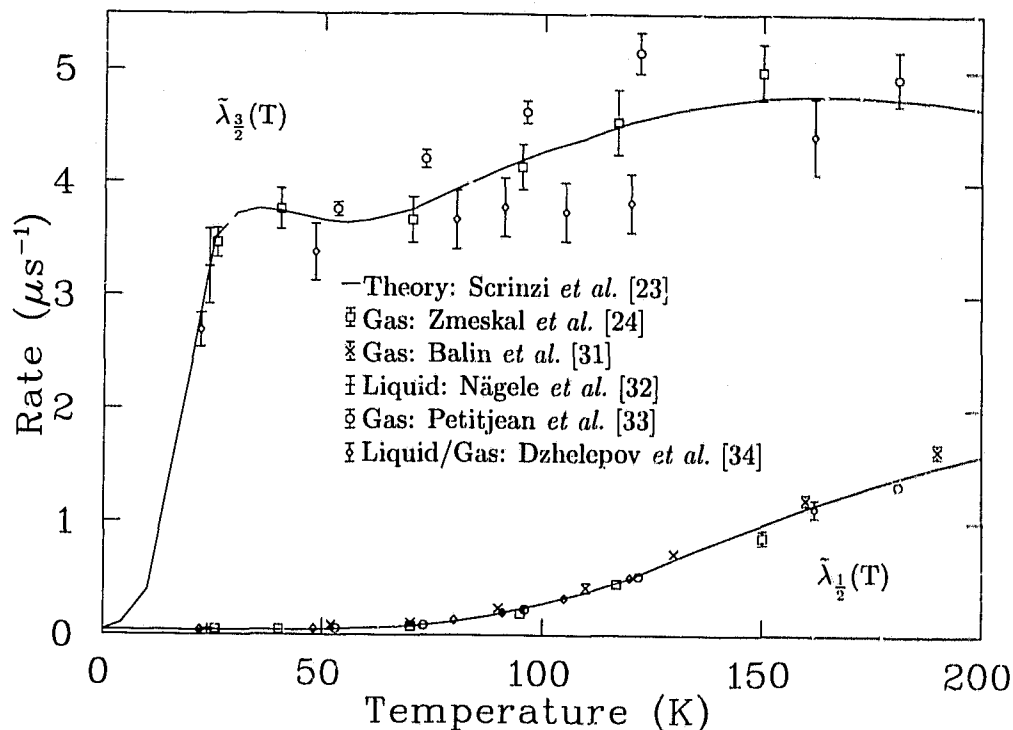


Figure 2.1.4: The temperature dependence of the $\bar{\lambda}_{1/2}$ and $\bar{\lambda}_{3/2}$ effective formation rates in liquid and gas. Note that 1 meV corresponds to roughly 10 K when comparing this graph with Figs. 2.1.2 and 2.1.3.

direct scattering makes up the remainder [23]. Such analysis predicts that the back decay is overestimated by about 10% and the direct scattering by about 45%.

If the resonance scattering contribution to the spin flip rate is considered to be correct, then the source of the disagreement is in the calculated scattering cross sections for the reactions represented in Eq. (2.1). Calculations have been carried out by several groups and the results are in agreement [12, 14]. Further refinements to the calculations for the scattering cross sections are underway, but there is no indication that they will result in agreement with the experimental results [35, 36].

It has been suggested that a reduction in the magnitude of the formation matrix element, $|t_{if}|^2$, would be sufficient to remove the discrepancy. Calculations first made in the dipole approximation, when extended to include the quadrupole term, have provided a mechanism for the reduction [27, 28].

It has been pointed out that the composition of the effective rates reduces the sensitivity of the molecular formation rate to the matrix element [39]; in essence the molecular formation rate has one factor of $|t_{if}|^2$ (contained in λ_{FS}) in the numerator, and one in the denominator (contained in Γ_{SF}) and thus the sensitivity to $|t_{if}|^2$ is decreased. The effective spin flip rate, in contrast, has two factors of $|t_{if}|^2$ in the numerator and one in the denominator leading to a larger sensitivity to the value of the matrix element [cf. Eq. (A.2)]

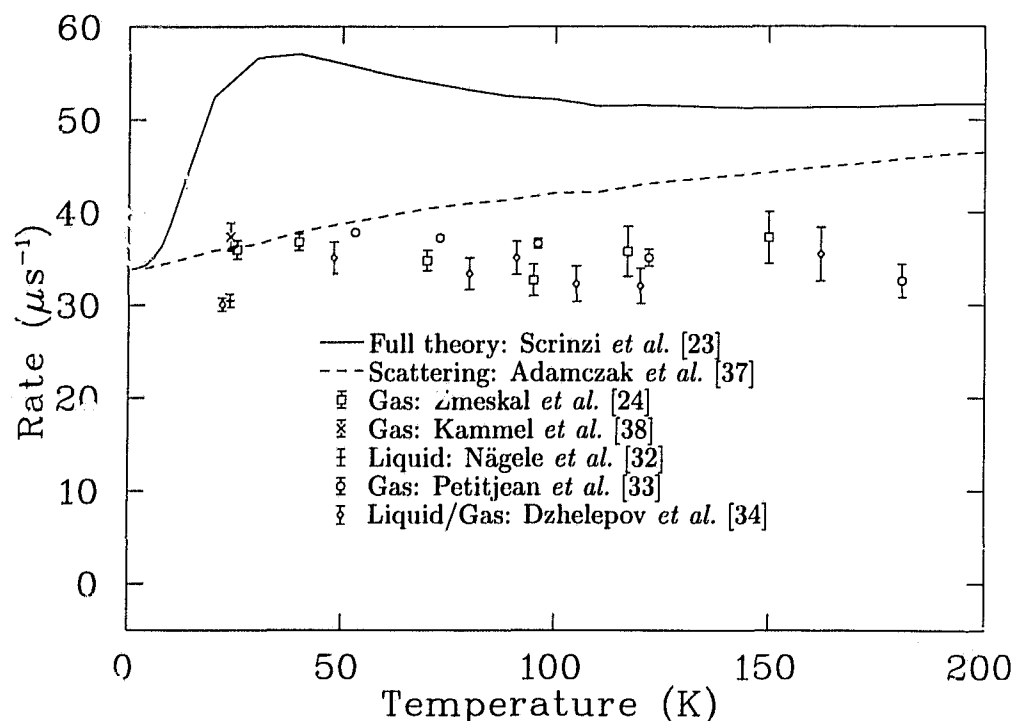


Figure 2.1.5: The measured values of the spin exchange rate, $\bar{\lambda}_{\frac{3}{2}\frac{1}{2}}$, as a function of the target temperature. Also shown are the direct spin flip scattering reaction (small even dashes) and the full prediction for the spin flip rate (solid line). The theoretical prediction is easily 35% too large.

and Eq. (A.2) in Appendix A, page 111]. The quality of fit between the data and the theory of molecular formation, Fig. 2.1.4, can be maintained for a range of matrix elements by small changes in other parameters used in calculating the rate. It is possible that a smaller matrix element can lead to agreement with both the formation rate and the spin exchange rate, but this has yet to be demonstrated.

The reverse process, $\bar{\lambda}_{\frac{1}{2}\frac{3}{2}}$, has an energy threshold of 48.5 meV and is strongly suppressed at lower temperatures. In the atomic cross section calculation, the reaction is forbidden for an incident energy less than the threshold, however, for the case where the target nucleus is contained in a molecule with molecular degrees of freedom, energy can transfer from the molecule to the reaction so that the sharp threshold is blurred [40].

2.1.3 Branching Ratio

In the scattering of polarized deuterons by a deuterium target, it was noticed that the branching ratio for the two reactions $d+d \rightarrow p+t$ and $d+d \rightarrow n+{}^3\text{He}$ was not equal [41]. The experiment, done with deuterons between 13 and 485 keV incident energy, was analyzed to extract the low energy asymmetries in the s wave and p wave interactions. Since then, two measurements using μCF in pure deuterium have accurately shown that the

p wave interaction produces neutrons for 58.2(7)% [42] and 58.0(5)% [24] of the reactions [cf. Eq. (A.1), page 112].

The asymmetry has been attributed to charge symmetry breaking in the strong force. However, a calculation has been done using an essentially charge-independent R-matrix method which has predicted a branching ratio in favour of 58.8% neutron production in the p wave case and 47.0% in the s wave case, in good agreement with the experimental measurements [43]. The calculation requires the two interacting deuterons to be treated as four interacting isospin- $\frac{1}{2}$ particles and not simply as two isospin-0 particles. In this way, it is possible for the Coulomb corrections to the interaction to add a small isospin-1 component to the dd wave function. This component can then couple to the outgoing wave functions and allow the asymmetric transitions.

The μ CF reaction in deuterium is unique since the resonantly formed $d\mu d$ is in a pure p wave state. The formed $d\mu d$ *very* rarely deexcite to a molecular s wave state since a change of nuclear spin alignment is required in the deexcitation transition to preserve the symmetry of the identical particles. The interactions which can cause the p-s transition are not coupled to the nuclear spin transition unless very small relativistic corrections are included and hence the transition is suppressed. Fusion occurs purely from the p wave state making it possible to extract the p wave branching ratio and hence the asymmetry at a very low interaction energy.

For the nonresonantly formed $d\mu d$, the fusion occurs from either an s wave or p wave state, depending on the bound state chosen in the Auger formation (cf. Table I, page 6). The observable branching ratio is then made up of weighted contributions from both s and p wave branching ratios (see the definition of β_F on page 113).

2.1.4 Effects of the Solid State

The experiments carried out for this work were the first to examine the fusion cycling at very low temperatures, and in the solid state. Since the examination of the theory of fusion under these conditions has only recently begun, there is very little *a priori* information available. Because of this, the modelling of the fusion process in gases and liquids will be used, testing its ability to fit the data. After measurements are made, it may be necessary to reinterpret the meaning of any derived parameters.

The scattering of μd in solid D_2 has been calculated and there are large differences for low energy scattering when compared to scattering from free molecules [44]. The easiest to understand is the change in reduced mass as the μd slows in the solid. When the collision of the μd occurs at energies high above the binding energy of a D_2 in the lattice, the collision will proceed as if the D_2 were free. As the μd loses energy in each successive collisions and the energy becomes small relative to the binding of the D_2 in the lattice, the μd will begin to scatter from the entire crystal, and the huge mass of the lattice will make it difficult for the μd to lose lab energy in elastic collisions. In addition, there are

only a few available phonon modes to allow inelastic scattering for μd with meV energy (cf. Fig. 5.4.2, page 93). This effect should occur near an energy equivalent to the melting point of the crystal, and so the energy loss mechanisms for the μd are suppressed when the muonic atoms are distributed below about 30 K.

2.1.5 Reaction Rates and Physical Measurements

As with any family of reactions described by rates, the time evolution of the system can be modelled by differential equations. The solutions are then used to fit the measured data to give values for the rates. The differential equations and their study is referred to as the kinetics of the reaction. It is important to understand the kinetics since the real physical processes are linked together and the ability to measure one parameter, which often depends critically on several others, is limited by the correlations.

The physical processes are obscured by the inability to distinguish differing reactions with the same initial and final states. The effective rates are the physically measurable parameters and are thus the ones to use when fitting data; see Appendix A, page 111.

Several assumptions are made about the relative size of the rates in order to simplify the process of finding a solution. The stopping and capture processes of the muon are so fast with respect to subsequent processes, and in relation to the time resolution of the detectors, that the initial conditions of the kinetics are accurately represented by the statistical filling of μd hyperfine states. The sticking of the muon to the triton after fusion is also ignored since it occurs with a very low probability, 0.0027 [45], and the μt would form a $d\mu t$ and fuse, releasing the muon very rapidly. The use of effective rates for the molecular formation and spin flip reactions removes the dependence of the solution on the $d\mu d$ population as a function of time. The entire problem reduces to finding the time dependence of the two hyperfine populations of the μd , and hence the name *two-node approximation* for this formulation of the problem.

By considering the kinetics pictured in Fig. 2.1.6, we can extract a first-order system of linear differential equations for $N_{\frac{3}{2}}$ and $N_{\frac{1}{2}}$, the populations of the $\mu d_{\frac{3}{2}}$ and $\mu d_{\frac{1}{2}}$ respectively.

$$\frac{d}{dt} \begin{bmatrix} N_{\frac{3}{2}} \\ N_{\frac{1}{2}} \end{bmatrix} = \begin{bmatrix} -A & B \\ C & -D \end{bmatrix} \cdot \begin{bmatrix} N_{\frac{3}{2}} \\ N_{\frac{1}{2}} \end{bmatrix} \quad (2.3)$$

with initial conditions

$$\begin{bmatrix} N_{\frac{3}{2}}(t=0) \\ N_{\frac{1}{2}}(t=0) \end{bmatrix} = \begin{bmatrix} \eta_{\frac{3}{2}} \\ \eta_{\frac{1}{2}} \end{bmatrix}. \quad (2.4)$$

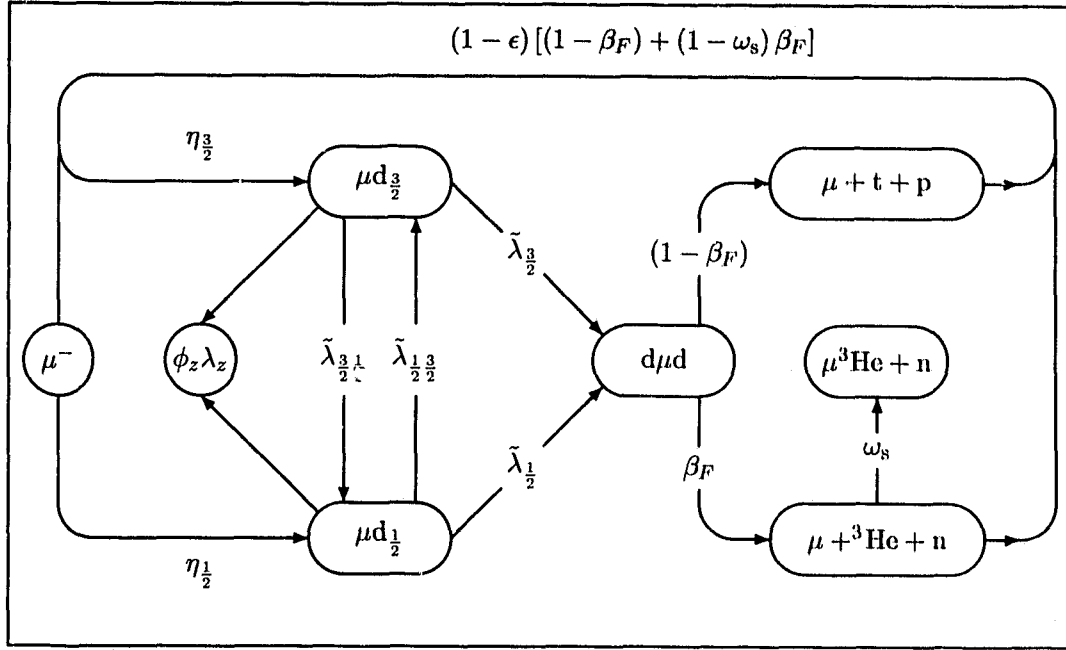


Figure 2.1.6: The two-node approximation kinetics model of the muonic states in deuterium. Effective rates are used (Appendix A, page 111) and thus only the time dependences of the $\mu d_{\frac{3}{2}}$ and $\mu d_{\frac{1}{2}}$ need to be found.

The coefficients in the matrix (all explicitly positive) are:

$$\begin{aligned}
 A &= \lambda_o + \phi_z \lambda_z + \phi \left\{ \tilde{\lambda}_{\frac{3}{2}} \left[1 - \eta_{\frac{3}{2}} (1 - \epsilon) (1 - \omega_{\frac{3}{2}}) \right] + \tilde{\lambda}_{\frac{3}{2}, \frac{1}{2}} \right\} \\
 B &= \phi \left[\tilde{\lambda}_{\frac{1}{2}} \eta_{\frac{3}{2}} (1 - \epsilon) (1 - \omega_{\frac{1}{2}}) + \tilde{\lambda}_{\frac{1}{2}, \frac{3}{2}} \right] \\
 C &= \phi \left[\tilde{\lambda}_{\frac{3}{2}} \eta_{\frac{1}{2}} (1 - \epsilon) (1 - \omega_{\frac{3}{2}}) + \tilde{\lambda}_{\frac{3}{2}, \frac{1}{2}} \right] \\
 D &= \lambda_o + \phi_z \lambda_z + \phi \left\{ \tilde{\lambda}_{\frac{1}{2}} \left[1 - \eta_{\frac{1}{2}} (1 - \epsilon) (1 - \omega_{\frac{1}{2}}) \right] + \tilde{\lambda}_{\frac{1}{2}, \frac{3}{2}} \right\}.
 \end{aligned} \tag{2.5}$$

In the above expressions ω_F is used as shorthand for the product $\omega_n \beta_F$. The rates are normalized to an atomic hydrogen density of $4.25 \times 10^{22} \text{ cm}^{-3}$; the value of ϕ relates the experimental density to the normalized value. The term $(1 - \epsilon)$ represents the probability that the fusion fragment escaped undetected. This term is necessary for fusion time spectra collected by single hit detectors which stop taking data as soon as a single event is detected. For detectors capable of detecting multiple hits, setting $(1 - \epsilon)$ to 1 (i.e., $\epsilon = 0$) will give the correct expressions.

The formal solution can be obtained by integrating Eq. (2.3) and using Eq. (2.4):

$$\vec{N}(t) = \exp \left\{ \begin{bmatrix} -A & B \\ C & -D \end{bmatrix} \cdot t \right\} \cdot \vec{N}(t=0).$$

The algorithm for the exponentiation of the matrix is straightforward (see Appendix B,

page 114) and results in the following expressions for the two hyperfine populations:

$$N_{\frac{3}{2}}(t) = \frac{1}{L_{\frac{3}{2}} - L_{\frac{1}{2}}} \left\{ \left[\eta_{\frac{3}{2}} (L_{\frac{3}{2}} + D) + \eta_{\frac{1}{2}} B \right] e^{L_{\frac{3}{2}} t} + \left[-\eta_{\frac{3}{2}} (L_{\frac{1}{2}} + D) - \eta_{\frac{1}{2}} B \right] e^{L_{\frac{1}{2}} t} \right\} \quad (2.6)$$

$$N_{\frac{1}{2}}(t) = \frac{1}{L_{\frac{3}{2}} - L_{\frac{1}{2}}} \left\{ \left[\eta_{\frac{3}{2}} C - \eta_{\frac{1}{2}} (L_{\frac{1}{2}} + D) \right] e^{L_{\frac{3}{2}} t} + \left[-\eta_{\frac{3}{2}} C + \eta_{\frac{1}{2}} (L_{\frac{3}{2}} + D) \right] e^{L_{\frac{1}{2}} t} \right\} \quad (2.7)$$

where the lifetimes $L_{\frac{3}{2}}$ and $L_{\frac{1}{2}}$, the eigenvalues of the rate matrix, are given by:

$$L_{\frac{3}{2}} = \frac{-1}{2} \left[(A + D) + \sqrt{(A - D)^2 + 4BC} \right] \quad (2.8)$$

$$L_{\frac{1}{2}} = \frac{-1}{2} \left[(A + D) - \sqrt{(A - D)^2 + 4BC} \right]. \quad (2.9)$$

2.1.6 Time Spectra of Fusion Products

The result of the two-node approximation is that the physically measurable parameters govern the time evolution of the two hyperfine populations $N_{\frac{1}{2}}$ and $N_{\frac{3}{2}}$. However, the time spectra measured are of the fusion fragments, either protons or neutrons, which originate from the μd hyperfine populations via molecular formation and branching to the appropriate fragment. This process is written as:

$$\dot{k} = \phi \sum_{F=\frac{1}{2}, \frac{3}{2}} \alpha_F \tilde{\lambda}_F N_F \quad (2.10)$$

where \dot{k} is either a proton or neutron time spectrum, $\tilde{\lambda}_F$ are the molecular formation rates from the populations represented by N_F , and α_F is related to the branching ratio via:

$$\alpha_F = \begin{cases} \beta_F & \text{for } k = \text{neutrons,} \\ 1 - \beta_F & \text{for } k = \text{protons.} \end{cases}$$

The time distribution of product k is thus:

$$k = \Psi_{\frac{3}{2}} e^{L_{\frac{3}{2}} t} + \Psi_{\frac{1}{2}} e^{L_{\frac{1}{2}} t}. \quad (2.11)$$

The amplitudes of the individual contributions are given explicitly as:

$$\Psi_{\frac{3}{2}} = \frac{\phi \left\{ \alpha_{\frac{3}{2}} \tilde{\lambda}_{\frac{3}{2}} \left[\eta_{\frac{3}{2}} (L_{\frac{3}{2}} + D) + \eta_{\frac{1}{2}} B \right] + \alpha_{\frac{1}{2}} \tilde{\lambda}_{\frac{1}{2}} \left[\eta_{\frac{3}{2}} C - \eta_{\frac{1}{2}} (L_{\frac{1}{2}} + D) \right] \right\}}{L_{\frac{3}{2}} - L_{\frac{1}{2}}} \quad (2.12)$$

and,

$$\Psi_{\frac{1}{2}} = \frac{\phi \left\{ \alpha_{\frac{3}{2}} \tilde{\lambda}_{\frac{3}{2}} \left[-\eta_{\frac{3}{2}} (L_{\frac{1}{2}} + D) - \eta_{\frac{1}{2}} B \right] + \alpha_{\frac{1}{2}} \tilde{\lambda}_{\frac{1}{2}} \left[-\eta_{\frac{3}{2}} C + \eta_{\frac{1}{2}} (L_{\frac{3}{2}} + D) \right] \right\}}{L_{\frac{3}{2}} - L_{\frac{1}{2}}}. \quad (2.13)$$

The amplitudes obey the relation

$$\Psi_{\frac{3}{2}} = -\Psi_{\frac{1}{2}} + \phi \left(\alpha_{\frac{3}{2}} \eta_{\frac{3}{2}} \tilde{\lambda}_{\frac{3}{2}} + \alpha_{\frac{1}{2}} \eta_{\frac{1}{2}} \tilde{\lambda}_{\frac{1}{2}} \right);$$

which is a re-expression of the amplitude of \dot{k} at time zero. The total yield of fusion particles from a single muon can be obtained by integrating Eq. (2.11) over times $[0, \infty)$ to obtain:

$$Y_k = - \left(\frac{\Psi_{\frac{3}{2}}}{L_{\frac{3}{2}}} + \frac{\Psi_{\frac{1}{2}}}{L_{\frac{1}{2}}} \right) \quad (2.14)$$

2.1.7 Comparison With Other Kinetic Models

The function represented by Eq. (2.11) was used to create a set of numbers representing the time spectrum of neutrons following fusion. That spectrum was then fit by another kinetics model, namely the approximation used in Zmeskal *et al.* [24], and the independent fitting routine recovered the input values to within 1%. This is good evidence that the above model accurately represents the two-node approximation to the dd kinetics³.

2.2 Emission Physics

The emission of μd atoms from solid protium layers containing small concentrations of deuterium is a well established phenomenon explained by the Ramsauer-Townsend effect in the scattering cross section for μd on $^1\text{H}_2$ [46-48].

The emission process for the experiment reported herein began with a relatively thick layer made from a homogenous mixture of deuterium-doped protium with the deuterium

³Thanks go to Peter Kammel for making this fit.

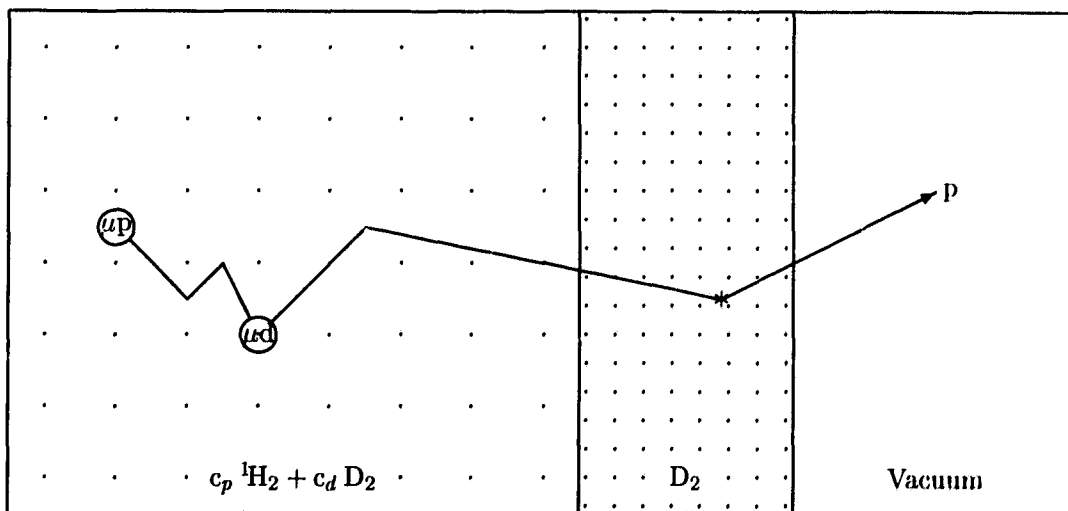


Figure 2.2.1: A very simplified picture of the emission process: a μp interacts in the emission layer, eventually losing the muon to a deuteron. The μd scatters and leaves the emission layer only to arrive in the pure deuterium layer where a molecular formation and fusion occur. The proton generated by the fusion can leave the layer and be detected.

concentration at 0.1% (a layer referred to as an *emission target* or *emission layer*). A muon stopped in such a mixture was generally captured on one of the far more numerous protons to form a μp atom (cf. Fig. 2.2.1). The μp interacted with its neighbours, scattering and losing energy, and sometimes forming a $p\mu\text{p}$ molecule which would normally last until the muon decayed since the pp fusion rate is very slow. If the μp found a deuteron, the muon transferred from the proton, due to the reduced mass effect, to produce a μd with an initial energy of 43.3 eV. The μd began to lose energy via scattering with the remaining hydrogen, and would sometimes form a $p\mu\text{d}$ molecule (The formation of a $d\mu\text{d}$ molecule in the emission layer was suppressed due to the low concentration of deuterium). However, for collision energies in the range of the Ramsauer–Townsend minimum (cf. Fig. 1.1.2, page 4) the μd traveled macroscopic distances between interactions. Since the solid layer was maintained in vacuum, it was possible for the μd to leave the layer entirely. The energy spectrum of the emitted μd was governed by the Ramsauer–Townsend minimum in the cross section.

A surface layer of pure D_2 on the emission layer changed the processes following emission. The number of μd atoms passing into the vacuum was reduced due to the large scattering cross section for the μd in the pure D_2 . In addition, the molecular formation and fusion reactions could occur and the fusion protons generated in the surface layer served as the measure of the process. The thickness of the pure D_2 layer was varied as a method to measure the $\mu\text{d} + \text{D}_2$ reactions.

An interesting comparison can be seen in Fig. 2.2.2. For a μd in the surface layer, the various reaction rates are shown in relation to each other. The graph uses only the nuclear scattering rates, i.e., no molecular or solid state effects are included, since they are sufficient to illustrate the physics processes involved. The four possible configurations of the μd initial and final hyperfine states for the scattering reaction $\mu\text{d} + \text{d} \rightarrow \mu\text{d} + \text{d}$ are shown in the figure⁴, along with the energy dependent molecular formation rates $\tilde{\lambda}_{\frac{3}{2}}$ and $\tilde{\lambda}_{\frac{1}{2}}$. For comparison, the $\mu\text{d} + \text{p}$ rate is also shown (The depression in the high energy end of the $\mu\text{d} + \text{p}$ rate is the Ramsauer–Townsend scattering minimum which allows the emission in the first place). The scattering reactions represented by λ_{11} and λ_{22} are easily two orders of magnitude larger than the $\mu\text{d} + \text{p}$ rate, so the surface layer can be thin relative to the emission layer and still allow experimentation with the $\mu\text{d} + \text{d}$ cross sections.

2.2.1 Cross Sections and Attenuation Measurements

The number of protons produced per incident muon as a function of the D_2 layer thickness contains information on the reaction cross sections. For an emission layer of fixed thickness and deuterium concentration, the yield of emitted μd atoms per incident muon will be a constant. As the thickness of the surface D_2 layer increases, more and more of the emitted

⁴The subscript "1" refers to the lower hyperfine state, "2" refers to the upper, hence the label λ_{12} represents the rate for the reaction $\mu\text{d}_{\frac{1}{2}} + \text{d} \rightarrow \mu\text{d}_{\frac{3}{2}} + \text{d}$.

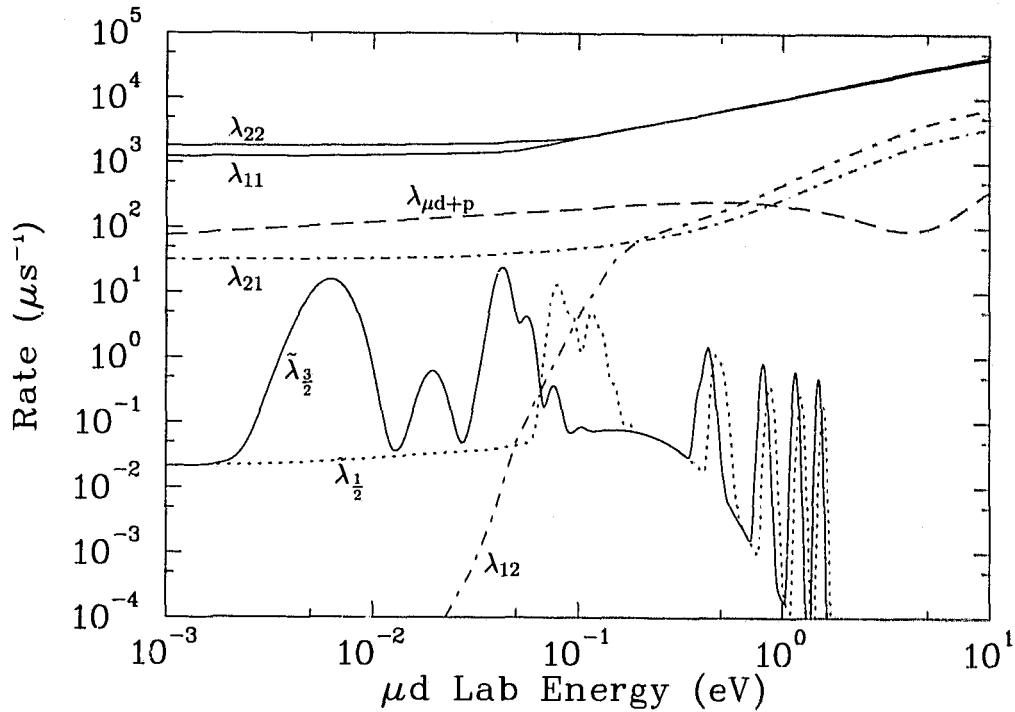


Figure 2.2.2: A plot of the various reaction rates for a μd as a function of the μd lab energy. See the text for explanation.

μd atoms will stop and interact in the layer until a saturation thickness has been reached where all of the emitted atoms are reacting. The stopping of the emitted μd atoms will be reflected in the yield of protons from the resulting fusions.

The yield of fusion protons does not result only from emitted μd atoms. Due to the stopping of muons throughout the entire target (i.e., emission layer *and* surface D_2 layer) the yield is composed of two components: protons from fusions catalyzed by muons which stopped directly in the surface D_2 layer, and the fusion protons generated by the emitted μd atoms.

The shape of the energy peak can theoretically be used to give information about the depth in the D_2 surface layer where the fusion occurs. As the fusions occur farther from the vacuum surface, the protons have more deuterium to traverse before reaching the vacuum, and hence the standard Bethe-Bloch energy loss will be larger.

For an emitted μd there will be some probability for interaction leading to fusion in the D_2 surface layer. Introducing an interaction length k allows the expected yield as a function of surface layer thickness, d , to be written as:

$$Y = A_1 (1 - e^{-d/k}) + A_2 d. \quad (2.15)$$

The factors A_1 and A_2 are for normalization, and the second term, $A_2 d$, is used to model the yield from direct stops. Since the D_2 surface layers are very thin with respect to the

momentum width, the number stopping in the layer will grow linearly with the thickness. This very simple approach to the data yields an effective interaction parameter which can eventually be compared to Monte Carlo results.

2.2.2 Emission Time Parameters

The time of the emission of the μd with respect to the arrival time of the muon is governed by the kinetics of the reactions which occur. The series of (and competition between) the rates for deexcitation to the ground state following initial muon capture, transfer to the deuteron or $p\mu p$ formation, emission or $p\mu d$ formation as well as energy loss processes must be considered. Unlike the time evolution in the homogenous solid target, the emission process contains a position dependence which makes the use of a differential equation model a less satisfying quantitative approach. Figure 2.2.3 shows a step by step representation of the processes occurring during emission and defines a simplistic model (referred to as a toy model) for a mathematical understanding of the emission time spectrum.

The processes in Fig. 2.2.3 can be used to define a set of differential equations for the number of μp and μd atoms, emitted muonic deuterium atoms, μd_e , and the number of $d\mu d$ molecules from which fusion can occur ($c_d = 1$ in the surface layer).

$$\dot{N}_{\mu p} = -(\lambda_o + \phi c_p \lambda_{p\mu p} + \phi c_d \lambda_{pd} + \phi_z \lambda_{zp}) N_{\mu p} \quad (2.16)$$

$$\dot{N}_{\mu d} = -(\lambda_o + \phi c_p \lambda_{p\mu d} + \phi c_d \lambda_{mf} + \phi_z \lambda_{zd} + \lambda_e) N_{\mu d} + \phi c_d \lambda_{pd} N_{\mu p} \quad (2.17)$$

$$\dot{N}_{\mu d_e} = -(\lambda_o + \phi_d \lambda_{mf} + \lambda_{escape}) N_{\mu d_e} + \lambda_e N_{\mu d} \quad (2.18)$$

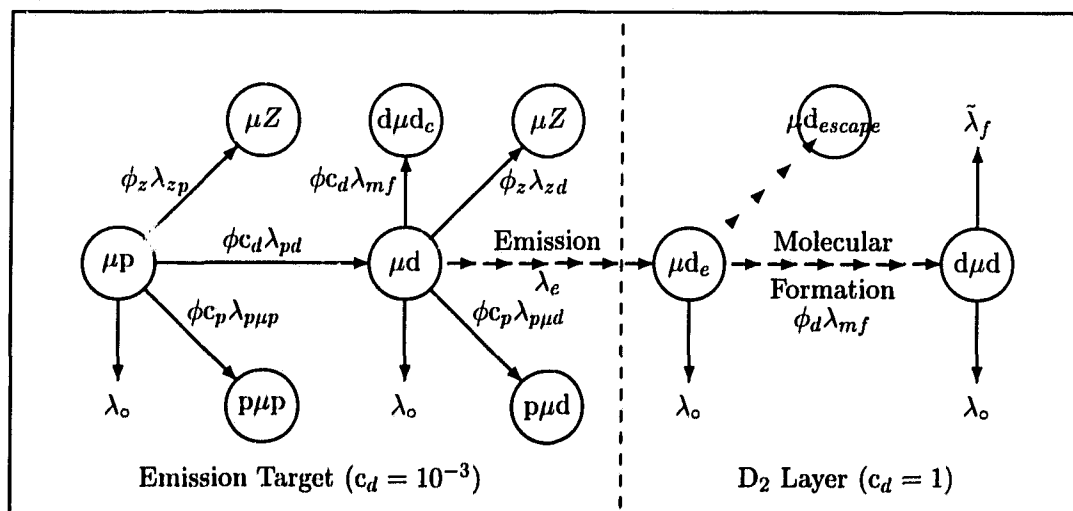


Figure 2.2.3: The simplified (toy) model of the emission time spectrum. The solid lines represent processes assumed to be adequately explained by constant rates, the dashed lines represent processes where rates are probably not as adequate.

$$\dot{N}_{d\mu d} = -(\lambda_o + \tilde{\lambda}_f) N_{d\mu d} + \phi_d \lambda_{mf} N_{\mu d e} \quad (2.19)$$

The assumption will be made that the emission, λ_e , and the molecular formation from the energetic μd , λ_{mf} , can both be represented by constant rates, and the validity of the assumption examined later. The emission process following the transfer of the muon from the proton to the deuteron is expected to be relatively fast. Given the thickness of the target layers, a nominal 0.2 mm, and a characteristic energy of a μd , for example 1 eV, then the flight time of the μd should be characteristic of the emission time and is about 20 ns. Since the μd atoms are formed with 43.3 eV, and the minimum of the Ramsauer-Townsend mechanism occurs near 7 eV, the estimate of 20 ns should be an upper limit for the time required for emission following transfer. The time required for emission is short compared to the expected time required for the transfer (50 ns), and it will affect each of the emitted μd atoms the same way. The modelling of emission as a constant rate should be a reasonable first approximation.

The $d\mu d$ molecular formation in the surface layer following the emission of a μd will generally occur after a complicated series of scattering interactions and spin exchange reactions due to the relative sizes of the rates (cf. Fig 2.2.2). As the μd interacts, the molecular formation rate competes with the scattering reactions which are changing the energy of the μd . The effective molecular formation rate, λ_{mf} , is an average over the energy dependent rate. The emission angle, which defines an effective thickness of the D_2 layer, will also affect the value of λ_{mf} simply because μd atoms emitted at an angle to the surface layer will have more path length over which the reactions with the D_2 occur. The averaging in energy of the molecular formation rate should be dominated by the relatively narrow peaks in the resonance structure and this should allow a constant rate to be used.

Since the goal of the model will be an understanding of the important parameters of the emission processes, and any measurement will be of the average of the parameters over important variables such as emission angle and energy, there is not much use in keeping account of the μd hyperfine state. Another way to look at that approximation is that the processes sampled during the emission depend on the high energy interactions of the muonic atom, ~ 1 eV, and are not sensitive to the hyperfine corrections.

Defining

$$R_1 = \lambda_o + \phi c_p \lambda_{p\mu p} + \phi c_d \lambda_{pd} + \phi_z \lambda_{zp}, \quad (2.20)$$

$$R_2 = \lambda_o + \phi c_p \lambda_{p\mu d} + \phi c_d \lambda_{mf} + \phi_z \lambda_{zd} + \lambda_e, \quad (2.21)$$

$$R_3 = \lambda_o + \phi_d \lambda_{mf} + \lambda_{escape}, \quad (2.22)$$

$$R_4 = \lambda_o + \tilde{\lambda}_f, \quad (2.23)$$

allows the solution for $N_{d\mu d}(t)$ to be written as:

$$N_{d\mu d}(t) = -\phi \lambda_{mf} \lambda_e \phi c_d \lambda_{pd} \left[\frac{e^{-R_1 t}}{(R_1 - R_2)(R_1 - R_3)(R_1 - R_4)} \right]$$

$$\begin{aligned}
& + \frac{e^{-R_2 t}}{(R_2 - R_1)(R_2 - R_3)(R_2 - R_4)} \\
& + \frac{e^{-R_3 t}}{(R_3 - R_1)(R_3 - R_2)(R_3 - R_4)} \\
& + \frac{e^{-R_4 t}}{(R_4 - R_1)(R_4 - R_2)(R_4 - R_3)} \Big] \quad (2.24)
\end{aligned}$$

The assumption has been made that $R_i - R_j \neq 0$, an effect that is not to be expected given the diverse makeup of the R_i .

The relative sizes of the R_i are important to consider. Since R_4 contains $\tilde{\lambda}_f$ ($\approx 450 \mu\text{s}^{-1}$) the $e^{-R_4 t}$ term will not only vanish quickly, it will not have a large amplitude relative to the other terms due to the three R_4 factors in the denominator. The values of R_3 will be similar to the flight time of a μd crossing the surface layer. From the arguments given earlier but considering now a surface layer with a thickness less than 5% of the emission layer thickness, R_3 will be large as well ($\sim 1000 \mu\text{s}^{-1}$ for a 1 eV μd). The third and fourth terms can be dropped⁵, after which the time spectrum of the observed protons ($= \tilde{\lambda}_f N_{d\mu\text{d}}$) approximates to:

$$\dot{p} = K \left[e^{-R_1 t} - e^{-R_2 t} \frac{(R_1 - R_3)(R_1 - R_4)}{(R_2 - R_3)(R_2 - R_4)} \right] \quad (2.25)$$

where a normalization K has been assumed.

If, as has been assumed, $R_3, R_4 \gg R_1, R_2$, then further approximations can be made yielding

$$\dot{p} = K e^{-R_1 t} \left\{ 1 - e^{-(R_2 - R_1)t} \left[1 + (R_2 - R_1) \frac{(R_3 + R_4)}{R_3 R_4} \right] \right\} \quad (2.26)$$

where it becomes clear that the sensitivity to the molecular formation and fusion rates λ_{mf} and $\tilde{\lambda}_f$ is seen as a deviation from the standard growth curve $[1 - e^{-(R_2 - R_1)t}]$. The main exponentials in the growth and decay curves are the R_1 and R_2 expressions, and they enter as the difference $-(R_2 - R_1)$. Expanding this difference and examining the terms which are found there gives:

$$-(R_2 - R_1) = -\lambda_e + \phi c_d (\lambda_{pd} - \lambda_{mf}) + \phi c_p (\lambda_{p\mu p} - \lambda_{p\mu d}) + \phi_z (\lambda_{zp} - \lambda_{zd}). \quad (2.27)$$

The molecular formation rates $\lambda_{p\mu p}$ and $\lambda_{p\mu d}$ are both nonresonant, similar in magnitude, and small, so the term in their difference can be ignored. The same should be true for the transfer to high Z contamination. This implies an interpretation of the toy model after the following re-expression of Eq. (2.24):

$$\dot{p} = K e^{-(\lambda_e + \phi c_p \lambda_{p\mu p} + \phi c_d \lambda_{pd} + \phi_z \lambda_{zp})t} \left[1 - \text{acorr} \times e^{-(\lambda_e + \phi c_d \lambda_{mf} - \phi c_d \lambda_{pd})t} \right]. \quad (2.28)$$

The growth in the model is determined by the difference between the μd creation rate from transfer, $c_d \lambda_{pd}$, and the emission and $d\mu\text{d}$ molecular formation rate inside the emission

⁵With the possible exception of a correction term required to match the initial condition $N_{d\mu\text{d}}(t=0) = 0$ during the fit to the data.

layer, $\phi c_d \lambda_{mf} + \lambda_e$. The amplitude correction, $acorr$, for the second term gives an added constraint on the difference ($R_2 - R_1$), making a clear determination of its sign. The decay rate expected after the growth factor has become unity is the R_1 value, which depends completely on processes which should be well modelled by rates, such as the molecular formation, $\lambda_{p\mu p}$, and the transfer, λ_{pd} .

A measurement of the emission parameters has been made using the layered target method [49]. A thin layer of neon was frozen to the surface of the emission layer, and emitted μd atoms quickly lost the muon to the neon via transfer. The rapidly cascade of the muon to lower energy levels then generated x rays. The time distribution of the muonic x rays was then an accurate measure of the μd arrival time at the neon, and hence emission time from the layer. The experiment was performed for three different deuterium concentrations in the emission layer and the resulting spectra analyzed by the Monte Carlo method. Values for $\lambda_{pd}(= 1.75 \pm 0.13_{\text{stat.}} \pm 0.06_{\text{syst.}} \times 10^4 \mu\text{s}^{-1})$ and $\lambda_{p\mu p}(= 3.56 \pm 0.38_{\text{stat.}} \pm 0.17_{\text{syst.}} \mu\text{s}^{-1})$ were found, but the considerable difficulty in achieving consistent agreement between the Monte Carlo predictions and the data for very small deuterium concentrations indicates that the muonic processes in solid $^1\text{H}_2$ are not well understood.

The emission experiments carried out for this work were taken from a single emission target with c_d of 0.1% which was covered by varying thicknesses of pure deuterium instead of neon. The μd atoms were emitted from the layer and either stopped in the thin surface layer or were transmitted. Transmitted μd atoms could be observed in flight by an imaging system which recorded the time and position of the muon decay electron. The μd atoms stopped in the layer would begin the fusion process and the resulting protons were detected.

Chapter 3

Experimental Equipment

The experiments described herein were done with solid hydrogen. To that end, a cryogenic target system was constructed in which gaseous mixtures of hydrogen isotopes were frozen onto a thin gold foil which was then suspended in a muon beam. The details of the target and detection systems are outlined below.

3.1 Muons and Beam Lines

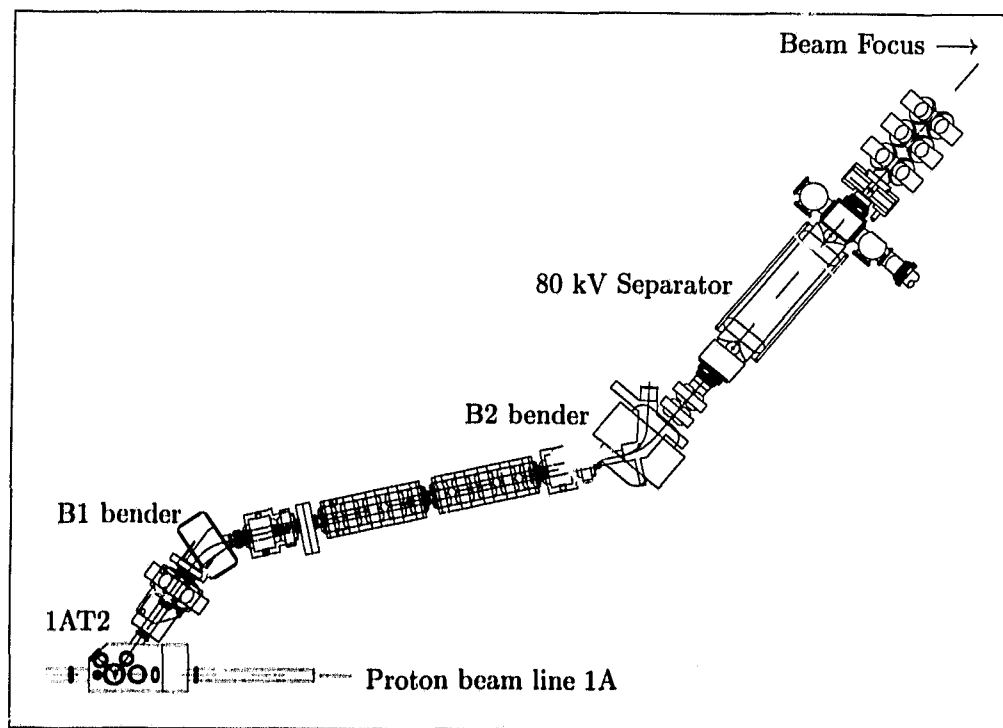


Figure 3.1.1: *The layout of the M20-B secondary beam line at TRIUMF.*

The experiment was performed at TRIUMF on the M20-B beam line (see Fig. 3.1.1). The primary 500 MeV proton beam struck a 10 cm beryllium target located at 1AT2 creating a cloud of pions which then decayed to muons. Negative muons were selected at a momentum of 26 MeV/c with a spread (bite) of $\sim 6\%$. After traversing the secondary beam line, negative muons arrived at the target in a beam spot of about 30 mm FWHM at a rate of $5.4 \times 10^3 \text{ s}^{-1}$. Although rate was a concern, the finite thickness of the solid hydrogen target defined an absolute range in which the muons could stop, hence the selection of a low momentum beam¹. The secondary beam line contained an electrostatic separator (Wein filter), consisting of parallel high voltage plates and a magnetic field perpendicular to the electric field, which was used to remove electrons from the beam. The separator changed the electron/muon ratio from 140:1 without separation to better than 0.5:1 with separation. Discrimination on the energy loss of the particle as it entered the target system reduced the electron triggers to less than 0.2%.

3.2 The Cryogenic Target

A cryogenic target system has been constructed in which gaseous mixtures of all three hydrogen isotopes have been frozen onto a thin, 65 mm diameter gold foil. The foil is cooled to 3 K while inside a 70 K radiation shield, all of which is mounted in a vacuum system maintained at 10^{-9} Torr. Stable multi-layer hydrogen targets of known uniformity and thickness have been maintained for required measurement times of up to several days.

3.2.1 Design and Construction

Problems in cryogenics, vacuum design, gas mixing, and tritium safety were addressed in the design of this target system for experimental studies of muon catalyzed fusion in hydrogen isotopes. Tritium compatibility was added to the system to allow an examination of all the μCF processes.

Fortunately the most demanding design restriction, the compatibility with tritium, was not often in conflict with the other requirements. The design had to eliminate, or reduce to a very low level, the possibility of leaks, and ensure that any release of tritium would occur in an area (or at a rate) which would not endanger personnel. Internal contamination had to be minimized to permit target disassembly, so materials such as elastomers were avoided to reduce contamination through replacement reactions of the tritium with any compound containing hydrogen.

The observed lifetime of a muonic hydrogen atom is very sensitive to contamination from heavier nuclei due to transfer reactions which compete strongly with the reactions

¹From the relation between range and momentum $R = kp^{3.5}$, it is easy to derive the range width due to momentum bite: $\delta R = 3.5kp^{3.5}(\delta p/p)$. The strong dependence of the absolute range spread on the momentum for a fixed $(\delta p/p)$ indicates why the low momentum was necessary [50].

being investigated. The all-metal vacuum system helped to achieve both cleanliness and a high vacuum, and in addition reduced the possibility of tritium contamination of internal surfaces.

3.2.2 The Cryostat

The cryogenic system was designed by a company specializing in custom refrigerators². The upper portion of the target system is represented in Fig. 3.2.1, the core of which is a modified continuous flow cryostat (detail A). A standard unit³ was extended to a length of 38 cm to reduce the thermal conductivity between the mounting flange and the cold stage. At two points along the body of the cryostat, cylindrical copper blocks (detail B) were attached to provide thermal contact points for the external target attachments (details G,I). The blocks provide conduction paths to the 3 K and the 70 K stages of the cryostat.

The cryostat functions by the continuous transfer of cold helium gas from a storage dewar through the cryostat and out through a pump. A needle valve located in the section of the transfer line inserted in the dewar restricts the flow, while the pump provides low pressure allowing the helium to vaporize and cool. The flow of cold helium gas through baffles in the cryostat provides the refrigeration. Additional steel wool installed in the helium gas flow path increased the cooling power of the 70 K thermal contact stage to 10 W.

The cryostat unit was inserted into a long closed cylindrical stainless steel tube of 500 μm wall thickness (detail C) whose upper end was welded to a 200-mm diameter knife-edge vacuum flange. The tube acted as a second barrier between the helium flow in the cryostat and the region of the vacuum system exposed to tritium. Thus the continuous flow of helium was separated from possible tritium contamination by two all-welded vacuum barriers; the tube, and the cryostat itself. Doubling the containment of the tritium strongly reduced the chance of introducing tritium contamination into the helium circuit, thereby allowing the helium to be safely recycled. The tritium barrier space, or TBS (detail D), between the outside of the cryostat and the inside of the tube was separately evacuated and monitored.

With the cryostat installed in the tube, the cylindrical copper blocks ensured a good thermal contact by providing sufficient surface area to overcome the limited thermal conductivity of the steel tube (C). Indium was used in the joints to increase the thermal conductance. Figure 3.2.2 shows the cross section of the upper contact region (section S in Fig. 3.2.1) detailing how external thermal loads (detail I, and similarly for G) were attached to the outside of the tube at the positions of the copper blocks. Stainless steel clamp rings (detail E) held together with 5/16" steel bolts, provided a high pressure on the joint (limited by the shear strength of the bolts) sufficient to conduct 10 W at 70 K.

²Quantum Technology Corporation, 1370, Alpha Lake Road, Unit 15, Whistler, B.C. Canada

³SuperTran[®], Janis Research Company, Inc. Wilmington MA, 01887-0696

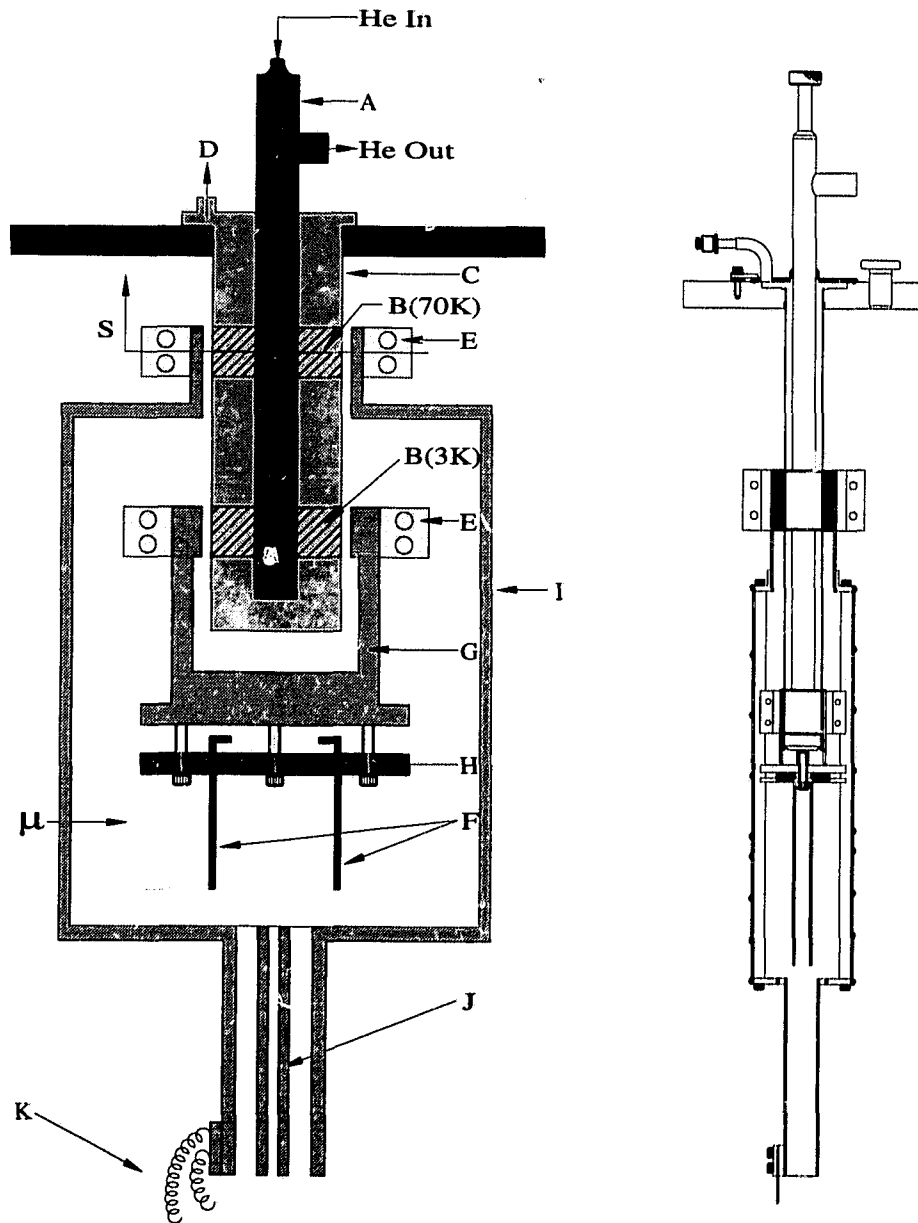


Figure 3.2.1: The figure on the left is a schematic view of the target system showing the commercial cryostat (A), heat transfer copper cylinders (B), secondary containment (C), TBS vacuum (D), attachment clamps (E), target support foils (F), 3 K cold stage (G), variable clamp (H), heat shield (I), diffuser guide rails (J), and diffuser cooling braids (K). The section S, Fig. 3.2.2, shows a cross section of the heat shield attachment. The figure on the right is a 1:6 scale drawing of the assembly.

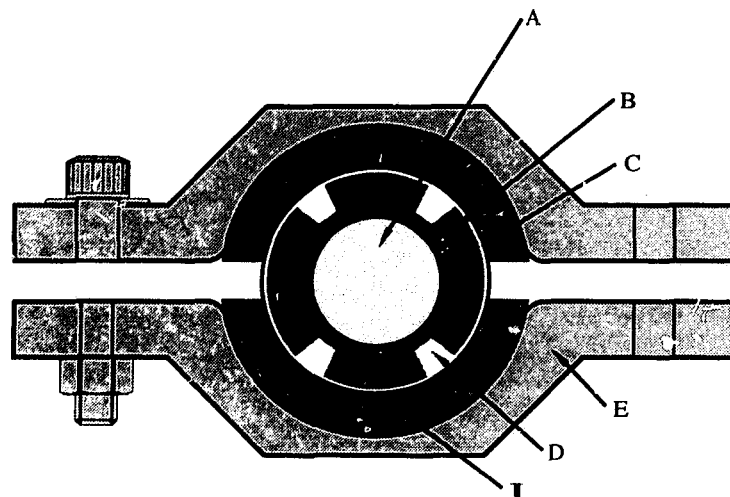


Figure 3.2.2: A cross section of a thermal load attachment point, section S from Fig. 3.2.1. The cryostat (A), heat transfer copper cylinders (B), secondary containment (C), TDS vacuum (D), and attachment clamps (E) are shown in relation to the target attachments (I, and similarly for G).

The cross section of the external attachments changed from circular, at the contact points (detail E, Fig. 3.2.1), to square, which simplified the manufacture of the target attachments and maximized the usable internal volume.

The two gold target foils $50\ \mu\text{m}$ thick and 65 mm in diameter were cold soldered, using indium, to gold-plated copper frames (detail F). The copper frames were attached to the coldest stage of the cryostat (detail G) by a clamp which allowed the spacing between the foils to be varied between 16 and 40 mm (detail H). Indium was used to ensure a good thermal contact between the removable target holding frames and the 3 K cold stage.

A radiation shield (detail I) fully surrounding the cold target stage and deposition mechanism, was attached to the cryostat at the 70 K cooling stage. The 10 W heat load due to thermal radiation from the room temperature vacuum system was thus removed by utilizing the cold exhaust gas from the 3 K cooling stage.

This radiation shield provided a convenient mount for silicon detectors used to observe reaction products originating at the targets. The shield also supported a guide rail system (detail J) for the precise insertion of the target gas deposition unit. The gas deposition unit, discussed below, was cooled via conductive copper braids (detail K).

The use of conventional super-insulation was precluded by the incompatibility between tritium and compounds containing hydrogen, such as plastics and elastomers. Instead, the low emissivity of gold plate was used to reduce the radiative heat load from all internal surfaces. The inert nature of the plating made it resistant to oxidation, and the low permeability to tritium reduced the contamination absorbed by the internal components.

Stray muons reacting with the gold produce a neutron background due to muon cap-

ture, but the neutron emission time distribution from such nuclei is prompt and well understood. The dominance of gold on all exposed surfaces ensured that only this well understood background was present.

The temperatures of parts of the target were monitored to verify proper operation. Constant-current silicon diodes were used at several places to monitor temperatures to an accuracy of a few Kelvin, while sensors specific to low temperature, such as carbon glass resistors or a CERNOX^{®4} low temperature sensor, were used on the target frames themselves where better information on target temperature was required.

Discrepancies of approximately 0.5 K were observed in measured temperatures. Thermometers mounted on the target support foils indicated a temperature different from other similar devices, as well as from that determined from the relatively well known vapour pressure of hydrogen at low temperatures. This was attributed to difficulty in thermally anchoring the thermometer leads without the use of glues and materials incompatible with tritium. Although the lack of an absolute calibration was troublesome, the thermometers reliably indicated changes in the temperature. Experience has shown that the vapour pressure of hydrogen in the vacuum system was a more useful measure of the target operation temperature and its stability — the parameters of greatest value in monitoring target performance.

3.2.3 The Deposition System

Hydrogen gas was deposited on the target foils by releasing it through the device pictured in Fig. 3.2.3. A central gold-plated copper sheet (detail L) supported two gas diffusers, independently connected to the gas supply to permit the deposition of a solid 60 mm diameter layer of hydrogen onto either of the two target foils.

Each side of the deposition system consisted of a gas supply line (detail M) from the gas mixing manifold, and a specialized chamber (detail N) designed to deposit the gas evenly on the chosen cold target with less than 0.1% deposited on the opposite target. The chamber was built from a thin cylindrical hollow disk. The diffuser end was covered with a 50 μm thick stainless steel foil containing roughly 700 holes spaced in a 1 mm square array and each of $\sim 250 \mu\text{m}$ diameter⁵. The other end of the cylinder was open, but sealed at the back by the diffuser support when the system was assembled. A section view of a diffuser is shown in Fig. 3.2.4. The gas was supplied through 0.8 mm inside diameter tubing connected to the deposition chamber. With the two diffusers mounted on the copper support the total thickness of the part inserted between the target foils was 9 mm. This limited the separation between the target foils to a minimum of about 16 mm when thermal

⁴All thermometers were acquired from LakeShore Cryotronics, Inc., Westerville, Ohio

⁵All of the holes were drilled using a hand sharpened sewing needle and a high speed drill, a technique rediscovered in a book on how to build small telescopes. The size of the holes was measured using the diffraction pattern created by the hole when illuminated by a laser.

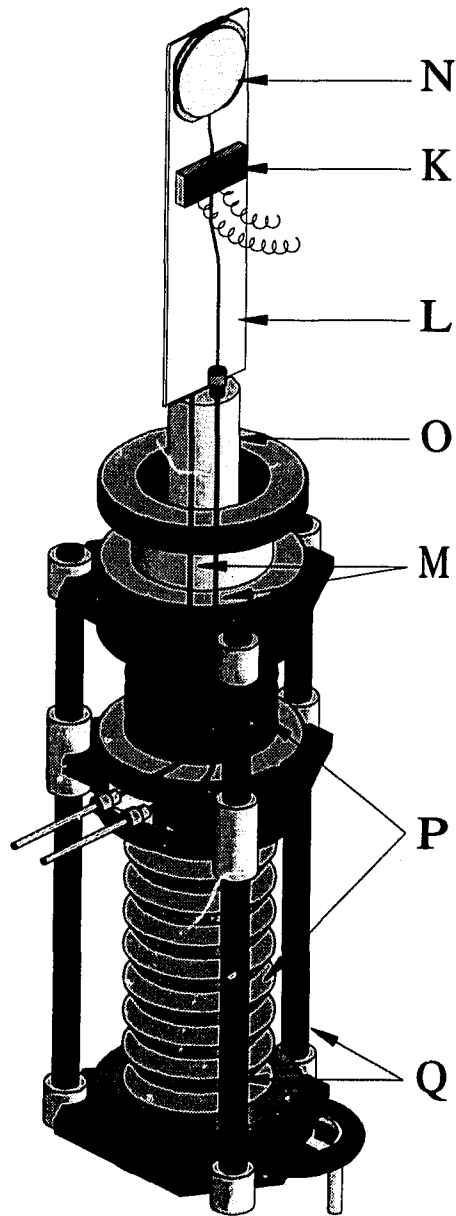


Figure 3.2.3: A view of the gas deposition diffuser showing the central diffuser support (L), braids to the heat shield (K), gas supply lines (M), diffuser chamber (N), mechanical support (O), bellows and vertical motion guide shafts (P,Q). The projection shows only one side of the full diffuser system; the second diffuser is obscured by the support (L).

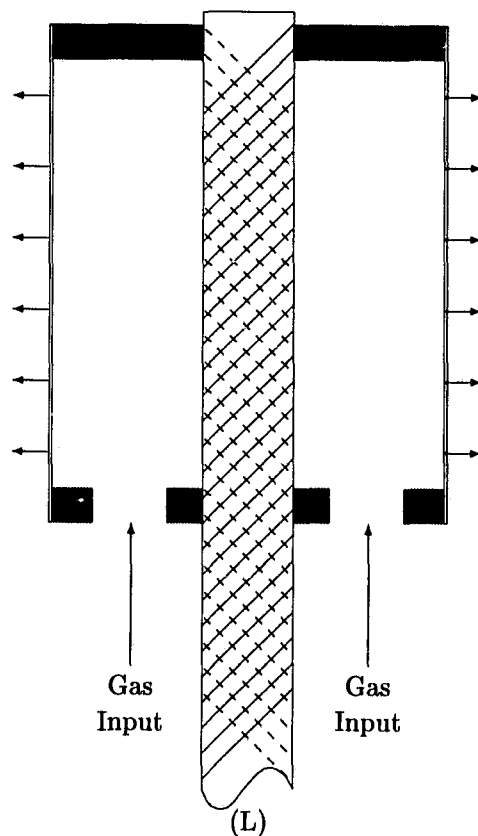


Figure 3.2.4: A vertical-section view of the gas diffusion assembly. The horizontal size is magnified by a factor of eight and the gas supply tubing has been removed for clarity. The top of the copper support, (L), is shown where the two diffusion chambers are mounted. The gas flow path into the chamber and out through the perforated metal is illustrated.

distortion precautions and maximum hydrogen target thickness were included.

Difficulties arose in controlling the deposition rate and total amount of gas released while using this system, so conductance measurements were made to optimize a new design [51]. The poor conductance of the long small-diameter supply lines resulted in a very long pump-down time to clean the lines, and allowed a pressure of several Torr at the gas inlet even when the target region was at a very high vacuum (10^{-7} Torr). To reduce the time required for target deposition and to gain more precise control of the amount of gas deposited, a new diffuser system was installed [52].

The copper sheet and diffusers were cooled to 100 K to suppress radiation loading of the target. Two flexible copper braids (detail K, Figs. 3.2.1 and 3.2.3) were connected to the copper sheet and the bottom of the radiation shield to provide a flexible thermal conduction path. The braids were long enough to allow the diffuser mount to move a total vertical distance of 160 mm.

The copper sheet was mounted on a tall thin-walled cylinder of stainless steel (detail O)

which served as a rigid mechanical, yet relatively poor thermal, contact to the movable flange. The movable flange was held between two bellows (detail P) to remove atmospheric pressure from the moving components, thus lowering the force required for motion and reducing the possibility of component failure. Two guide shafts and a lead screw (detail Q) provided well-controlled vertical motion. Guide rails on the inside of the radiation shield (detail J, Figs. 3.2.1 and 3.2.5) ensured that the copper sheet with its deposition units was accurately located between the target support frames.

3.2.4 The Target Vacuum System

The gas deposition system and the cryostat were both attached to a stainless-steel cube using knife-edge seals. The cryostat was introduced through the top port of the cube, which had been modified from a circular to a square aperture to accommodate the profile of the heat shield. The deposition and pumping systems were attached through the bottom port, leaving the four remaining sides of the cube for a muon entry port and windows through which detectors could view the target. Figure 3.2.5 shows a drawing of the cube. The target support foils (detail F) are seen through the radiation shield (detail I) which is drawn with one of its side plates removed for clarity. The partially inserted gas deposition system is shown entering through the bottom of the radiation shield (detail L).

Muons entered the system through a custom flange which had a thin ($25\ \mu\text{m}$) stainless-steel vacuum isolation window to protect the beam line vacuum from possible tritium contamination, and to protect the clean high-vacuum target from oil and other contaminants from the beam line vacuum system. Stainless-steel windows covered the remaining cube ports through which emitted radiations such as neutrons, gammas, and muon-decay electrons exit to the external detectors. The left and right side windows of the cube were used for neutron detectors, germanium x-ray and γ -ray counters, or wire chamber position tracking detectors, each of which was mounted externally to the vacuum system. The downstream position was useful only for the neutron detectors because of the beam transmission related backgrounds. The windows varied between $50\ \mu\text{m}$ thick for the window in front of the imaging system, to 3 mm thick in front of the downstream neutron detector. The internally located silicon detectors, designed to see the charged products of muon catalyzed fusion, were mounted on the thermal shield.

The entire vacuum system was constructed using all-metal, knife-edge fittings of a nominal 150 mm diameter, and all-metal valves⁶. For the experiments described herein, the pumping of the vacuum system was done with a cryo-sorption⁷ pump, a turbo-molecular pump, and an oil free roughing pump⁸.

When converted to tritium use, the vacuum system (without the cryostat installed)

⁶VAT, Haag, CH-9469, Switzerland, and MDC, Hayward CA, 94545

⁷CRYO-TORR High-Vacuum pump, CTI Cryogenics, Santa Clara, CA, 95051

⁸DVP-500 oil free mechanical pump, Varian Vacuum Products, Lexington, MA, 02173

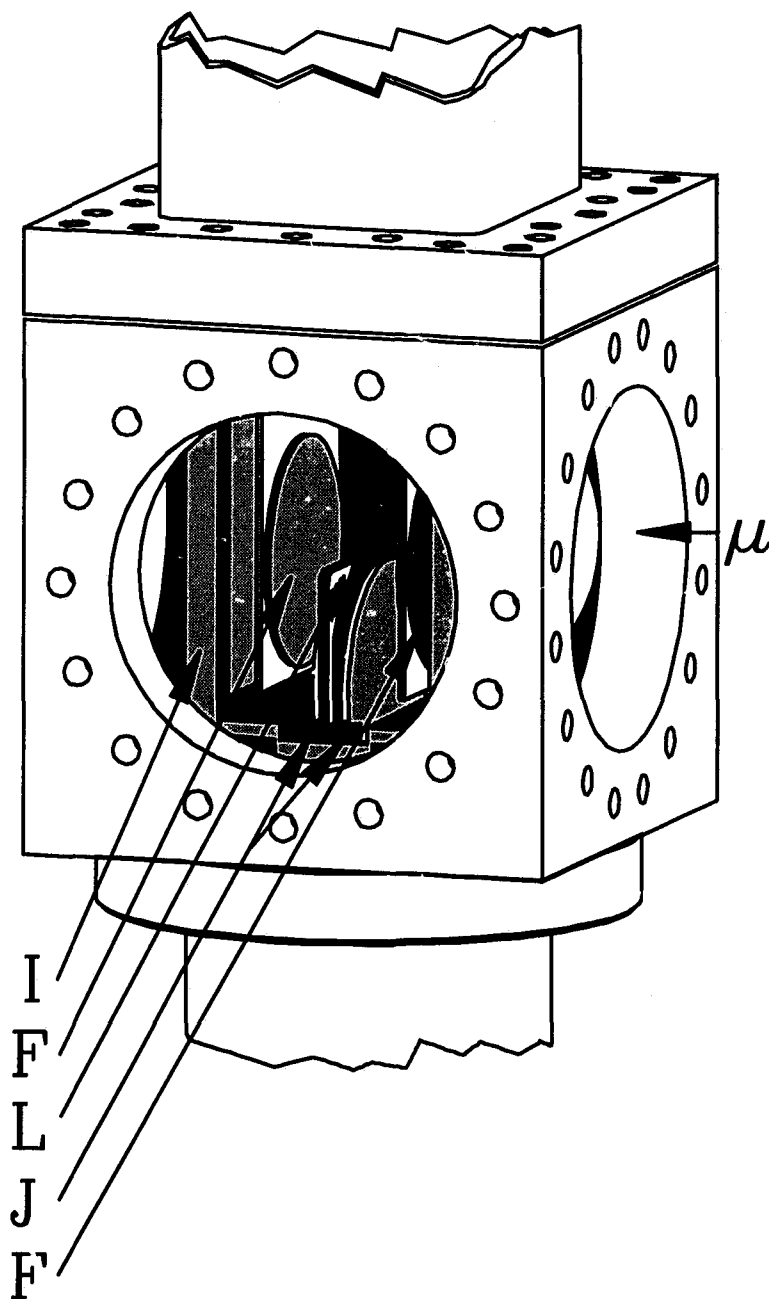


Figure 3.2.5: A perspective view of the assembled target system as viewed through an open side window of the stainless steel cube. The inner thermal shield side plate (which traditionally holds a silicon detector) has been removed. The orientation of the 3 K target foils (F), with respect to the heat shield (I) and the half-inserted diffuser (L) in its guide rails (J), is illustrated. The drawing also shows the position of the incident muon beam.

was cleaned by use of an oxygen plasma. A pressure of 300 mTorr of oxygen was required to start the cleaning. Once the plasma ignited, a pressure of 60 mTorr and a current of 1.3 A (which provided the brightest glow from the inside of the vacuum system) were maintained for 30 minutes. Pressures of $\sim 10^{-7}$ Torr were then routinely achieved after baking when pumped by a magnetic levitation turbo pump⁹, backed by an oil and elastomer free roughing pump system¹⁰. The exhaust of the pumps was directed to an evacuated 100 l volume to provide a closed-cycle pumping system for safe collection of residual tritium from the vacuum system.

3.2.5 The Gas Mixing System

Since the target system was designed to work with hydrogen isotope mixtures, a comprehensive system for purifying and mixing hydrogen was constructed. Experience from a previous hydrogen mixing system was incorporated in the design shown as a block-schematic layout in Fig. 3.2.5.

Isotopically pure protium was generated by electrolysis of deuterium-depleted water using a small commercial unit¹¹. Deuterium was obtained from bottled research-grade deuterium which was passed through a commercial palladium filter¹². Because small admixtures of protium in the deuterium did not disturb our measurements, ordinary research grade deuterium cleaned of nonhydrogens was sufficient. Other gases, such as He or Ne, were supplied as required through the gas inlet ports. The overall construction of the system relied on metal face-seal connections¹³ and bellows-sealed valves¹⁴.

The mixing system consisted of an accurately measured volume and one accurate capacitive manometer. By expansion of gases between volumes and the accurate measurement of the pressures, the volumes of all the mixing components were obtained. Gas mixtures were made by capturing the required amount of each gas in its own measured volume, and then opening the interconnections between the volumes.

The gas handling system pictured in Fig. 3.2.5 was the second iteration in a series of gas handling systems which has subsequently evolved into a tritium compatible system. As such the system corrected the shortcomings of the first design, but introduced new problems. The two main difficulties with the system occurred in the central mixing area delimited by the valve Va1, the volumes 1-3, the capacitive manometer, and the metering valve. Firstly, the multitude of connections to the relatively light tubing placed the manifold under stress which eventually lead to a small leak which introduced nitrogen into the hydrogen. The

⁹TurboVac 340M, Leybold Vacuum Products Inc., D5000 Cologne 51, Germany

¹⁰A combination of a Normetex D7 spiral pump, and a PV-12 bellows pump, Normetex Corporation, France

¹¹Elhygen Mark V, Milton Roy, Ireland

¹²Johnson-Mathey Inc., Wayne PA, 19087

¹³VCR Metal Gasket, Cajon, Macedonia, Oh 44056.

¹⁴SS-4BK-V51, NUPRO, Willoughby, Oh 44094.

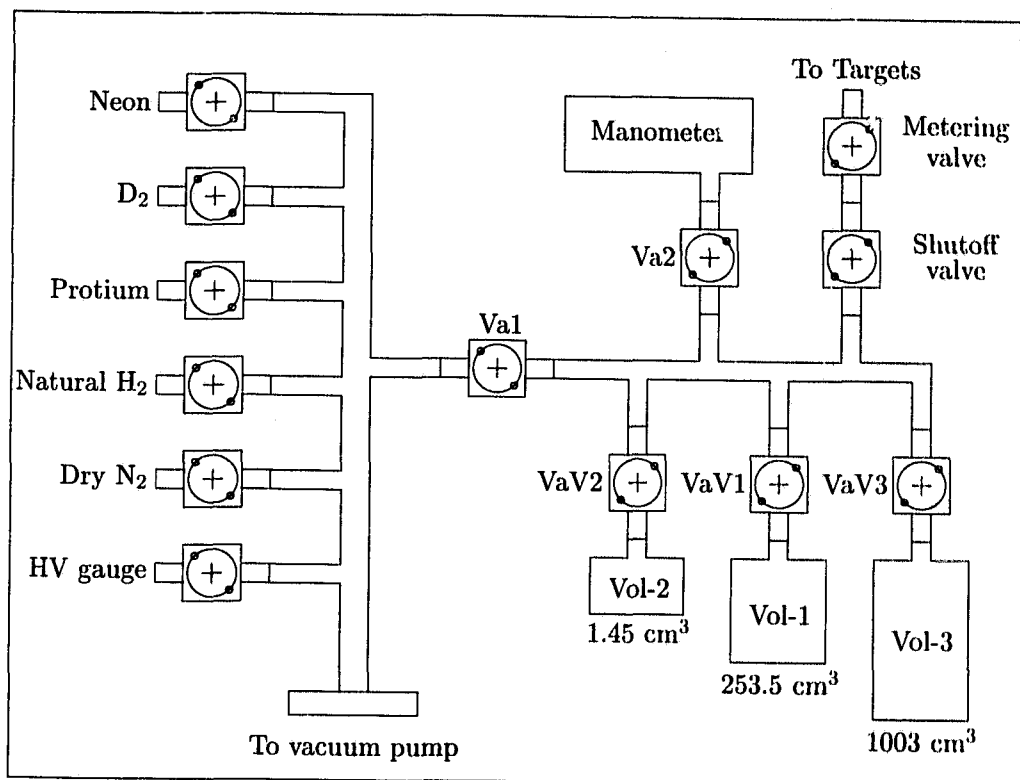


Figure 3.2.6: Layout of the gas mixing and deposition system in use during the operation of the target. The volume to the right of Va1 delimited by the VaV1-3 valves, the shutoff valve, and including the manometer was 35.5 cm³.

second problem involved the long lengths of relatively small diameter tubing which limited the conductance between volumes, and hence a long equilibration time was required to mix different hydrogen isotopes.

Once mixed, the gas was released at a slow rate by a metering valve into the vacuum system, through one of the two deposition lines (Detail M, Fig. 3.2.3, page 34), via the diffuser system which directed it to the target foil.

3.2.6 Operation

The continuous flow commercial cooling unit has provided good stability and reliability of operation. Cooling of the target system from room temperature can be accomplished in about four hours, with optimum running conditions achieved after twelve hours. When cold, the system consumes approximately 2.8 l of liquid helium per hour to maintain the 3 K target foil temperature. By use of a 500 l dewar of He, the target system was able to maintain a solid hydrogen layer for about a week, permitting studies at low event rates without alteration of the target conditions.

Of major concern in the design was the maximum achievable cooling power. High

cooling power was essential not only to maintain the 3 K temperature when a target had been deposited, but also to deposit a target of roughly one standard liter of hydrogen in a reasonable time. The measured cooling power of the cryostat is ~ 100 mW/K at the nominal 3 K operating temperature. This is sufficient to freeze one standard liter of hydrogen to a target foil in about 30 minutes.

A nominal pressure of 10^{-7} Torr was achieved at room temperature using the cryosorption pump, with water the dominant residual gas. When cold, the cryostat, because of the large surface area of the thermal shield, pumped more rapidly than the cryo-pump. Under these conditions, the vacuum system was isolated and the cryostat maintained the vacuum outside of the cold shield at 10^{-9} Torr.

The thickness and uniformity of the solid targets, studied by measuring the energy loss of alpha particles transmitted through the layer [53], is reproducible to 1% and uniform to $\sim 7\%$ over the FWHM beam distribution of 30 mm. This reliability extends to targets which are deposited in several different steps of different isotope concentrations even when many hours have passed between the application of each layer.

3.3 Electronics and Data Collection

Detector signals were sent to a counting room where they were processed and digitized by standard NIM and CAMAC electronics. The digitized signal data were read by a CAMAC STARBURST and then transferred to a VAX station for histogramming and storage on an 8 mm EXabyte tape. The data collection and taping was done by the VDACS VAX-based data acquisition system developed at TRIUMF. Online histograms were collected in the FLOWA format using the MOLLI analysis program and a custom analysis subroutine. Both FLOWA and MOLLI were developed at TRIUMF.

3.3.1 The Trigger

The trigger signal, which was composed from a pulse from the beam entrance scintillator in delayed logical coincidence with a gate enabled by any of the active detectors (cf. Fig. 3.4.1, page 44), was sent to the data acquisition system when a good event was detected. The electronics schematic, including module reference names (cf. Table XXIII, page 121), is given in Fig. 3.3.1; the timing of the elements in the schematic is given in Fig. 3.3.2.

When a muon passed through the entrance scintillator, T1, and deposited sufficient energy to pass an energy loss cut, the pile-up-gate (PUG) busy (B) output was set on for a $10 \mu\text{s}$ lock-out time. The barred output from the PUG (symbol \bar{B}), always set to the logical complement of the PUG output value, was used to indicate either that the system had accepted a muon (cf. Fig. 3.3.2), or was able to accept a muon. A general inhibit signal, \bar{I} , due either to an event trigger (HINH), the computer readout time (CINH and EI), or a failure in the high voltage supply of the wire chamber system (WCINH), was combined

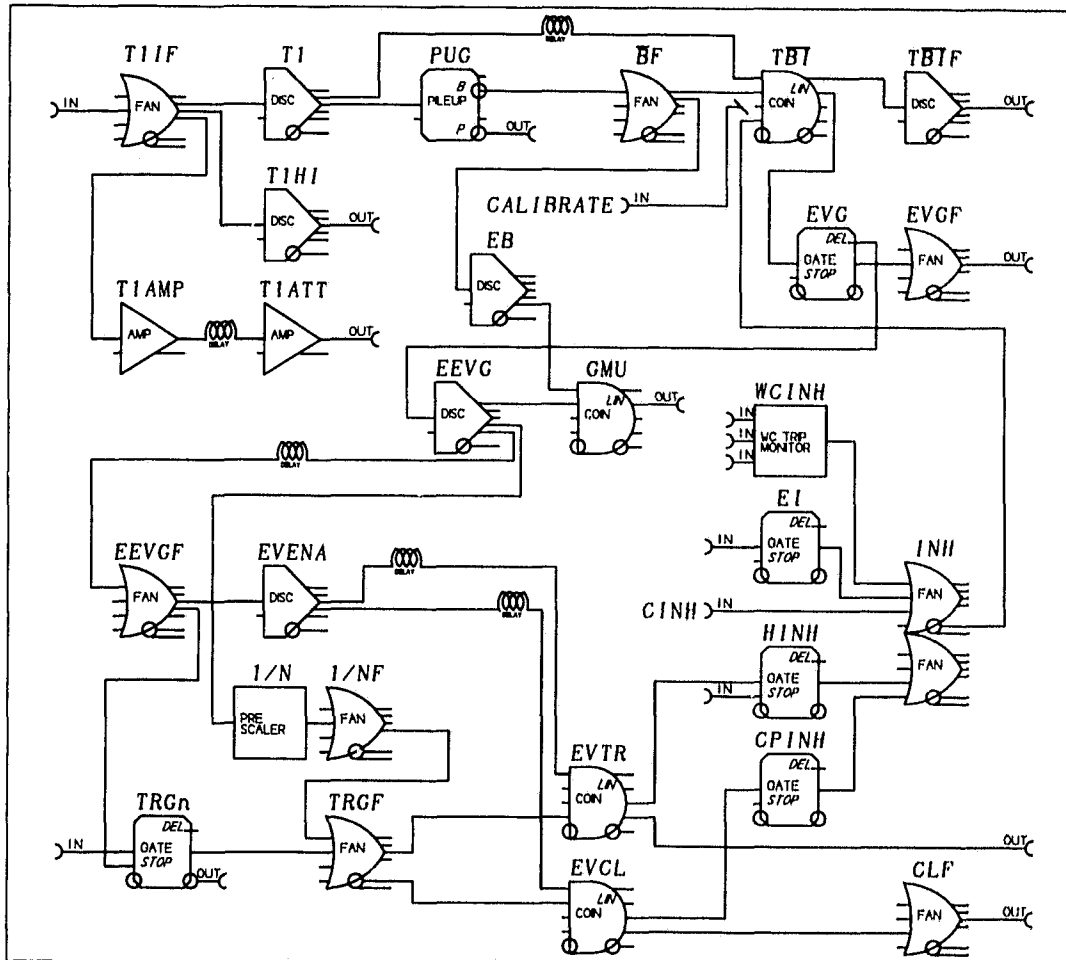


Figure 3.3.1: The electronics diagram for the trigger circuit. The input to T1IF came from the beam entrance scintillator T1 (cf. Fig.3.4.1, page 44; not to be confused with the T1 discriminator shown above) and the inputs to the (generic) TRGn were supplied by the individual detectors. The critical outputs of EVGF, EVTR, and EVCL were sent to the detector electronics, data acquisition computer, and CAMAC module clear inputs respectively.

with the T1 and \bar{B} signals to designate the condition when the event gate, EVG, could open and good events could be accepted. Thus an EVG would only open for a signal from T1, a nonbusy PUG, \bar{B} , and an attentive computer system, \bar{I} . The $\bar{B}\bar{I}$ signal was sent to the individual detector coincidences to permit acceptance of events, and to the CAMAC TDC units as a common start. Since the changes in the state of the trigger electronics were caused by the T1 signal alone, the timing of the $\bar{B}\bar{I}$ coincidence was critical. Disabling the \bar{B} signal [i.e., $\text{not}(\text{not}(\text{BUSY})) \equiv \text{BUSY}$] too quickly would not permit the $\bar{B}\bar{I}$ coincidence (cf. Fig. 3.3.2).

If a second muon activated the entrance scintillator T1 (dashed event in T1 time line, Fig. 3.3.2), the PUG began timing the lock-out again, extending it (dashed line extension

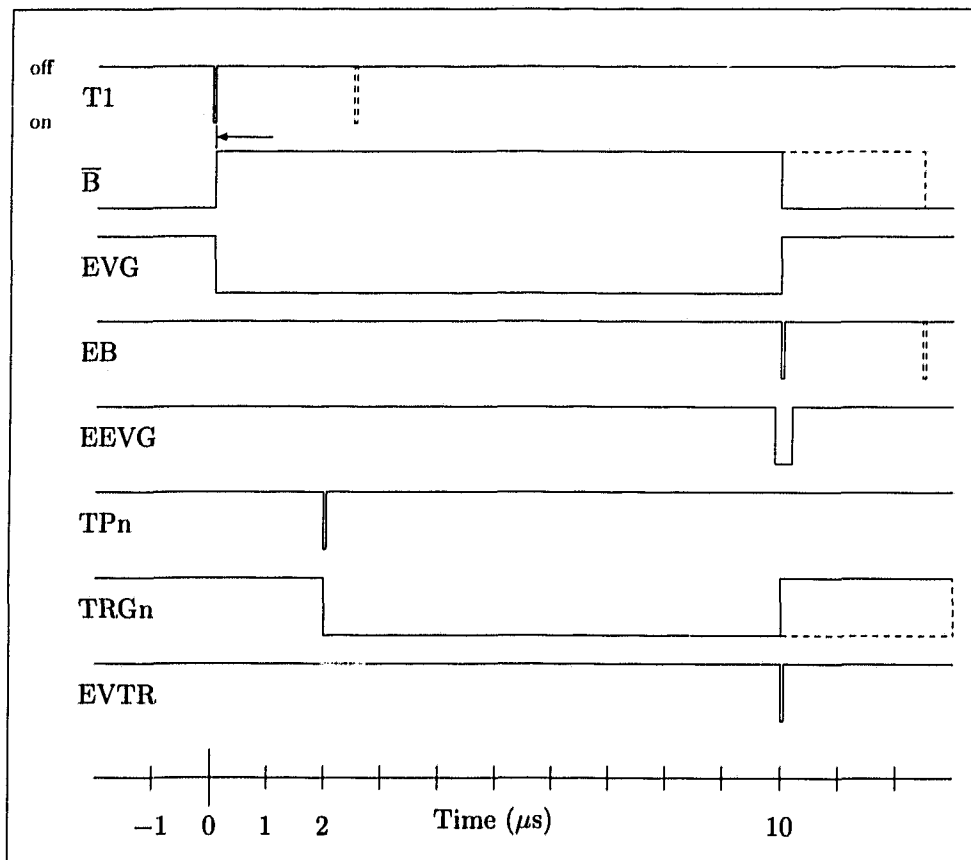


Figure 3.3.2: The timing setup for the electronics in Fig. 3.3.1. Time is indicated horizontally, and logic level, on/off, indicated by the lower/higher lines in keeping with the NIM logic level standard.

of \bar{B}). Although data collection was permitted to continue, a pattern bit was set in software to allow dismissal of the event. Removing the event using a hardware circuit was difficult due to problems in clearing the ADC's under these circumstances. This was due to the binary nature of the choice between EVTR and EVCL which did not allow a CLEAR signal to be issued when there was pile-up on an EVTR coincidence. Pile-up of events occurred for about 5% of the data so adding the hardware necessary to implement the pile-up CLEAR condition was more trouble than it was worth.

When any one of the n different detectors recorded an event at a time when the EVG gate was true, such as the pictured TPn in Fig. 3.3.2, a gate, TRGn, was opened. At the end of the event gate duration, the logical OR of all the possible TRGn gates was placed in coincidence with the end of the event gate EEVG to determine whether the event was read as an event trigger, EVTR (coincidence), or if it was cleared, EVCL (no coincidence). An event trigger would immediately initiate a hardware inhibit (HINH) to prevent loss of the data already measured by disabling the $T\bar{B}$ coincidence. A computer-driven signal

output system would maintain the inhibit while the data were read (CINH) and while the CAMAC modules were cleared (EI). An event clear would inhibit the trigger (CPINH) and then remove any values accidentally recorded by the CAMAC system.

Many scaler values (counts in a fixed time interval) were recorded to provide rapid diagnosis of the status of the detectors and electronics. Rate values for the T1, $\overline{\text{TBI}}$, EVG, EVTR, EVCL, and the TRGn signals were recorded and monitored since any change in these rates would be indicative of a problem somewhere in the data acquisition system. The average beam current and inhibit dead time were monitored by a special set of scalers, MON and $\overline{\text{MON}}$. One of the more important scalers was the GMU count, which was made by the coincidence of the end of busy, EB, and the end of event gate, EEVG, signals. These two signals in coincidence implied that there was no pileup and hence the muon was "good" in terms of the physics we wish to measure. Since no detector signal is required in this process, GMU is very close to the number of non-pile-up muons introduced into the target system and provides a rapid way to normalize data for comparison between runs.

As a consistency check on the status of the electronics, the GMU scaler can, in theory, be identically predicted from other scaler values via the relation:

$$\text{GMU} = \overline{\text{TBI}} \times \frac{\overline{\text{TBI}}}{\overline{\text{T1}}} \times \frac{\overline{\text{MON}}}{\overline{\text{MON}} \cdot \overline{\text{I}}}. \quad (3.1)$$

In practice, this value is slightly different than the GMU counter due to the finite widths and transition times of the logic signals. However, the two values generally agree to within 0.5%, hence the statement that GMU is "close to" the number of muons without pile up. Equation (3.1) was used to check each analyzed run, and runs where the scaler values did not agree within the 0.5% bound were discarded.

For further monitoring of the rather complex detector system, a special trigger, called 1/n, was implemented. This trigger was activated once for roughly every one thousand T1 triggers, independent of the dE/dx energy cut. The 1/n triggers permitted the monitoring of events which were unbiased in the sense that they did not require a detector trigger, for example, electrons which activated the T1 signal, but would not generate an event in the detectors.

3.4 Detectors

Several detection systems were used since each one reveals different information about the μCF processes. A general view of these systems and their positions is given in Fig. 3.4.1. When a valid trigger condition occurred, all of the detection systems were read not only to record the time and energy of the triggered detector, but of the other detectors as well. This ensured that the electronics were properly cleared.

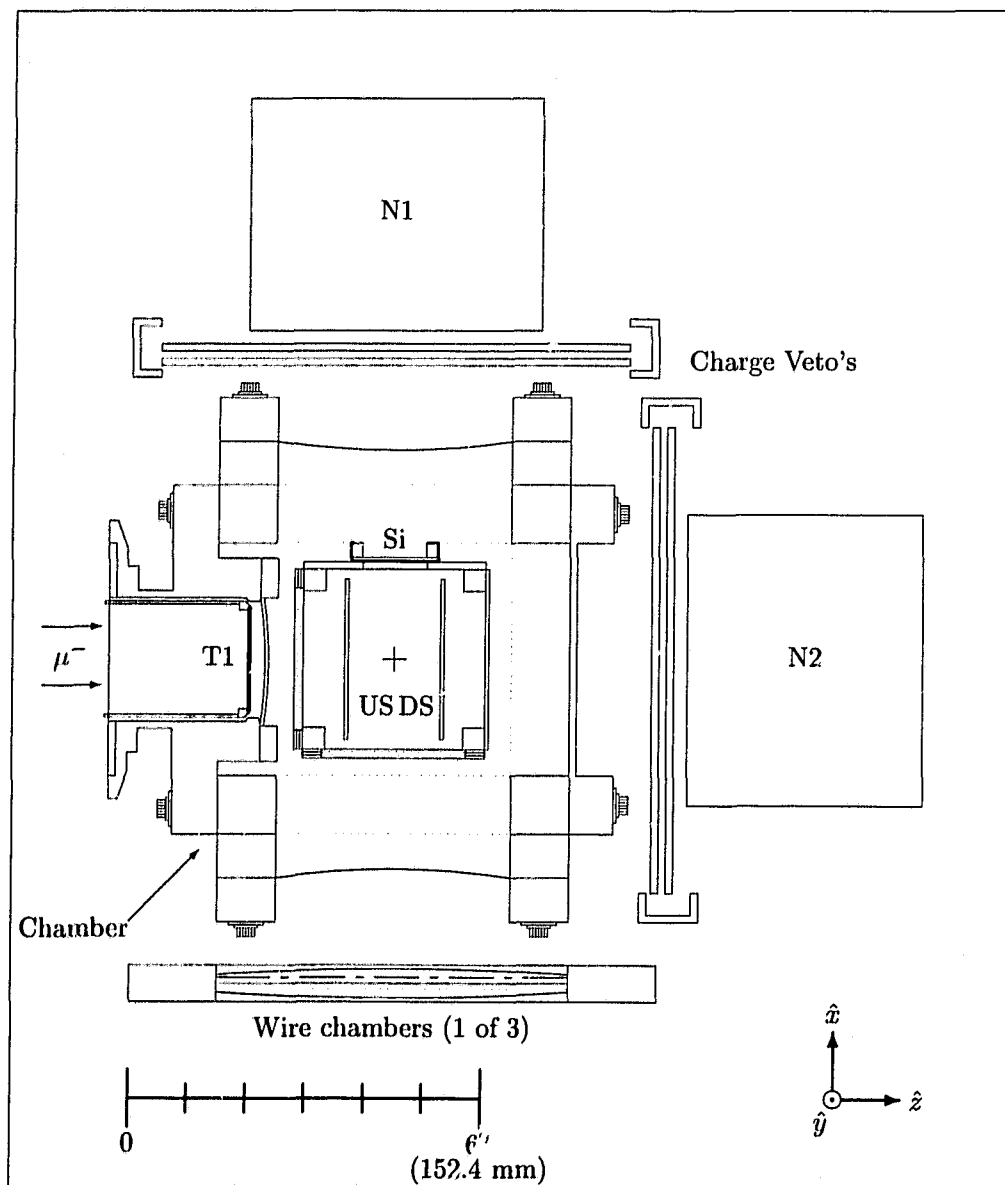


Figure 3.4.1: A top view of the detectors and their positions with respect to the target. The incoming muons are marked, thus clarifying the notation US, Upstream, and DS, Downstream, for the target foils. Not shown are the remaining two wire chambers, scintillators, and Sodium Iodide crystal which constituted the imaging system, nor the Germanium detector, which, when in use, replaced N1.

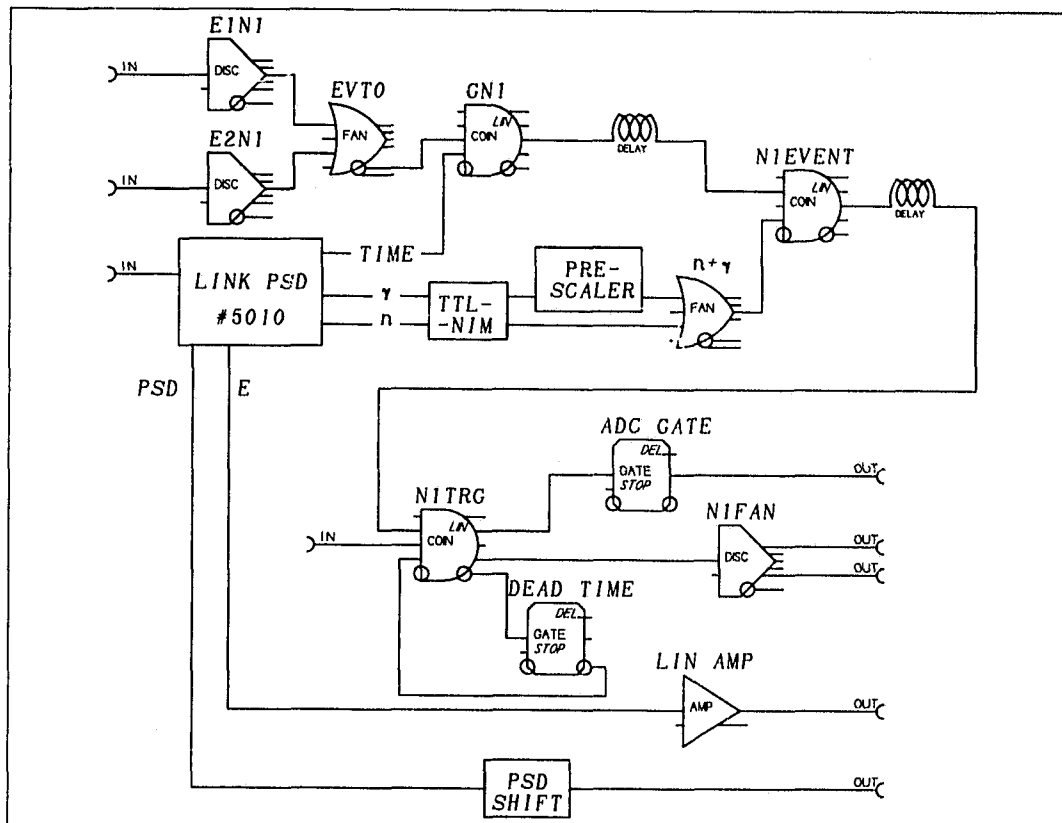


Figure 3.4.2: The electronics diagram for the neutron circuit. The inputs to the $EiN1$ discriminators came from the two veto scintillators, while the input to the PSD module came from the neutron detector itself. The NITRG accepted the EVGF signal, and based on the timing coincidences, sent a gate signal to the ADC which digitized the energy signal from the neutron detector (after amplification), and the PSD value (after a DC baseline shift).

3.4.1 Neutron Detection

Of the $d\mu d$ fusion products, only the neutrons exit the vacuum system. Two five inch diameter by four-inch deep enclosed cylinders of NE-213 liquid organic scintillator viewed by a photomultiplier were used as neutron detectors. NE-213 was chosen for its pulse shape discrimination properties.

Neither photons nor neutrons are charged, and thus neither will activate the thin scintillators used to reject charged particle events in the detectors. Some other method must be used to distinguish between these two types of events in the detector. The method is based on the interactions of the particles and the scintillation properties of the detector.

Photons will Compton scatter from the electrons in the scintillator resulting in an energetic electron which will cause scintillations and generate a signal. Neutrons only interact with nuclei. Organic scintillators generally have a high ratio of hydrogen to heavier

elements, so a neutron has a reasonable probability to scatter from a single proton, giving it energy, and thus creating an energetic proton which will cause scintillations and hence a signal in the detector. Pulse shape discrimination, or PSD, techniques for the detection of neutrons rely on the different light emission curves (pulse shapes) for electrons and protons losing energy in the scintillator. The light pulse has a different time structure depending on whether it was produced by a slowing electron or a slowing proton. By exploiting the difference in pulse shape, neutrons can be distinguished from photons.

The Link Systems PSD-5010, a hardware pulse shape discriminator, gave trigger level identification of neutron and photon events. The device distinguishes between the event types by integrating the signal pulse over two time ranges both of which start with the beginning of the pulse; a short interval of approximately 50 ns, and a long interval approximately 500 ns. The short interval was set so that it contained most of the signal produced by the slowing of electrons (which deposit energy quickly in the scintillator). The long interval was such that it covered all the signal that the short gate does, and much more of the signal produced by the slowing of the heavier proton. The weighted difference of the integrals, simply called the PSD value, gave a measure of the shape of the pulse and thus a method of distinguishing neutron events from photon events. For example, a photon event in the detector will generate roughly the same value in both integrals, and hence the difference is close to zero. A neutron event will make the integrals sufficiently different that the PSD value is nonzero. A selection based on the PSD value then identifies the neutron events.

The schematic for the neutron electronics can be seen in Fig. 3.4.2. Neutron event candidates were selected by requiring that the signal from the neutron detector be in anticoincidence with either member of a pair of charged-particle scintillators to ensure that the event was from an uncharged particle (E1N1 and E2N2 in the diagram). Meanwhile, the hardware PSD evaluated the shape of the energy signal to determine if the event was from a photon or a neutron, and then set an output level accordingly¹⁵. Since photon events were very common, prescaling was done to keep the photon triggers to an acceptable level. A good set of coincidences then activated the neutron trigger and sent the data to the computer. The prescaling was removed for the gamma calibration of the detectors.

An effective method for background suppression in μ CF processes was the requirement that the muon survived the event, a condition enforced by the detection of the muon decay electron. It was convenient to use all of the veto scintillators as decay electron counters. By requiring that the time of the detected muon decay electron was between 0.2 and 5.05 μ s after the time of a candidate fusion event, the signal-to-background ratio was strongly enhanced (see section 5.1). Even more effective, but much less efficient due to smaller solid angle, was a restriction on the electron energy requiring it to be at the high end of the

¹⁵The Link PSD-5010 had TTL logic outputs and hence required a level adaptor; the newer Oxford Instruments PSD-5020 has internal selector switches allowing TTL or NIM output.

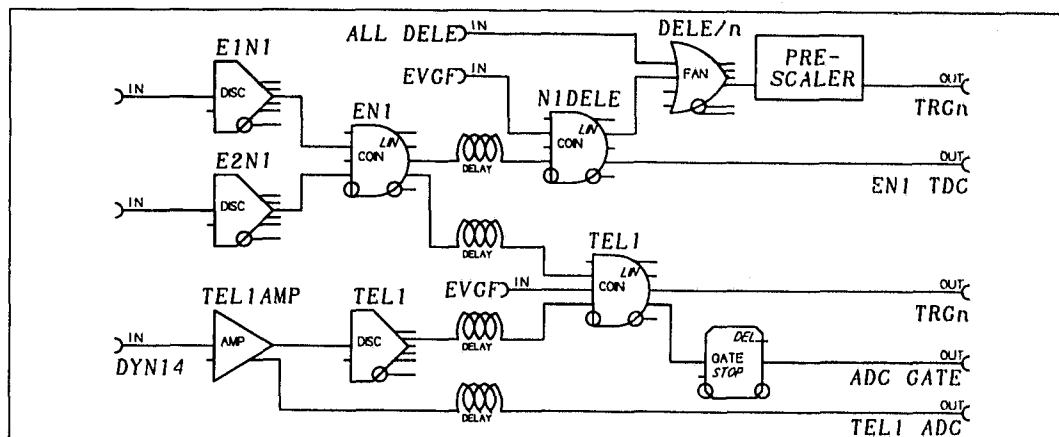


Figure 3.4.3: The electronics diagram for the delayed electron circuit. This is the schematic for the *del_e* and *del_tel* signals from N1 only. The *del_e* signal was made by a coincidence between the two veto scintillators E1N1 and E2N1 the time of which was sent to a TDC provided there was an EVGF signal. The sum of all *del_e* signals from all of the detectors was passed to a prescaler, which then provided a *del_e* trigger signal for every k events ($k = 16$ normally). The *del_tel* circuit accepted a fast dynode signal from the neutron detector and used it to provide a *del_tel* trigger, and an ADC gate and signal.

Michel spectrum.

A separate circuit (Fig. 3.4.3) recorded the time and energy when an electron from muon decay was detected either by the pair of scintillators (*del_e*), or by the scintillators and the neutron detector (*del_tel*). A dynode signal from the neutron counter photomultiplier was used as a fast independent signal from the detector. The dynode signal was then placed in coincidence with the electron veto counters to determine a clear signal from a charged particle. The *del_tel* condition was designated as a separate trigger. The digitized amplitude of the dynode signal measured the energy deposited in the detector by the charged event. Selecting events with sufficient energy ensured a high probability that its origin was from a muon decay. The fusion signals passing the *del_tel* cut were free from most backgrounds, but the limited solid angle of the neutron detectors made the cut too severe on statistics.

The *del_e* condition consisted only of the coincidence between the pair of veto counters. All of the charge-veto pairs were combined into one prescaled trigger to allow monitoring of the signal.

3.4.2 Silicon Charged-Particle Detectors

Two types of detector were used: a commercial device from Canberra, and a custom device, referred to as Si_2 ¹⁶, originally designed to function at very low temperatures. The custom device was mounted on the top of the diffuser system directly facing the target to achieve

¹⁶Provided by Dr. C.J. Martoff of Temple University

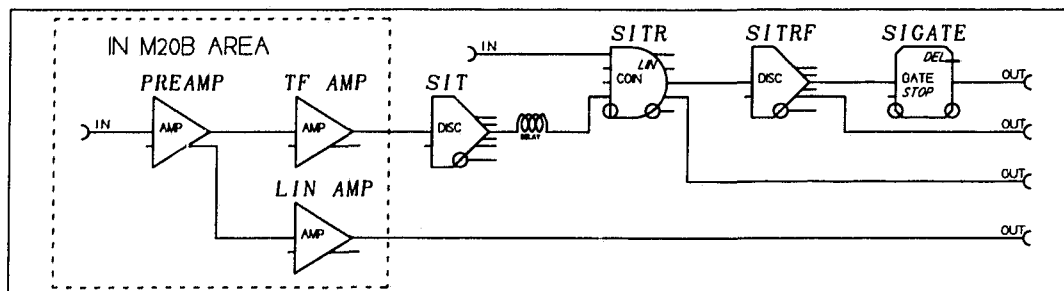


Figure 3.4.4: The electronics diagram for the silicon circuit. Because of the sensitive nature of the signals, the preamplifier, timing filter amplifier, and linear shaping amplifier were located in the experimental area, close to the detector. The energy and time signals were then sent to the counting room where coincidences with an EVGF signal were used stop the TDC and open the gate on the ADC to record the data.

maximum solid angle but did not operate consistently due mainly to the long separation between the detector and its preamplifier and the poor quality of the connection.

The commercial device, provided by Canberra, was an ion implanted, 600 mm² active area by 150 μ m active thickness, fully depleted diode. At the nominal operating voltage of 30 V it had a quoted resolution of 29 keV FWHM for α -particles. Due to mounting constraints and the distance to the preamplifier, we were unable to achieve resolution of that quality (see Appendix D). The silicon detector was mounted on the side of the cold shield, in front of the neutron detector N1, to detect the charged fusion products (see Fig. 3.4.1). The 3 MeV protons produced by dd fusion were easily seen but the ³He and tritons were too low in energy and hence lost in background or stopped in the solid target before they could reach the detector. This detector alone provided the data used herein.

3.4.3 Germanium Counter

A germanium counter was installed to look for muon-related atomic cascade photons generated from transfer to high-Z nuclei, as well as the photons from nuclear capture. A Canberra model GR3019 (55 mm crystal size) was set up in anticoincidence with charge-veto scintillators. To reduce background, the detector was enclosed in a 1.5" wall thickness copper cylinder which, in turn, was enclosed in a 1.5" wall thickness tungsten cylinder. The electronics used to process the germanium signals are shown in Fig. 3.4.5. The N1 detector was removed and the germanium put in its place whenever x-ray measurements were to be made.

3.4.4 Multi-Wire Proportional Chambers and Imaging

The electron from muon decay was used to reconstruct the position at which the muon decayed. The imaging system consisted of three delay line multi-wire proportional chambers to provide y-z position information, plastic scintillators for timing, and a large sodium

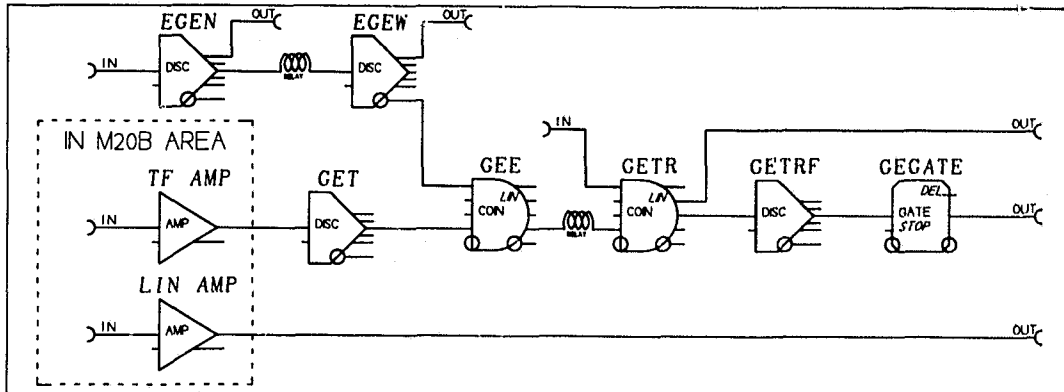


Figure 3.4.5: The electronics diagram for the germanium circuit. The electronics setup functioned in a similar manner as the silicon detector, with the added requirement of the anticoincidence with the charge particle scintillator. The GETR accepted the EVGF signal and used it to determine when the ADC gate and TDC stop were activated to record the event energy and time.

iodide crystal for accurate energy measurements on the detected electron. A straight line was fit to the positions given by the three wire chambers, and then selections were made on the quality of the fit. Quality cuts were also made on the energy deposited by the Michel electron, since the higher energy electrons were less susceptible to multiple scattering. Figure 3.4.6 shows the general form of the signal processing logic for the wire chambers.

The reconstruction of the muon decay electron path was extrapolated back to the central y - z plane of the target to give the position of the decay. The accuracy of the method depended on many factors but was generally good to about 3 mm FWHM resolution. The emission of muonic atoms from the hydrogen layers into the vacuum spaces was monitored by counting the number of decay events occurring in the clearly defined vacuum region.

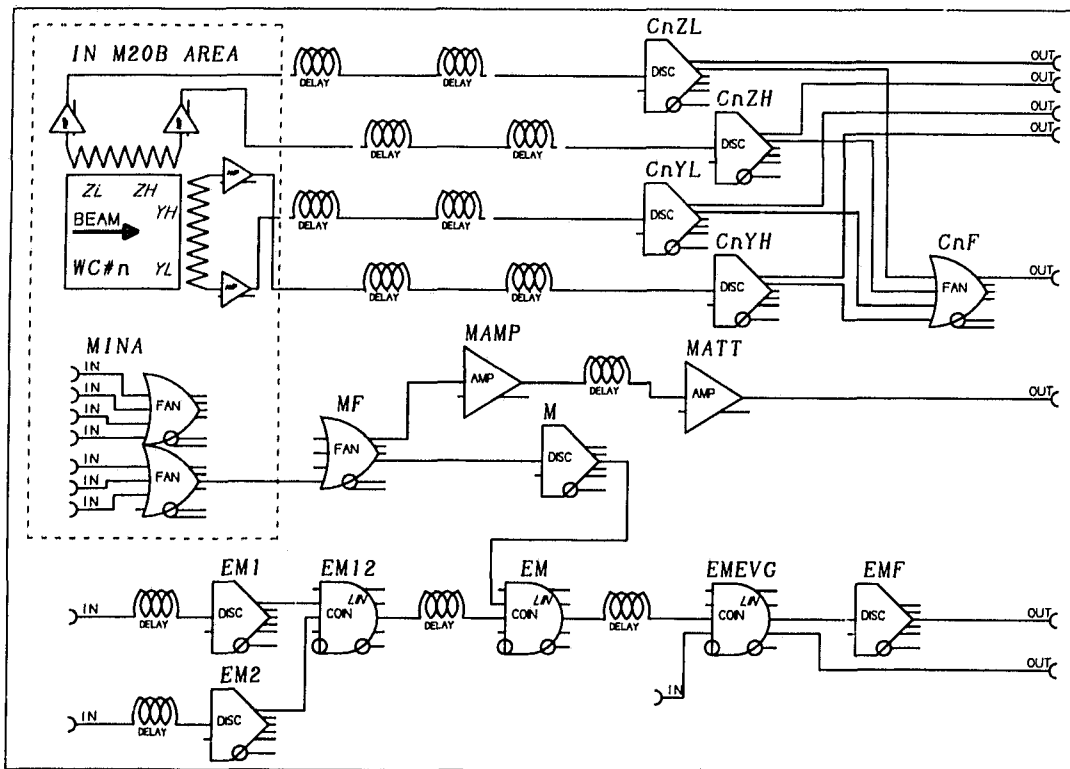


Figure 3.4.6: The electronics diagram for the wire-chamber circuit; only inputs from one chamber are shown: the two remaining chambers functioned in an identical fashion. The plastic scintillators EM1 and EM2 were used in coincidence with the EVGF signal to determine if a wire chamber event had occurred (EMEVG). When true, the electronics opened an ADC gate (not shown) which allowed the measurement of the MINA energy, and set the wire chamber trigger condition in the main trigger. The Cn(YZ)(LH) time signals were used to stop the individual TDC channels.

Chapter 4

Data

Data for the experiment were collected using two three-week runs within a period of one year. In the tables below, the solid targets are characterized by the position, either upstream, (US), or downstream, (DS), with respect to the geometrical center of the target, and by thickness, measured in units of Tl, or Torr \times liter, the amount of gas in a one liter volume at one Torr and ambient temperature (20°C). The conversion value between Tl and thickness has been measured using the energy loss of alpha particles traversing the layer, and the mean value was 3.2 $\mu\text{g} \cdot \text{cm}^{-2} \cdot (\text{Tl})^{-1}$ for $^1\text{H}_2$ (6.4 $\mu\text{g} \cdot \text{cm}^{-2} \cdot (\text{Tl})^{-1}$ for D_2) [53].

4.1 Solid Deuterium Runs

Data for pure solid deuterium were collected in both the February 1992 (FEB92), and August 1992 (AUG92), run times. The February run was devoted mostly to the testing of the then-new cryostat system, silicon detectors, and the wire chamber system allowing collection of muonic deuterium emission data. Reliability problems with the PSD units

Run #	Target type	Comment	GMU
1291	Neutron Calibration	Zone Background	n/a
1291	Neutron Calibration	^{60}Co	n/a
1291	Neutron Calibration	^{137}Cs	n/a
1299	1560 Tl D_2 US and DS	0.3 hr	6.279 M
1300	1560 Tl D_2 US and DS 'Thick'	4.8 hr	71.148 M
1301	1560 Tl D_2 US and DS	9.5 hr	139.184 M
1316	312 Tl D_2 US and DS	3.0 hr	50.571 M
1317	312 Tl D_2 US and DS 'Thin'	5.3 hr	66.295 M
1318	312 Tl D_2 US and DS	3.5 hr	47.042 M
1319	US and DS bare	1.3 hr	18.504 M
1320	313 Tl $^1\text{H}_2$ US and DS 'Thin'	3.5 hr	48.974 M
1325	1560 Tl $^1\text{H}_2$ US and DS 'Thick'	5.5 hr	59.797 M

Table IV: Summary table for the solid deuterium data of August 1992.

during that time meant that good neutron data are unavailable. Silicon detector spectra of the proton signals were collected, but the poor timing resolution, lack of clear background characterization, and low statistics did not allow meaningful analysis when compared to the quality of the AUG92 data set.

The AUG92 run time devoted a week to tuning the detectors and collecting good statistics on the fusion reaction in solid deuterium. Background measurements were also made by using solid protium targets, which have the same stopping fraction for the muons but no fusion processes to produce neutrons. The systematic study of the background was of the utmost importance in the analysis of the proton data. The runs used in the analysis as well as the exact target specification and GMU values are given in Table IV.

Run #	Target type	Time	S_{i_2}	GMU $\times 10^6$
1122	SET \oplus (2 + 3 + 3 = 8) Tl	3.0 hr	out	34.906
1123	SET \oplus (2 + 3 + 3 = 8) Tl	0.5 hr	in	3.941
1124	SET \oplus (2 + 3 + 3 = 8) Tl	1.4 hr	in	9.776
1128	SET \oplus (2 + 3 + 3 + 8 = 16) Tl	1.3 hr	out	10.074
1129	SET \oplus (2 + 3 + 3 + 8 + 35 = 51) Tl	2.3 hr	out	22.436
1130	SET \oplus (2 + 3 + 3 + 8 + 35 = 51) Tl	2.0 hr	in	18.019
1131	SET \oplus (0) Tl	1.0 hr	out	11.250
1132	SET \oplus (8) Tl	2.0 hr	out	29.900
1133	SET \oplus (8) Tl	0.7 hr	out	10.199
1134	SET \oplus (8 + 8 = 16) Tl	2.0 hr	out	28.089
1143	SET \oplus (8 + 8 = 16) Tl	1.6 hr	in	17.063
1144	SET \oplus (8 + 8 = 16) Tl	1.0 hr	out	15.563
1145	SET \oplus (8 + 8 = 16) Tl	0.6 hr	out	5.889
1147	SET \oplus (8 + 8 = 16) Tl	1.5 hr	in	11.264
1148	SET \oplus (8 + 8 + 8 = 24) Tl	4.6 hr	cal	65.199
1149	SET \oplus (8 + 8 + 8 + 7 = 35) Tl	2.1 hr	cal	30.202
1150	SET \oplus (8 + 8 + 8 + 7 + 15 = 50) Tl	1.1 hr	cal+10	16.488
1153	SET \oplus (8 + 8 + 8 + 7 + 15 = 50) Tl	1.9 hr	cal+13	27.326
1160	1040 Tl $^1\text{H}_2$	3.1 hr	out	44.678
1169	1040 Tl $^1\text{H}_2$	1.0 hr	cal+10	9.651
1170	1040 Tl $^1\text{H}_2$	1.3 hr	cal+10	14.467
1172	1040 Tl $^1\text{H}_2$	1.3 hr	cal+10	16.194
1173	1040 Tl $^1\text{H}_2$	3.0 hr	in	32.567

Table V: Summary table of the emission data. SET stands for Standard Emission Target, which in this case was 1040 Tl of deuterium doped protium mixture with $c_d = 10^{-3}$. The SET was deposited on the upstream foil; the downstream was bare. The \oplus is used to indicate that the D_2 layer was frozen on the surface in the increments summed in parenthesis. The column labeled S_{i_2} refers to the position of the second silicon detector, and is important since the 'in' position interfered with the solid angle of the side-mounted detector.

4.2 Muonic Deuterium Emission Data

In both FEB92 and AUG92, emission measurements were made. In general, an emission layer of 1040 Tl protium with a small admixture of deuterium, normally $c_d = 10^{-3}$, was frozen to the upstream foil. Muons stopped in the layer would undergo the capture on protium then transfer to deuterium after which the μd would escape the layer due to the Ramsauer-Townsend effect. The emitted μd atoms were subsequently reacted with a thin pure deuterium layer frozen to the surface of the emission layer.

Although detector tests and development were being done, meaningful data were collected during the FEB92 running period. Much of the AUG92 emission data were used to make a measurement of λ_{pd} . This was done by observing the muonic x rays generated by the transfer of the muon from the emitted μd to neon, which had been frozen in a thin layer on the surface of the emission layer, and thus there was no silicon detector data collected. The AUG92 emission data were collected for very thin deuterium surface layers with the intent of measuring effects on the μd transmission. The yield was too low in the silicon detector to allow analysis.

Since the S_{i2} detector was mounted in the target system, and tests were made on its functionality, it was sometimes in a position where it affected the solid angle of the main silicon detector. Its position was recorded as "in" the beam, "out" of the target volume entirely, or by the number of millimeters away from its calibration position. The experimental runs listed in Table V where the S_{i2} detector was "in" were analyzed qualitatively, since the lack of a measure of the solid angle of the main silicon detector made comparisons impossible.

4.3 Histogram Collection

Data analysis for histogram creation was done using the MOLLI¹ analysis package developed at TRIUMF. MOLLI is an interface that reads data from tape and passes it to a user defined subroutine which then creates the required histograms. The histograms themselves were stored in the FLOWA format, a program also developed at TRIUMF.

To facilitate the analysis process, a second interface to the histogramming package was written which alleviated the need to recompile and link the FORTRAN analysis subroutine. A text file containing histogram definitions was read by the compiled code and interpreted to define the necessary histograms. Changing the definition of a histogram, for example, a cut on a specified parameter, was accomplished by rerunning the analysis with the new definition file. Histograms were then accessed either by the REPLAY viewing package or the PHYSICA analysis package, and parameters extracted from there.

¹Multi OffLine Interactive analysis

Chapter 5

Analysis

5.1 Detector Calibration and Efficiencies

The work presented herein relied on the neutron detectors and the silicon diode. The neutron detectors were not working correctly for the FEB92 data run so the neutron information is limited to that taken in the AUG92 period. The Canberra silicon detector was similar for both runs; differences will be noted.

5.1.1 Neutron Detector

The energy calibration of a neutron detector is not straightforward. Monoenergetic neutrons are available only at specialized facilities, and the direct exposure of the detector to a source of monoenergetic protons is not possible due to the relatively heavily walled vessel containing the scintillator. The occasional drift of the phototube gain can change the calibration so a simple method is needed to allow frequent checks.

The calibration of the neutron detector energy response is made using the Compton edges of different gamma sources. An equivalency curve relating the Compton edge to the energy response of the scintillator to protons is made once for a detector (or if not the specific detector at least for the scintillator material) by using a source of monoenergetic neutrons [54]. The Compton edges then serve as an index to the neutron energy distribution. Discussion of the calibration process has been relegated to Appendix D.1, page 117.

The energy calibration is important since monoenergetic neutrons do not leave peaks in the energy spectrum. The scattering cross section for neutrons on protons is dominated by s wave contributions so scattered neutrons leave an essentially uniform pulse height distribution between zero energy (forward scattered neutrons) and the end-point energy (back scattered neutrons). Cuts on the low energy end of the spectrum remove some of the real counts from the monoenergetic source and hence affect the efficiency.

The PSD value is a comparison of integrals of the energy pulse. Low energy events can easily be misidentified so a certain energy threshold is required before the PSD value

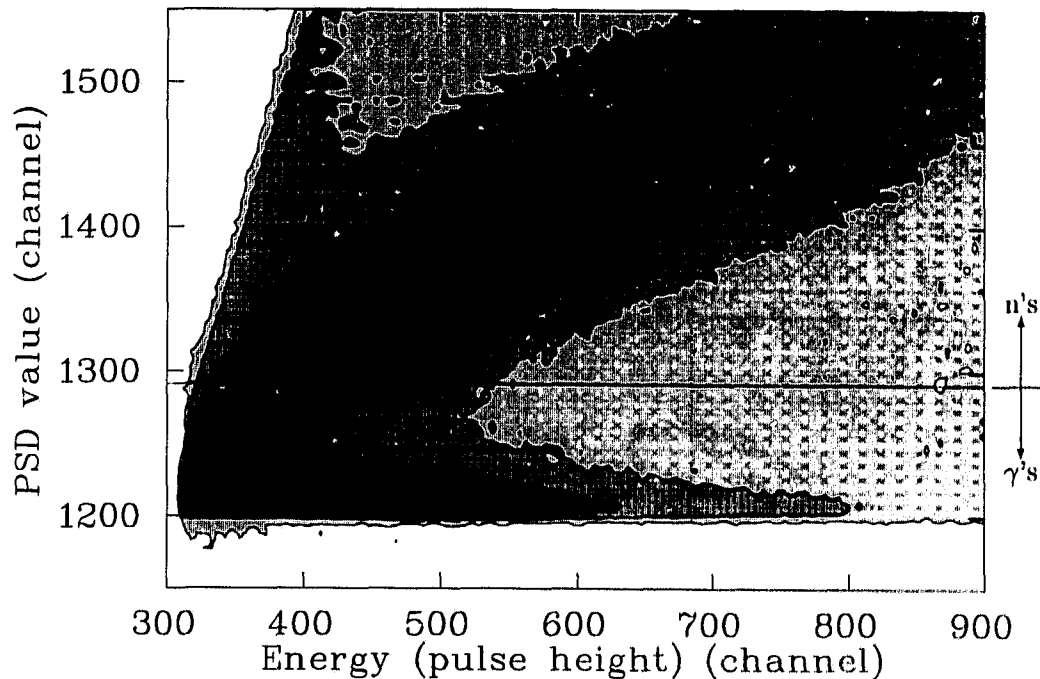


Figure 5.1.1: A PSD versus pulse height density plot for solid deuterium data. The two lobed structure is clearly visible: the relatively narrow horizontal band with PSD values near 1200 represent photon events. The broad band represent neutron events. The horizontal line at PSD=1291 shows the cut value, events above this line were considered to be neutrons in the analysis. Neutrons at 2.45 MeV give, at maximum, a pulse height of 900 channels (cf. Fig. 5.2.1, page 60). The fourth root of the number of counts determined the shading.

becomes reliable. Hence there is the trade-off between high statistics, realized by the full utilization of the pulse height spectrum, and the increase in background due to photons misidentified as neutrons by the PSD value.

Figure 5.1.1 shows a density plot of the pulse heights and PSD values of neutron detector signals. The fourth root of the number of counts was taken before plotting to allow regions other than the origin to be seen. For the analysis of neutron spectra in general, a cut on the PSD value was chosen to remove the photon events and studies were done to understand and remove background signals.

Although the energy and PSD cuts do a good job at identifying events from real neutrons, fusions were not the only source of neutrons. Capture reactions, for example muon nuclear capture on gold, will give neutron events correlated in time with the arrival of the muon. Since about half of the muons arriving in the target stop in gold, the intensity of the capture background is severe to the point where the fusion signal is lost in the background; even in the region of best signal-to-background ratio there were more than 10 background neutrons for each signal neutron.

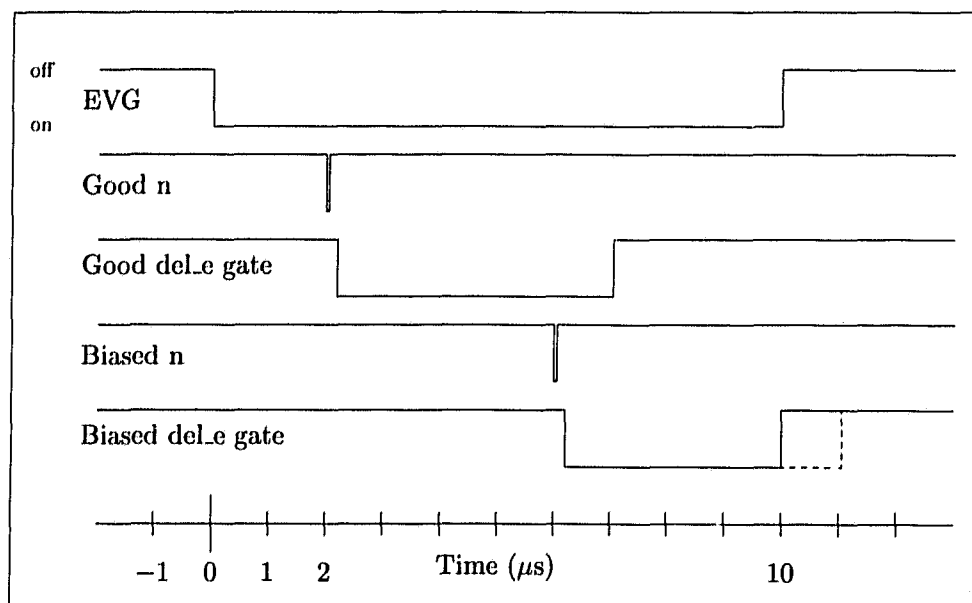


Figure 5.1.2: A pictorial representation of the biasing of the decay events caused by the closing of the global event gate EVG. For both the “good” trigger pulse, and the “biased” trigger pulse, the interval is shown over which decay electrons are accepted. For the “biased” event, the closing of EVG limits the time the detector has to register decay electrons, hence changing the efficiency. Time is indicated horizontally, and logic level, on/off, indicated by the lower/higher lines.

The capture background is strongly suppressed by demanding that the event which created the neutron does not consume the muon. This is done by observing the muon decay electron and requiring that the decay occurs after the neutron event. A cut is placed on the decay time requiring it to be at least 200 ns after the neutron event to help reject prompt accidental events in the delayed electron counters. A second cut requiring that the decay occurs within 5.05 μ s after the neutron event helps reject accidental coincidences. The time interval between the two cuts has an 81% probability of containing the muon decay.

For events occurring close to the end of the event gate, it is the end of the event gate and not the 5.05 μ s cut which will limit the efficiency of electron detection. Since the amount of time the counters are permitted to accept decays is reduced, the efficiency for the cut changes with time and suppresses counts at longer times. However, all neutron data with decay electron coincidence collected between the time of the muon arrival and 5.05 μ s before the end of the event gate is seen with the same efficiency. The 10 μ s event gate width means that the 4.95 μ s following the muon arrival contain events which are not biased by a 0.2-5.05 μ s decay time cut. Figure 5.1.2 illustrates the effect using a timeline.

The decay electron cut has a very strong effect on the background from nuclear

capture. Imposing the cut suppresses the data from fusion by the efficiency of the cut [12.15(30)%] but the background is removed so that it is less than 10% of the remaining spectrum, an increase in the signal-to-background ratio of about 100. The background that does survive the cut is predominantly neutrons from capture followed by an accidental event in the delayed electron coincidence.

The time resolution of a neutron detector at a given energy is determined mainly by the size of the detector. The interaction point of the neutron in the detector can be anywhere through the depth of the detector, so the time resolution is determined by the flight time of the neutron through the detector. Although the photomultiplier tube and electronics contribute to the time resolution, the contribution is small. For 2.45 MeV neutrons in a 10 cm detector the expected FWHM resolution is about 4 ns.

The solid angle of the detector was calculated by two methods. The first was a Monte Carlo method using the measured geometry of the target and detector. The second was taken from a comparison of the del_e and del_{tel} efficiencies. An event in the del_{tel} spectrum has already passed the del_e cut but has the added restriction both of the solid angle of the neutron detectors, and an energy cut on the dynode signal. The solid angle along with an estimate of the intrinsic efficiency of the detector, also found by Monte Carlo calculation, were used during the run to ensure that the detectors were operating correctly and detecting the correct number of events for a given muon flux.

5.1.2 Silicon Detector

The solid angle of the Canberra silicon detector was calculated by the Monte Carlo method and was the same both for the AUG92 and FEB92 measurements. The measured geometry of the target and detector placement were used, along with the best estimate of the beam stopping distribution, to calculate the effective solid angle of the detector with respect to the target. A value of 1.9(2)% of 4π was found. The uncertainty results mainly from the beam stopping distribution --- and hence the distribution of source events in the target and the uncertainty in the relative position of the detector with respect to the target.

The energy calibration of the detector was carried out by use of an alpha source taken from a common household smoke detector. These sources are small and easily mounted inside the confined geometry of the target system. During the AUG92 experiment the source was mounted on the diffuser to allow it to be withdrawn and not contaminate the silicon spectra when measurements were being made. During FEB92, when the two silicon detectors were in use, two smoke detector sources were installed in the vacuum system, one per detector. The position of the diffuser was used to determine which detector received signals from its calibration source. With the diffuser based silicon detector fully inserted, the side mounted Canberra detector received strong source signals. Actual calibration curves are shown in Appendix D.2.

An attempt was made to measure the efficiency of the detector at different energies by

the use of a precision pulse generator, whose output was sent into the detector preamplifier. By sending into the preamplifier a known number of counts at a well defined peak height for several known peak heights a measure of the linearity and efficiency of the detector can be found. The position of the peaks in the spectrum measures the linearity. The width of the peaks measures the effect of the electronics on the resolution. The intensity of the peak measures the efficiency.

Although this method gave a good measure of the linearity of the device, it did not give an accurate measure of the trigger efficiency as a function of energy. The pulse generator¹ had a limited bandwidth output, and could only simulate a 50 ns signal rise time, whereas the stopping of a charged particle in the detector generated a much sharper signal rise time. The amplitude of the preamplifier timing output was a function of the rise time, becoming larger as the rise time became sharper. Hence the timing pulse, and thus the triggering signal, from a charged particle was larger in comparison to the timing pulse resulting from the pulse generator for signals of equivalent energy amplitude. The difference was often a factor of two or more, and was found to depend strongly on the pulser settings, especially the use of attenuators. The measure of the efficiency as given by the pulser was an underestimate of the real efficiency of the detector. The pulser was effectively measuring the efficiency at an unknown lower energy. For events above 1 MeV, it is certain that the efficiency was 100%. Based on the measurements made at the time, there is evidence to indicate that the efficiency was still perfect even at a few hundred keV. We have not yet determined a simple method of finding the true efficiency; fortunately for the measurements reported here the absolute efficiency is not required.

Walk Correction

The silicon detector in the AUG92 run exhibited *time walk*, that is, a dependence of the time zero position on the energy measured. This distortion had a serious effect on the time spectra when large energy bins were used, since it mimics a very wide time resolution. Corrections were made based on the thick deuterium fusion spectra which exhibited a well defined time zero. The walk effect was measured, and then time spectra were corrected depending on the energy bin in which they fell.

Figure 5.1.3 shows a measure of the walk as extracted from the fusion signal in thick solid deuterium (1560Tl on each foil). Thick deuterium was chosen for the measurement since the energy loss of the protons as they left the thick layer provided a known shape of the time signal over an energy range of 3 MeV to 1 MeV. The difference in the flight time for a proton of 3 MeV compared to a proton at 1 MeV can account for no more than about 4 ns of difference between the high and low energy time zero positions.

The data in the figure were fit to an inverse energy dependence to give a formula by which to correct all of the time spectra used for fitting and parameter determination.

¹BNC model PB-4

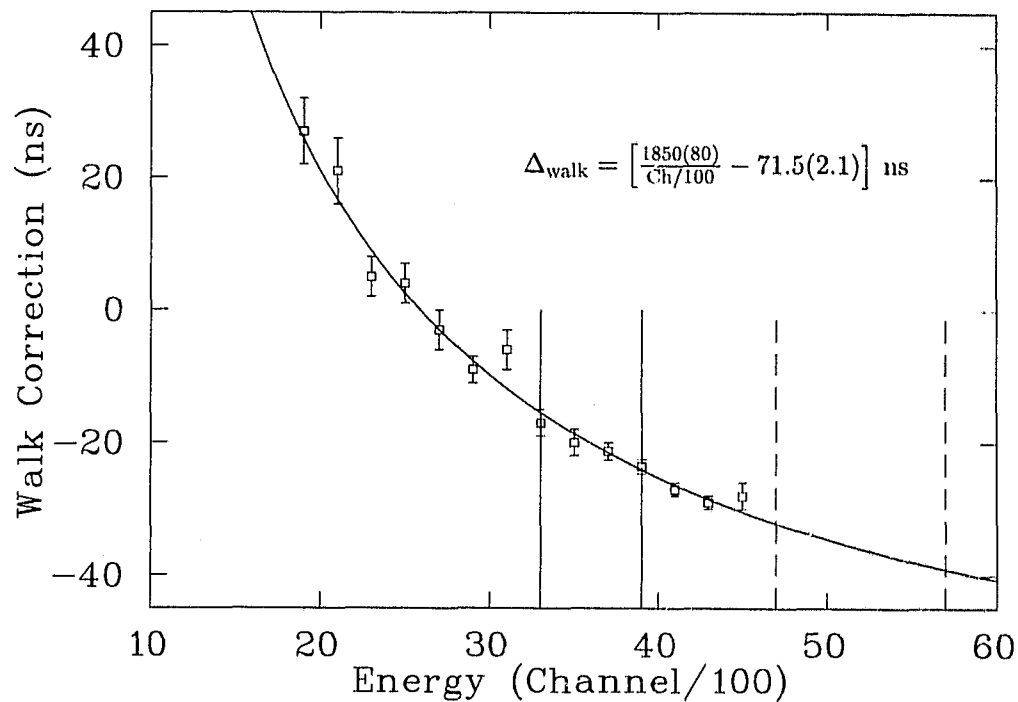


Figure 5.1.3: A plot of the measured time zero position versus energy channel extracted from the fusion time spectra in thick deuterium (1560 Tl). The walk correction curve is also plotted for the fit values shown. The solid bars show the energy interval where signal data for fits was taken. The dotted bars show the background region where the correction was taken from the extrapolation of the fit.

5.2 Solid Deuterium

The data for μCF in solid deuterium collected during the AUG92 measurements and summarized in Table IV, page 51, were analyzed to extract both neutron and proton time spectra. The time spectra were fit by the kinetics to extract the fusion cycle parameters.

5.2.1 Neutron Spectra

Sections 3.4.1 and 5.1.1 have outlined the nature of neutron detection and the types of signals that occur in the detector. Based on that, the backgrounds can be understood and accounted for in the fits to the fusion time spectra.

A plot of the energy spectrum for both single neutrons (referred to as "singles" and composed of the events passing the PSD cut only) and for del.e neutrons (events passing both the PSD cut and having an electron detected between $0.2 \mu\text{s}$ and $5.05 \mu\text{s}$ after the event) is shown in Fig. 5.2.1. The singles spectrum has the characteristic shape of capture neutrons, while the del.e spectrum clearly shows a spectrum resulting from monoenergetic neutrons on top of a much smaller background. The fusion signal is contained in the singles

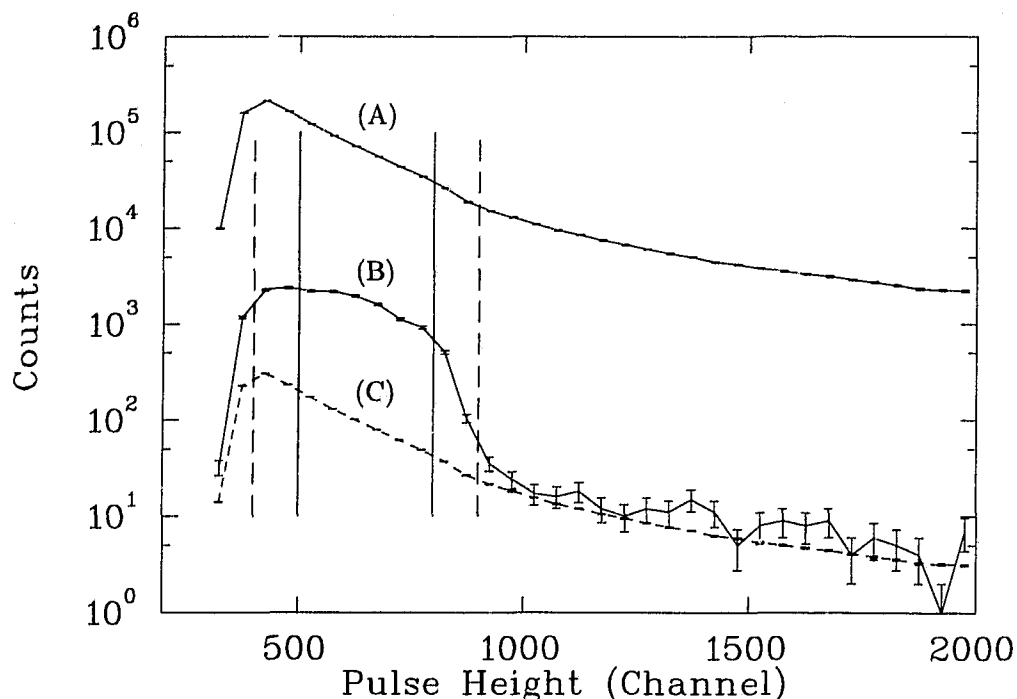


Figure 5.2.1: A plot of counts versus energy pulse height for singles and deuterium neutrons. The upper curve (A) is the spectrum of single neutrons. The middle curve (B) is of neutrons passing the deuterium condition and exhibits the characteristic profile of monoenergetic neutrons (where channel 900 represents the maximum pulse height generated by 2.45 MeV neutrons). The lower curve (C) is the scaled singles contribution to the deuterium spectrum [cf. Eq. (5.3), page 63].

spectrum, however the level of capture events far exceeds the number of fusion counts.

A pulse height cut was chosen selecting events between the solid vertical lines since it is in that region that the ratio of the deuterium signal to the singles (i.e., a type of “signal-to-background” ratio) was most favourable. A more relaxed version of the cut was also selected (dashed vertical lines). The spectra were made from the data that fell within the acceptable regions. It was from these time spectra that the kinetics parameters were extracted.

Figure 5.2.2 shows the time spectra of the singles and deuterium data for the pulse heights between the solid vertical bars in Fig. 5.2.1. Two lifetimes are visible in each of the curves (A) and (B) in Fig. 5.2.2, and while the long lifetime components are similar in the two spectra, the short lifetimes are radically different. In the singles spectrum, (A), the short lifetime is dominated by neutrons resulting from capture on gold and has the characteristic 80 ns lifetime. The deuterium short lifetime is dominated by the μCF kinetics and shows the lifetime of the $\mu d_{\frac{3}{2}}$ hyperfine state in deuterium. The long lifetimes are predominantly real

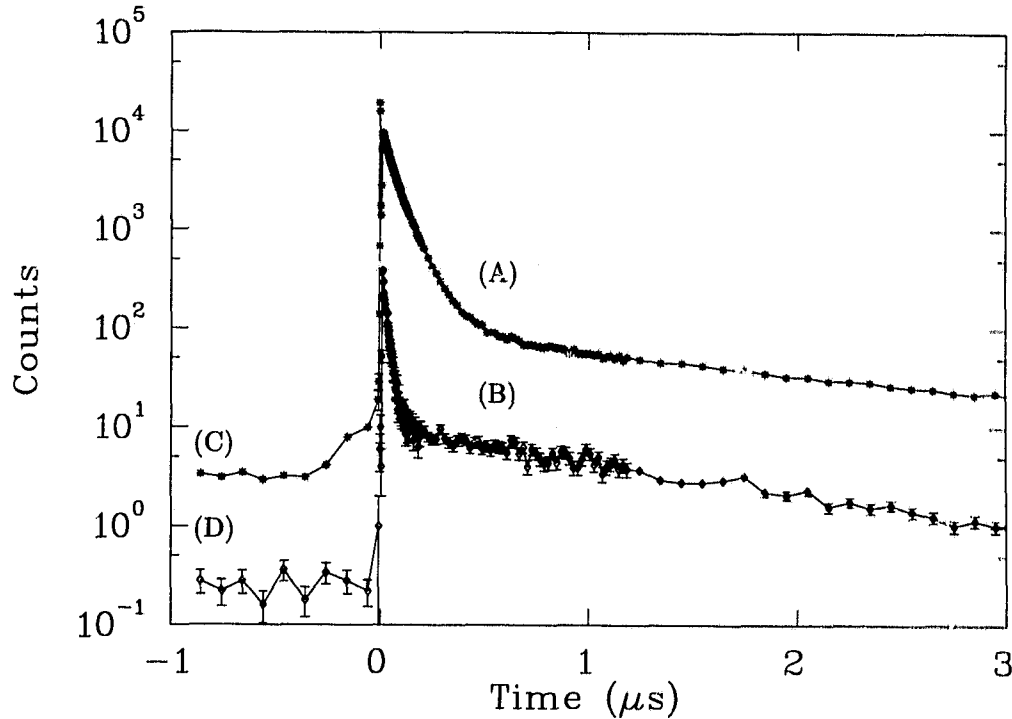


Figure 5.2.2: A plot of neutron time spectra for singles, (A), and del.e, (B), data. The flat background and electronics contribution to the singles spectrum can be seen at (C), while the del.e spectrum retains the flat background with proportionally less electronics contribution (D).

fusion events, although neutrons resulting from muon capture on nitrogen contamination will be present in the singles spectrum.

The energy plot of the del.e spectrum makes it clear that it still contains background and thus some method must be used to remove it during the fit. To do this it is necessary to study each of the neutron sources contributing to the singles spectrum and the manner by which they pass the del.e cut.

The signals in the neutron spectrum are of four basic types: fusion neutrons, capture neutrons, neutrons from the ambient background (zone neutrons), and electronic effects. Fusion neutrons, n_f , are generated according to the kinetics of the muon catalyzed fusion reactions in the target and are thus time correlated with the muon arrival and will pass the delayed electron cut with an efficiency ϵ_e , the efficiency with which the electron detectors measure that a muon has decayed in the specified time interval. This efficiency is comprised from a solid angle contribution and a time cut efficiency (λ the measured muon decay rate):

$$\epsilon_e = \Omega_e \lambda \int_{0.2 \mu\text{s}}^{5.05 \mu\text{s}} d\tau e^{-\lambda\tau}. \quad (5.1)$$

The capture neutrons, n_c , are also time correlated with the arrival of the muon, but

the consumption of the muon in the capture process means there is no muon decay to provide a signal in the electron detectors. Only those capture neutrons that are followed by some accidental event in the electron detectors will be admitted to the del_e spectrum. The efficiency for accidental events will be written as ϵ_a . The fusion neutrons, n_f , will also pass into the del_e spectrum with this accidental efficiency.

The two remaining components in the singles spectrum, the zone neutrons, n_{zone} , and electronics effects, $n_{\text{electronics}}$, require some attention for complete characterization. The area in which the experiment was conducted was in a constant neutron flux. Thus, independent of the arrival of a muon, there was a probability of a neutron event in the detector. In the singles time spectrum these events form a constant flat background.

The electronics effects are related to the integration gates that the PSD unit uses to discriminate between neutron-like and photon-like events. For example, consider the case where a photon triggers the PSD unit and the two integrators begin to measure the signal. The short integration gate has finished after about 50 ns but the long gate is still operating. If a second event occurs in the detector, the long integration gate will accept it and include it in the value of the long integral, hence biasing the event toward neutron PSD values. The probability of having a second event increases dramatically with the arrival of the muon (due to the flood of photons from atomic cascades). For an initial photon event that occurs close to the muon arrival time, the long gate is still open when the muon arrives, and with the muon generated radiation the ability to pass the PSD cut is enhanced. This effect is seen in the spectrum as the rise in the background starting at 500 ns before the muon arrival.

Since both of the above backgrounds are not caused directly by the muon itself, their ability to pass the del_e cut depends on the time of the signal with respect to the muon arrival. As a reminder, the del_e cut requires an event in the electron detectors in the interval of $0.2 \mu\text{s}$ to $5.05 \mu\text{s}$ after the signal. For a signal that occurs $5.05 \mu\text{s}$ before the muon arrival, only an accidental event (ϵ_a) can pass the signal into the del_e spectrum. As the time of the signal moves closer to the arrival of the muon, more and more of the cut interval overlaps with the time when a muon is known to be in the target and hence the efficiency for accepting the signal grows. For a signal occurring at $0.2 \mu\text{s}$ before the muon arrival, the cut interval overlaps exactly with the muon arrival and hence can detect the muon decay with an efficiency slightly larger than the decay electron efficiency ϵ_e due to the difference in time integrals. After the muon arrival, accidental events are accepted with the electron detection solid angle weighted by the probability that a muon had survived to the time of the signal. The flat background has thus been given a muon lifetime in the delayed spectrum. This relationship is represented by the integral in Eq. (5.3). Of course, accidental events permit signals into the del_e spectrum at all times.

A mathematical expression of the composition of the singles and del_e spectra can be

written as:

$$n_s = n_f + n_c + n_{zone} + n_{electronic} \quad (5.2)$$

and

$$n_{del_e} = (\epsilon_e + \epsilon_a) n_f + \epsilon_a n_c + \left(\epsilon_a + \Omega_e \lambda \int_{t+0.2 \mu s}^{t+5.05 \mu s} d\tau \Theta(\tau - t_0) e^{-\lambda(\tau - t_0)} \right) (n_{zone} + n_{electronic}). \quad (5.3)$$

Where $\Theta(\tau - t_0)$ is a step function which models the discrete arrival time of the muon.

It is instructive to examine $n_{del_e} - \epsilon_a n_s$ and transpose the singles spectrum to isolate the measured n_{del_e} spectrum.

$$n_{del_e} = \epsilon_e n_f + \epsilon_a n_s + \left(\Omega_e \lambda \int_{t+0.2 \mu s}^{t+5.05 \mu s} d\tau \Theta(\tau - t_0) e^{-\lambda(\tau - t_0)} \right) (n_{zone} + n_{electronic}). \quad (5.4)$$

The capture time spectrum, n_c , an unknown time-dependent quantity, has been removed entirely by the simple determination of ϵ_a , a constant. The singles spectrum is very well measured during the experiment and thus has small errors. The value of $(n_{zone} + n_{electronic})$ is very well modelled by a constant. The reason for treating the sum of the two terms as constant, when clearly only n_{zone} is constant in time, comes from their relative sizes when compared to the signal and the other background. The largest contribution to the background is from the accidental singles neutrons. The zone neutrons are an order of magnitude lower than that, and the electronic effects are less than a quarter of the zone neutrons. The events in the del_e spectrum occurring in the short time interval measured before the muon arrival are quite consistent with a constant. The above expression is of the form "data = fitting function" and it is the above that was used to extract the measured parameters.

A word is appropriate here on the use of weights in the fit. In a simple case where a model is fit to data, i.e., $d \pm \delta d = model$, the weight used for each point is simply $(\delta d)^{-2}$. In Eq. (5.4) above there are two input spectra, each with an uncertainty. Replacing the integral by the symbol $I(t)$, and dropping the ϵ_e (it will be absorbed by the normalization coefficient) we get

$$n_{del_e} \pm \delta n_{del_e} = n_f + \epsilon_a (n_s \pm \delta n_s) + I(t) (n_{zone} + n_{electronic}). \quad (5.5)$$

The value and normalization of the fusion contribution, n_f , after convolution with the detector resolution [cf. Eq. (5.10)] will be determined by the fit thus yielding the fusion parameters. $I(t)$ has a well determined functional form, and $(n_{zone} + n_{electronic})$ is treated as a constant (see above), the value of which is determined by the counts occurring before the muon arrival time. The determination of the weights for the χ^2 fit is then dependent only on the errors of the input spectra and will be:

$$weight = \left[(\delta n_{del_e})^2 + (\epsilon_a \delta n_s)^2 \right]^{-1}. \quad (5.6)$$

The weight contains the variable parameter ϵ_a , so the fitting routine will iterate on the fit, each time re-evaluating the weight, until a stable value for ϵ_a is found.

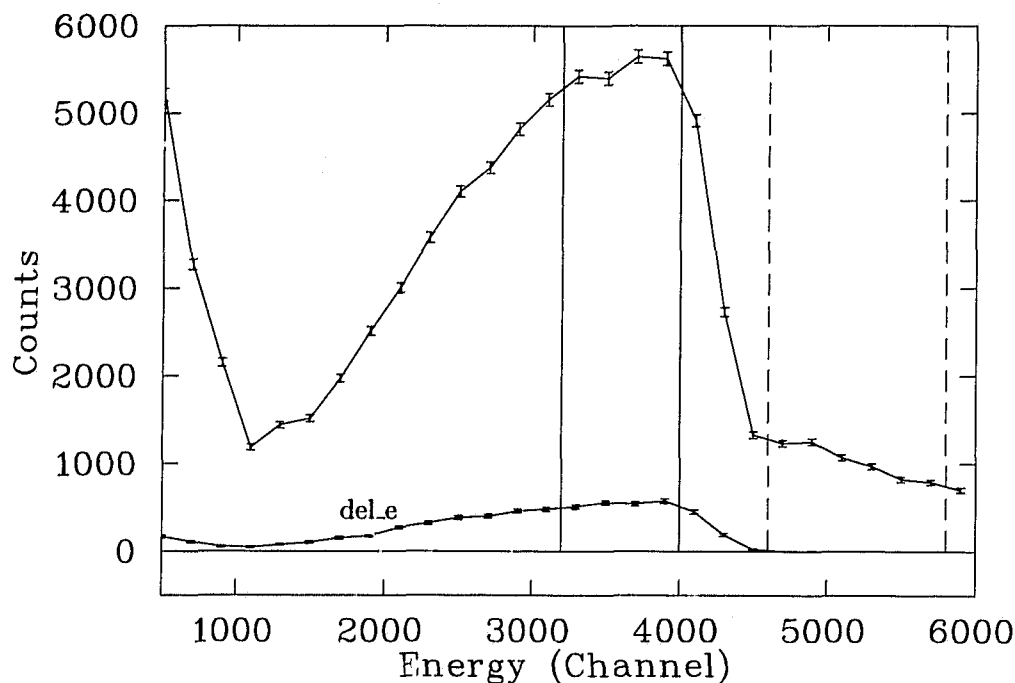


Figure 5.2.3: A plot of the silicon energy spectrum for solid deuterium. Note the spread of the 3 MeV proton peak due to energy loss in the thick target (1560 Tl on each foil) and the strong suppression of the background in the deLe spectrum. The boundaries of the "h" (dotted) and "l" (solid) energy cut regions are denoted.

5.2.2 Proton Spectra

The spectra of the silicon detector exhibit many different features, and careful study of different target types was required before a consistency of interpretation was achieved. Five different types of target were used to gain the quantitative understanding necessary to extract meaningful parameters.

Scatterplots of time versus energy for the five different types of target were collected. The different target conditions were: bare target, thick (1560 Tl) and thin (313 Tl) solid protium layers upstream and downstream, and thick (1560 Tl) and thin (312 Tl) solid deuterium layers upstream and downstream (cf. Table IV, page 51). Walk-corrected time spectra were collected (cf. §5.1.2, page 58) for 23 energy windows beginning at channel 1300 (0.9 MeV), each one 200 channels (142 keV) wide. Two standard energy regions were defined, based on the clarity of the fusion signal in the thick deuterium spectrum, and represent the signal region (channels 3300–3900, 2.3–2.7 MeV, called "l") and the background region (channels 4700–5700, 3.3–4.0 MeV, called "h"). Note that fusion protons are produced at 3.02 MeV. Comparisons and measurements of the time spectra in these regions for different targets were then made.

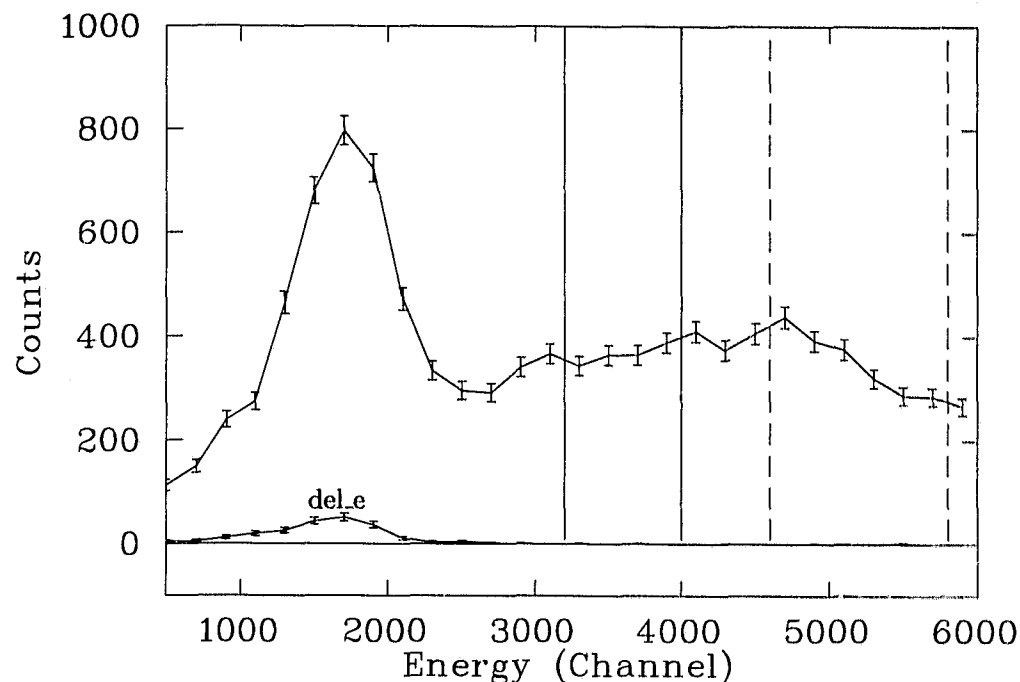


Figure 5.2.4: A plot of the silicon energy spectrum for the bare gold target. Here the shape of the background is visible, as are muons which scatter into the detector and stop. Note also the strong suppression of the background due to the del.e condition.

Energy Spectra Features

The background in the detector comes mainly from charged particle emission following nuclear muon capture. The intensity of this background with respect to the signal varied depending on the thickness of the hydrogen layers and the incident muon beam momentum. This effect can be understood in terms of the number of muons stopped in the gold of the target system and the silicon of the detector itself. As the beam momentum was optimized for stops in the hydrogen layer, the relative number of stops in elements giving rise to muon capture background varied.

Characteristic energy spectra are shown for the thick deuterium target, Fig. 5.2.3, and for the bare target, Fig. 5.2.4. The thick deuterium target exhibits a strong fusion signal which is spread out due to energy loss in the target layer. The fusion signal is on top of a background which comprises about 20% of the total counts. The bare target shows the background signal shape common to all of the spectra, as well as the lower energy peak resulting from muons which stop and capture in the silicon detector itself.

The background in the silicon detector was removed to the ϵ_a level by the del.e requirement, evidence that the background was due to a process which conserved the muon. The ϵ_a measured by the ratio of the number of counts in the h spectra (hence nonfusion re-

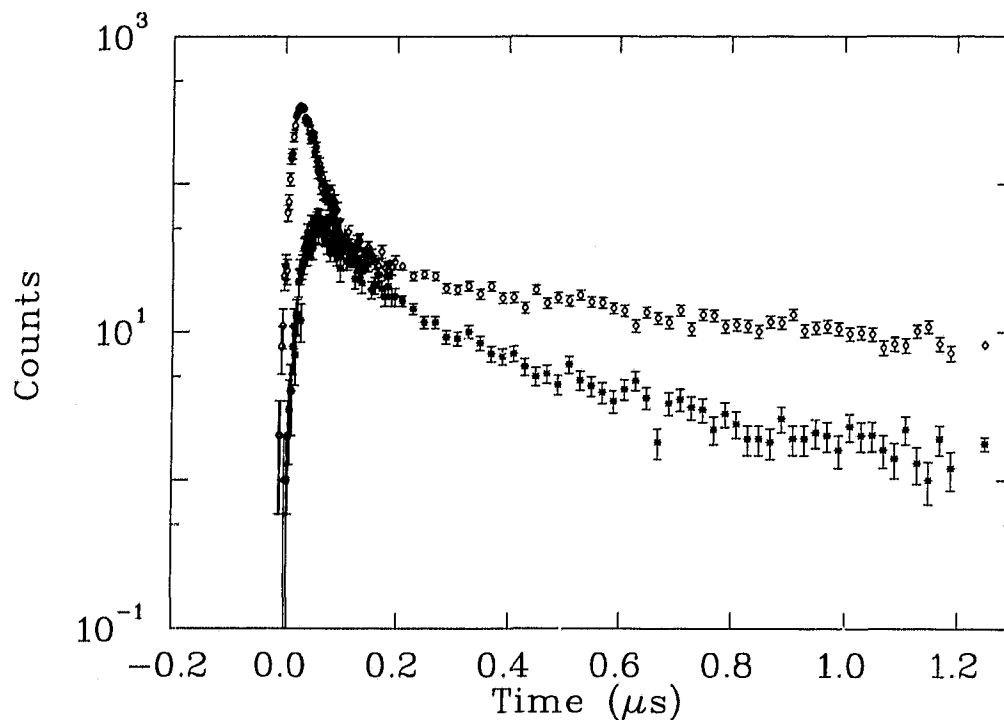


Figure 5.2.5: Plots of the silicon time spectrum from the *l* (diamonds) and *h* (stars) regions in thick solid deuterium (1560 Tl on each foil). Note the ~ 15 ns delay in the onset of counts in the *h* spectrum.

lated), to those from the same spectra which passed the delete cut gives a value of 0.11(4)%, which is in good agreement with the value found for ϵ_a from the neutron detector: 0.14(4)% (cf. Table VII, page 72).

Time Spectra Features

The time spectra of the 23 different energy regions for each of the five different target types were examined for intensity, number and value of visible lifetimes, and time-zero (onset) value. For data where fusion events contributed to the spectrum, the onset and rise time of the data were clearly visible (it is from here that the measures of the walk in the detector were taken, §5.1.2), as well as the characteristic two-lifetime structure of the kinetics in pure deuterium.

The walk correction was applied individually to each of the 23 spectra for the different target types, and the resulting corrected spectra for each target type were summed over the *l* and *h* energy windows to create high-statistics *l* and *h* time spectra for the different target conditions. The corrected and summed data were then rebinned with an adaptive step size which preserved the fine binning where sensitivity to fast rates was required, but

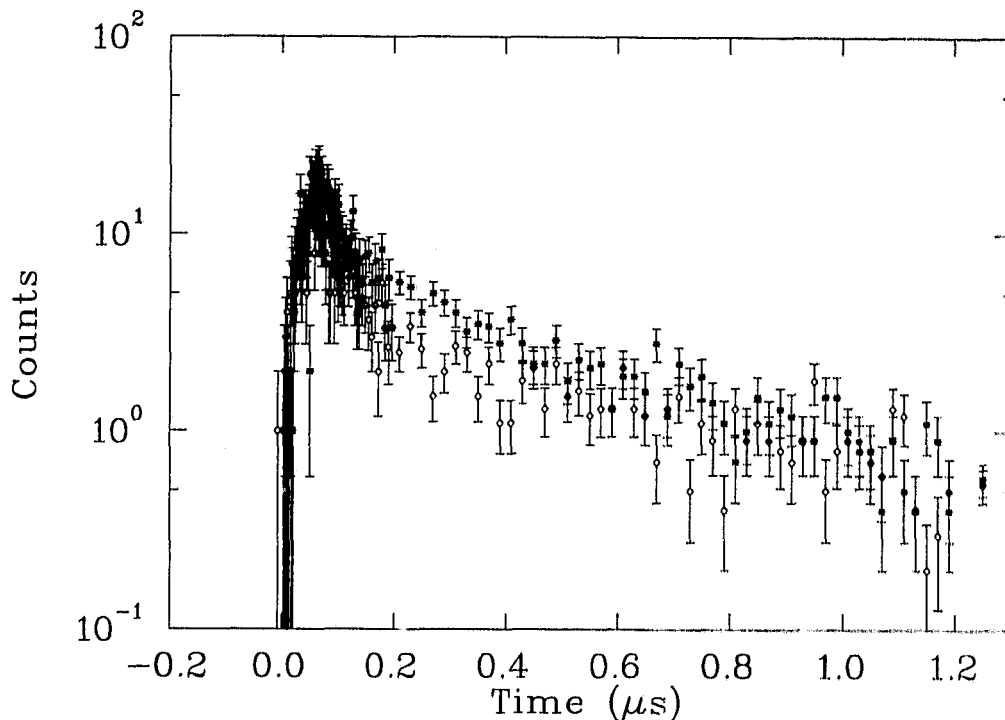


Figure 5.2.6: Plots of the time spectrum for the *l* (diamonds) and *h* (stars) regions from the bare target. The *l* spectrum is systematically lower than the *h* spectrum during early times.

used larger steps at long times where small scale sensitivity was not required². The larger bins at long times removed the problem of fitting data containing many zeros, and reduced the total number of points in the fit, which in turn significantly reduced the amount of computer time required per fit.

Figures 5.2.5, 5.2.6, and 5.2.7 show the time spectra for the *h* and *l* energy cut regions for the thick deuterium, bare target, and thick protium runs respectively.

The thick deuterium *l* region contains the strong fusion signal seen in the energy spectrum Fig. 5.2.3. The two lifetimes are the dominating feature in the data, which is to be expected based on the two-node approximation. The fusion spectrum has a rapid onset and rise of the leading edge, the shape given not by the physical processes of muon stopping, atomic capture and thermalization, but by the time resolution of the detector.

The background spectra in all three cases, the *h* and *l* regions for both gold and thick protium and the *h* region for thick deuterium, seem delayed with respect to the

²In the language of differential equations, the time spectra were stiff meaning that there are radically different decay constants in the solution of the problem. The granularity appropriate for one lifetime is either too large or too small for the other lifetime. Adaptively changing the step size depending on the time region of the solution being examined is the common approach to the problem.

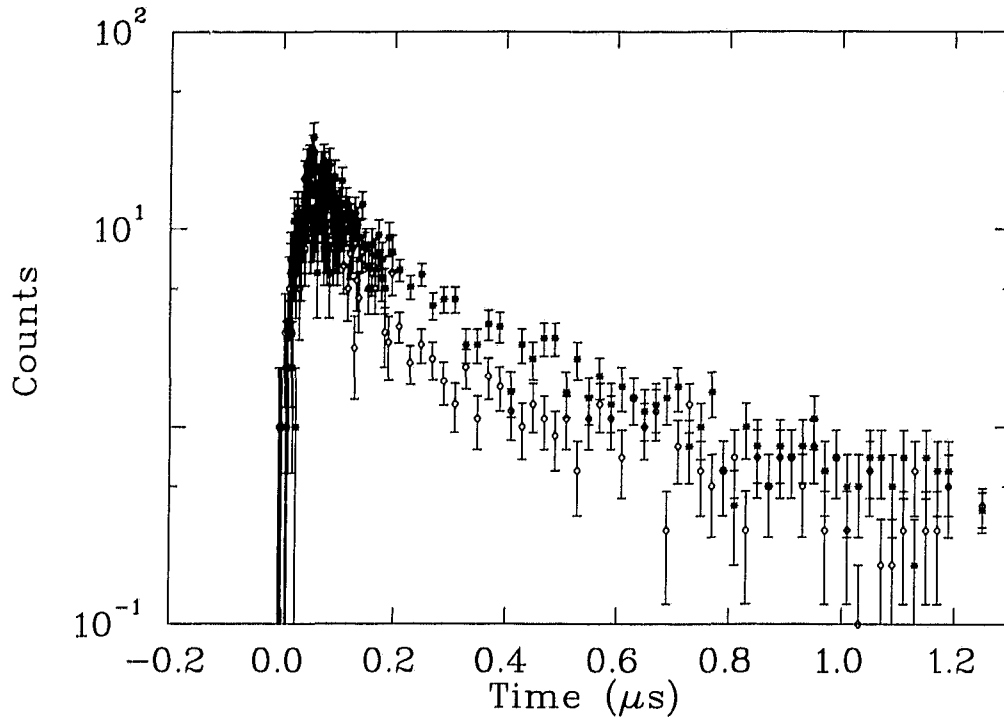


Figure 5.2.7: Plots of the silicon time spectrum for the *l* (diamonds) and *h* (stars) regions from the thick protium target (1560 Tl on each foil). Again the *l* spectrum is systematically lower than the *h* spectrum.

fusion signal. It is possible to extract two lifetimes from the background spectra as well, lifetimes consistent with a muon in gold (80 ns) and a muon in intermediate mass nuclei like silicon or aluminum (~ 700 ns). This background does not pass the ϵ_a cut except by ϵ_a coincidences (cf. Fig. 5.2.4). Unfortunately the statistics in the ϵ_a spectrum are poor to the point where the data is severely limited. The regular spectrum must be used and the background has to be characterized and removed explicitly.

Although the dominant process following nuclear muon capture is neutron emission, charged particles can also be emitted [55]. The emission of charged particle has to compete with other modes of nuclear deexcitation, such as multiple neutron emission or photon emission. For low energy emissions, the neutral particles do not have the nuclear Coulomb barrier to cross while the charged particles must tunnel through the barrier. Due to this effect, the charged particle spectrum is suppressed for energies below the nuclear Coulomb barrier for a given nuclei. Protons are the most commonly emitted particle, with an emission probability ranging from 15% for muon capture on silicon, down to about 1% following muon capture on a heavy nucleus like gold. For gold and silicon the Coulomb barriers are at about 16 and 5 MeV respectively.

The thickness of the active volume of the detector, $150 \mu\text{m}$, was sufficient to stop

protons of energies less than 4.5 MeV. Protons with more than that energy could pass through the active layer. The ionization deposited in the detector, and hence the induced current to the preamplifier, depended on the energy loss of the particle in the active layer. For example, if the proton were to pass through the detector, there would be no Bragg ionization peak from the end of the particle track. The difference in induced current would give a difference in rise time in the timing signal from the preamplifier and hence affect the relative timing of the event in the spectrum.

The explanation of the delay in the onset of nonfusion signals can be explained in this manner, with one small exception. If the background was due to the emission of protons following muon capture on materials in the target, why were there no low energy events which would have stopped fully in the detector and given sharp onset times? Since there were two thicknesses of hydrogen, ranging and energy loss of the protons produced by capture must have occurred but there was no evidence of nonfusion related, prompt onset low energy events.

Other sources of background were considered. The possibility of neutron reactions with the hydrogen target were excluded because the background was observed when there was no hydrogen in the target. Other neutron reactions were ruled out by time of flight considerations: it was extremely difficult to find a 15 ns delay by time of flight reactions for the target geometry and still have the measured energy. No satisfactory answer to this question has yet been found.

The background was parametrized and removed phenomenologically. The studies of the h and l time spectra for targets that did not produce fusion signals provided the method to predict the background in the l region given the spectrum in the h region. The curious discovery during the study was that the scaling from the h region to the l region was time dependent, i.e., $l(t) = f(t) \times h(t)$. This is consistent with the model of charged particles emitted after muon capture from different nuclei: the measured time structure of the emission spectrum, summed from components each having a different decay time constant and intensity, cannot be expected to be invariant under a translation in energy.

Four parameters were found to be sufficient to model the time dependence of the function transforming h spectra into the associated l spectra. The function used was:

$$f(t) = \left[A_1 + A_2 e^{-A_3(t-A_4)} \left(1 - e^{-A_3(t-A_4)} \right) \right]. \quad (5.7)$$

This function was chosen for its ability to allow good fits in the relation $l(t) = f(t) \times h(t)$. Once the parameters were determined, along with their correlations, the function f , and an uncertainty on the function δf were found³. Although the values of the parameters were strongly correlated, the value of $f \pm \delta f$ was well defined.

Since the delay condition was not imposed on the fit data, the l spectra containing fusion signals were simply composed of the fusion protons and the background. As ex-

³See, for example, Lyons, [56], §3.5, on the use of the error matrix.

plained above, the background in the l region can be found from the h region using the transformation function. The fit expression, with errors, is

$$p_l \pm \delta p_l = p_f + (f \pm \delta f) (p_h \pm \delta p_h) \quad (5.8)$$

where p_l is the measured time spectrum in the l energy window, p_h is the same for the h energy window, p_f is the kinetics function, after convolution, for protons production by μ CF [cf. Eq. (5.10)], and f is the transformation function.

With the quoted errors, the weight for the point is constructed in the same manner as in the neutron case, yielding:

$$\text{weight} = [(\delta p_l)^2 + (f \delta p_h)^2 + (p_h \delta f)^2]^{-1}. \quad (5.9)$$

The uncertainty in the background scaling function $f(t)$ enters into the calculation of the statistical uncertainty during the fit.

5.2.3 Fit Methods

In order to extract the rates for the muonic molecular processes in deuterium, the theoretically expected time distributions, Eq. (2.10), were convoluted with a detector resolution function and a step function modelling the muon arrival, see Appendix C, page 116, to give a function which more realistically represented the data. Explicitly, the function took the form:

$$\begin{aligned} k(t - t_0) = & \frac{N_0 \Psi_{\frac{3}{2}}}{2} \left\{ \mathcal{E} \mathcal{R} \mathcal{F} \mathcal{C} \left[-\frac{(t - t_0) + L_{\frac{3}{2}} \sigma^2}{\sqrt{2} \sigma^2} \right] \exp \left[L_{\frac{3}{2}} (t - t_0) + \frac{(L_{\frac{3}{2}} \sigma)^2}{2} \right] \right. \\ & \left. + \frac{\Psi_{\frac{1}{2}}}{\Psi_{\frac{3}{2}}} \mathcal{E} \mathcal{R} \mathcal{F} \mathcal{C} \left[-\frac{(t - t_0) + L_{\frac{1}{2}} \sigma^2}{\sqrt{2} \sigma^2} \right] \exp \left[L_{\frac{1}{2}} (t - t_0) + \frac{(L_{\frac{1}{2}} \sigma)^2}{2} \right] \right\} \quad (5.10) \end{aligned}$$

Excluding background parametrization, six independent parameters were required to completely determine the shape of a spectrum: two lifetimes, two amplitudes, the detector timing resolution, and the muon arrival time. There are ten parameters in the kinetics which determine the values of the two lifetimes and two amplitudes, and so it is impossible to measure more than four of them at any one time. Since an absolute measurement was not done, one of the parameters in the fit was used for normalization, so only three of the ten kinetics parameters could be extracted from a single time spectrum. By fitting the time spectra of both the neutron and proton data simultaneously, four kinetics parameters could be extracted (equivalent to doing an absolute measurement for a single fusion product spectrum). Unfortunately, it was necessary to use one parameter to fit the somewhat uninteresting nitrogen contamination of the target, hence the number of interesting physical parameters fitted was again reduced to three. The assumption of a background in the data introduced other parameters which were independent of the kinetics.

Parameter	Value	Source
λ_o	0.455160(8) μs^{-1}	Review of Particle Properties [57]
T	3.0(2) K	
ϵ	2-3% of 4π	See the text for discussion
ω_s	0.122(3)	Experiment: Balin <i>et al.</i> [31]
ϕ	1.4269(4)	Experiment: Petitjean <i>et al.</i> [58]
$\tilde{\lambda}_{\frac{1}{2}\frac{3}{2}}$	0 μs^{-1}	Detailed balance of $\tilde{\lambda}_{\frac{3}{2}\frac{1}{2}}$ at 3 K
$\lambda_{\frac{1}{2}}$	0.044(5) μs^{-1}	Experiment: Scrinzi <i>et al.</i> [23]
P_s	0.560	Theory: Fařfinan [26]
β_s	0.470	Theory: Hale [43]
β_p	0.580(5)	Experiment: Zmeskal <i>et al.</i> [24]

Table VI: Table of standard values passed to the fitting routine. The fits to the data required the first six values but were unable to return any measurements of those values. The last four values in the table were required in the kinetics, but were also measurable depending on the number of available free parameters.

A fit of the distribution in Eq. (5.10) to the data was made by chi squared minimization. A Fortran function representing the fitting function was loaded into the PHYSICA analysis program and used to extract the kinetics parameters.

The fits to the spectra are sensitive to the input values of $\tilde{\lambda}_{\frac{3}{2}\frac{1}{2}}$, $\tilde{\lambda}_{\frac{1}{2}}$, $\phi_z\lambda_z$ (the loss rate to nitrogen), $\tilde{\lambda}_{\frac{1}{2}}$, P_s , β_s , and β_p . The standard values of the parameters passed to the fitting routine are given in Table VI, along with the uncertainty on the value used when examining the systematic uncertainties.

5.2.4 Fit Results

For both the neutron and proton time spectra, fits were made to the individual spectra. For the neutron detector, the data were restricted to the thick deuterium targets only, since insufficient statistics existed for the thin deuterium layers. For the proton data, both thick and thin deuterium layers yielded spectra which could be fit.

In the fits to individual spectra, the two kinetics parameters $\tilde{\lambda}_{\frac{3}{2}\frac{1}{2}}$ and $\tilde{\lambda}_{\frac{1}{2}}$, as well as the loss rate to high Z components, $\phi_z\lambda_z$, were measured. When the fits to the combined spectra were done, the sensitivity to four parameters was used to measure $\tilde{\lambda}_{\frac{3}{2}\frac{1}{2}}$, $\tilde{\lambda}_{\frac{1}{2}}$, $\phi_z\lambda_z$, and values for $\tilde{\lambda}_{\frac{1}{2}}$, P_s , β_s , and β_p , each one of the latter four taken in turn with the remaining three of the four fixed at the standard values (cf. Table VI).

Uncertainties

The systematic uncertainties fall into two categories; the effects on the measured values resulting from uncertainties in input parameters, and the variations in the fitted parameters due to fit interval, cuts on the input spectrum, and in the case of the proton spectrum, the background scaling function. The uncertainties due to input parameters in the fit

are relatively easy to identify and to understand by changing the parameter and refitting the data. The systematic effects due to the cuts on the spectrum and the fitting interval were studied by fitting the same data with different cuts. When the variations on the fit parameters with cut value were small with respect to the other systematic and statistical uncertainties, the fit was considered to have converged.

Within the quoted errors, variations in temperature T , density ϕ , muon decay rate λ_0 , the detection efficiency ϵ (which was detector dependent), $\tilde{\lambda}_{\frac{1}{2}\frac{3}{2}}$, and ω_s did not cause variations in the values found for the fitted parameters. This was checked by varying the input values of the above by twice the uncertainty and observing the variation in the fit parameters. The uncertainty in the input values of $\tilde{\lambda}_{\frac{1}{2}}$, β_s , β_p , and P_s did have significant systematic effects.

The total systematic uncertainty on a fitted parameter was made by the addition in quadrature of the uncertainties due to the possible variations of the fixed input parameters. The systematic uncertainty associated with the proton background scaling function was handled in a different way. The uncertainty in the background scaling function was explicitly taken into account in the fitting function, and so the uncertainty due to the scaling is included in the statistical error evaluation. See the discussion surrounding Eq. (5.7) on page 69.

The statistical errors on the fitted values were found by making an asymmetric error evaluation around the best-fit value. The positive (negative) uncertainty was found by fixing the parameter in question, adding to it a guess of the uncertainty, and refitting the data with the parameter held fixed. The asymmetric error value was assigned the same value as the change necessary to increase the χ^2 of the fit by 1.0. Where the positive and negative uncertainties are the same, only one value is quoted.

Neutron Data Fits

Fits to the neutron data taken from the thick deuterium layer gave the results found in Table VII. The fitted value for the ϵ_a efficiency agrees with the value found by comparing

Parameter	Value
$\lambda_{\frac{3}{2}\frac{1}{2}}$	35.3 (+1.4, -1.3) μs^{-1}
$\lambda_{\frac{3}{2}}$	3.12 (+0.14, -0.11) μs^{-1}
$\phi_z \lambda_z$	0.288 (± 0.015) μs^{-1}
ϵ_a	0.14 (± 0.04) %
σ	1.48 (± 0.11) ns
$\chi^2/\text{dof (cl)}$	158/150 (55%)

Table VII: The kinetics values resulting from fits to the thick deuterium neutron spectrum (1560 Tl on each foil). The (cl) refers to the confidence level of the fit, the chance that another measurement would yield a worse (higher) value for χ^2 .

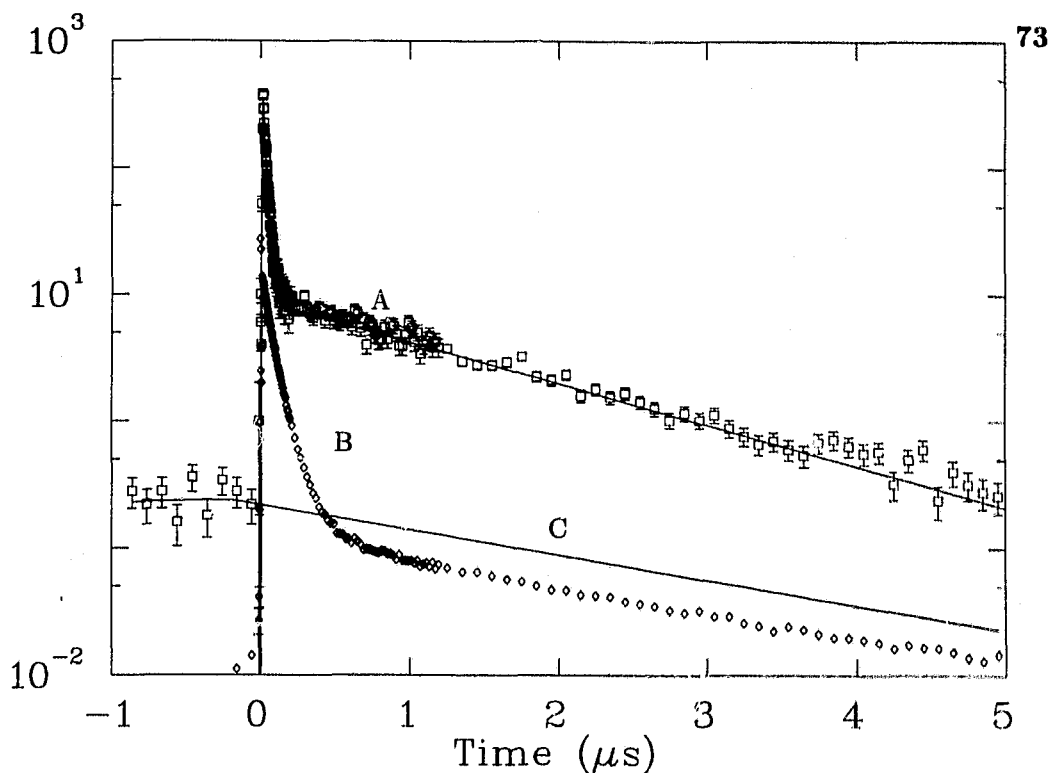


Figure 5.2.8: Neutron time data, and the fit to the data. Curve (A)(squares) is the data measured in the deLe spectrum. Curve (B)(diamonds) shows the level of the singles spectrum contribution via ϵ_a . Curve (C)(line) is the representation of the other backgrounds, fit by the constant approximation before time zero, and with the muon lifetime after time zero. The fitted contribution of the fusion neutrons is shown as the solid line passing among curve (A).

the counts in the energy spectrum above the fusion neutron cutoff with and without the deLe cut (see Fig. 5.2.1, page 60). The σ value for the time resolution of the detector yields a FWHM of 3.5 ns, close to the estimate of 4 ns arrived at earlier based on the flight times of 2.45 MeV neutrons in a 10 cm detector. From Fig. 5.2.8 it is evident that the treatment of $(n_{zone} + n_{electronic})$ as a constant is valid by considering the shape of time distribution before time zero.

Proton Data Fits

Fits to the proton data taken from both the thick and thin deuterium layers are summarized in Table VIII; the results of the fit for the thick target data are plotted in Fig. 5.2.9. The results for the thick deuterium given in the table are in reasonable agreement with the neutron results in Table VII. The signal-to-background ratio for the thick deuterium proton data was roughly 9:2, while the ratio for the thin deuterium data was much worse at 9:6, a three-times-higher background. The background scaling function was predicted using both the thick and thin protium layers and so, to check the systematic effects on the

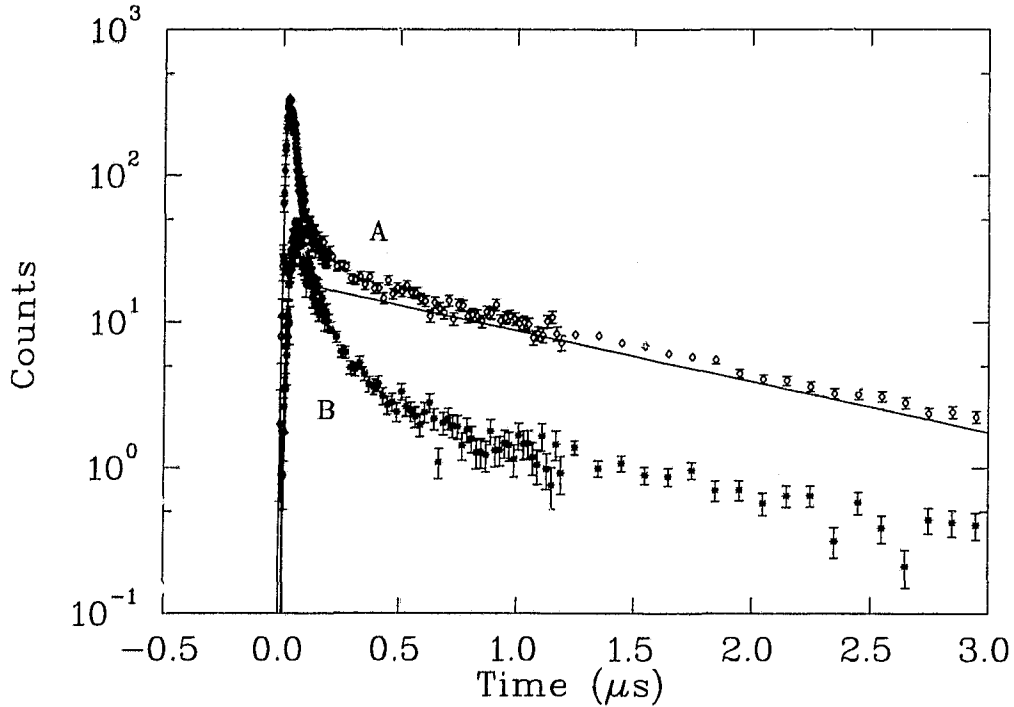


Figure 5.2.9: Proton time data for the thick deuterium (1560 Tl on each foil), and the fit to the data. Curve (A)(diamonds) is the data measured in the l energy region. Curve (B)(stars) shows the background as determined from the h energy region and the scaling function Eq. (5.7). The fusion contribution to the data is shown as the solid line.

fits, the two deuterium spectra were each fit with both of the scaling functions. The results of the fits showed that the thick deuterium data were not sensitive to the choice of background scaling, presumably due to the favourable signal-to-background ratio, while the thin deuterium fits fluctuated to the limits of the statistical accuracy. The data extracted from the thin deuterium targets were more sensitive to other effects such as μd escape from the layer and, from the value of $\phi_z \lambda_z$, suffered from a higher nitrogen contamination.

Parameter	Value: Thick D ₂	Value: Thin D ₂
$\lambda_{\frac{3}{2}}$	34.7 (+1.5, -1.4) μs^{-1}	38.6 (+3.1, -2.8) μs^{-1}
$\lambda_{\frac{3}{2}}$	2.77 (+0.12, -0.11) μs^{-1}	2.97 (+0.23, -0.21) μs^{-1}
$\phi_z \lambda_z$	0.340 (± 0.012) μs^{-1}	0.589 (± 0.024) μs^{-1}
σ	9.52 (± 0.28) ns	9.02 (± 0.36) ns
χ^2/dof (cl)	164/157 (33%)	162/157 (39%)

Table VIII: The values resulting from fits to the proton time spectra taken from both the thick (1560 Tl) and thin (312 Tl) deuterium targets.

Simultaneous Fits to Both n and p Spectra

The simultaneous fit of both the neutron and proton data from the thick deuterium target allowed one more parameter to be measured in addition to $\tilde{\lambda}_{\frac{3}{2}\frac{1}{2}}$, $\tilde{\lambda}_{\frac{3}{2}}$, and $\phi_z \lambda_z$. The choice of parameter to vary was limited to $\tilde{\lambda}_{\frac{1}{2}}$, β_s , β_p , and P_s : the kinetics equations were simply not able to predict the other parameters in any reliable way (cf. Table VI, page 71). All of the fits gave a χ^2 value of 325 for 309 degrees of freedom.

The four extracted parameters are dependent on the input values of the remaining three. With $\tilde{\lambda}_{\frac{1}{2}}$ and any two of P_s , β_s , and β_p fixed, the resulting value of the remaining physical parameter was found. The results of the fit, which yielded values for P_s , β_s , and β_p , as well as $\tilde{\lambda}_{\frac{3}{2}\frac{1}{2}}$, $\tilde{\lambda}_{\frac{3}{2}}$, and $\phi_z \lambda_z$, are given in Table IX.

The values of $\tilde{\lambda}_{\frac{3}{2}\frac{1}{2}}$, $\tilde{\lambda}_{\frac{3}{2}}$, and $\phi_z \lambda_z$ do not change when each of P_s , β_s , and β_p are alternatively varied with the remaining two of the three fixed at the standard values. This behaviour is expected from Eq. (A.5) which enters the kinetics as a distinct subformula. The large systematic uncertainty in the $\tilde{\lambda}_{\frac{3}{2}}$ value is due almost entirely to the uncertainty in the $\tilde{\lambda}_{\frac{1}{2}}$ input value.

Setting all three of P_s , β_s , β_p to the standard values allowed a measurement of $\tilde{\lambda}_{\frac{1}{2}}$, resulting in the values given in Table X. The systematic uncertainty in this case is dominated by the variations in the β_p value.

Although the experiment was not designed to make an absolute measurement of the yield, a consistency check on the number of fusion products has been made. The fit values of the kinetics parameters define a yield of neutrons and protons per muon stopped in the layer [see Eq. (2.14) on page 21]. The total number of protons and neutrons, coupled with the yield per muon, the efficiency values for the applied cuts, and the detector solid angle, can be used to reconstruct the number of muons stopped in the layer.

This number of muons can also be found by an examination of the GMU value for the run. A GMU muon is one which enters the target and stops somewhere, possible in the

Parameter	Value
$\tilde{\lambda}_{\frac{3}{2}\frac{1}{2}}$	34.2(8) _{stat.} (1) _{sys.} μS^{-1}
$\tilde{\lambda}_{\frac{3}{2}}$	2.71(7) _{stat.} (32) _{sys.} μS^{-1}
$\phi_z \lambda_z$	0.320(10) _{stat.} (1) _{sys.} μS^{-1}
P_s	0.47(8) _{stat.} (6) _{sys.}
β_s	0.487(15) _{stat.} (11) _{sys.}
β_p	0.563(14) _{stat.} (11) _{sys.}

Table IX: The kinetics values resulting from fits to the thick (1560 Tl) deuterium spectrum for both neutron and proton data. The value of $\tilde{\lambda}_{\frac{1}{2}}$ ($= 0.044 \mu\text{S}^{-1}$) was fixed during the fit.

Parameter	Value
$\tilde{\lambda}_{\frac{1}{2}}$	0.052(8) _{stat.} (3) _{sys.} μS^{-1}
$\tilde{\lambda}_{\frac{3}{2}\frac{1}{2}}$	34.0(8) _{stat.} (1) _{sys.} μS^{-1}
$\tilde{\lambda}_{\frac{3}{2}}$	3.21(51) _{stat.} (16) _{sys.} μS^{-1}
$\phi_z \lambda_z$	0.320(10) _{stat.} (1) _{sys.} μS^{-1}

Table X: The kinetics values resulting from fits to the thick deuterium spectrum for both neutron and proton data, with the goal of measuring $\tilde{\lambda}_{\frac{1}{2}}$.

hydrogen target, possible in the surrounding gold structure. The measured decay electron time spectrum reflects this ratio of muons decaying in gold, with an 80 ns lifetime, versus those decaying in hydrogen with a 2194 ns lifetime⁴. For the thick deuterium runs, there were 216×10^6 μ 's in the GMU scaler. The number stopping in the deuterium was found to be 0.576(13) of GMU, or 124×10^6 μ 's. Since the yield for neutrons based on Eq. (2.14) is 0.0713, there were 8.87×10^6 neutrons produced. Likewise, the proton yield per muon is 0.0619 so 7.70×10^6 protons are to be expected.

The neutron detector efficiency is composed of the intrinsic efficiency of the detector to 2.45 MeV neutrons and the limitations imposed by the cut on the pulse height (see Fig. 5.2.1). The value of the efficiency as calculated by Monte Carlo was about 0.010(2)⁵. In addition the del.e efficiency of 0.12 reduced the number of observed neutrons as well⁶. Taking these two factors into account implies that the neutron spectrum should contain about 10600 events. In actuality, 9800 events were seen, a number which is not inconsistent considering the uncertainty in the efficiencies.

The silicon detector had a solid angle of 0.019(2) again calculated by Monte Carlo. A correction for the energy window (see Fig. 5.2.3) was found by using the ratio of the counts within the signal energy cut to the total number of counts (this measured in the del.e data where the backgrounds are negligible), and this factor implies that 0.38(1) of the protons hitting the detector are in the selected energy region. These numbers imply that of the 7.70×10^6 protons produced, 55700 should be detected. Only 18000 protons were counted in total, implying that there is some other efficiency of roughly 30%, perhaps the ranging losses in the layer, which was preventing the protons from reaching the detector.

From Fig. 3.4.1, page 44, it can be seen that the protons detected by the silicon detector left the solid hydrogen layer at a large angle. For fusions deep in the layer, this increases the path length and hence the energy loss and attenuation. The range of a 3 MeV proton in hydrogen is roughly $6 \text{ mg}\cdot\text{cm}^{-2}$ and the thickness of the target layers for the thick deuterium was about $5 \text{ mg}\cdot\text{cm}^{-2}$ so protons exiting the layer normal to the target would do so from all depths of the target. At an angle of 70° however, the target has a total thickness of $15 \text{ mg}\cdot\text{cm}^{-2}$, and so fusions occurring deep in the layer would generate protons unable to reach the detector. Only the fusions in the front third of the target could escape the layer. Since the comparison was done only to check for consistency, no further effort was made to model the effect (via Monte Carlo or otherwise) and achieve an accurate estimate.

⁴This method of finding the stopping fraction is good provided the efficiency for the detection of muons decaying in gold is identical to that for muons decaying in hydrogen. For the del.e detection system used, this assumption is true at the 5-10% level.

⁵This value was supplied by P. Kammel, and includes none of the effects due to neutron absorption or re-scattering by the apparatus and hence the large uncertainty.

⁶There is a third effect coming from the limited length of the time window in which the data were collected, but this effect is at the 10% level.

5.3 Emitted Muonic Deuterium

The measurements made with the μ d emission targets were quite different in nature than those made for the pure solid deuterium targets. In the case of emission, a deuterium doped protium layer 1040 Tl thick was applied to the upstream foil while the downstream foil was bare. The emission measurements used only one third of the total quantity of hydrogen deposited during the pure deuterium experiment (2×1560 Tl). The thinner layer stopped fewer muons relative to the surrounding support structure, and the formed μ d had to exit the layer before any reactions gave an analyzable signal. Because of the lower stopping fraction of muons in hydrogen, and the addition of an emission probability before any possible fusion reaction, it was impossible to collect sufficient data for analysis using the neutron detectors. Only the silicon detector and wire chamber imaging yielded useful data. The analysis here uses only the silicon detector data collected by the commercial detector (S_{i2} data were not used). The information from the imaging detectors was outside the scope of this work.

Data were taken for five different surface layer thicknesses: 8, 16, 24, 35, and 50 Tl of pure D₂. The summary of the runs analyzed for the data presented here is given in Table V on page 52.

5.3.1 Proton Energy Spectra Features

Figure 5.3.1 shows the energy spectra as measured by the silicon detector over the region of the proton signal for the five different layer thicknesses. It is worth noting that as the surface D₂ layer thickness increases the width of the distribution increases and the center of the distribution shifts to a lower energy.

For each of the individual runs with surface D₂ layers (cf. Table V, page 52), four energy spectra were created based on time cuts. For the energy interval between channels 2600 and 3400 (2.6 MeV to 3.3 MeV) the energy spectra were collected for the following four conditions (a) all times, (b) $t < 20$ ns, (c) $20 < t < 100$ ns, and (d) $t > 100$ ns. These regions were chosen so that for (a) all data were available, (b) the early time background could be seen, (c) the early time proton signal energy distribution could be analyzed and (d) the later time proton signal energy distribution could be analyzed.

Initially, Gaussian distributions were used to fit to the peak shapes but, as expected, when the peak shape became broader than the intrinsic detector resolution, the Gaussian line shape was unable to represent all of the distributions. An asymmetric shape was chosen via the Physica TINA function:

$$\text{TINA}(x, a, b, c) = \frac{1}{2ce^{b^2/4c^2}} e^{\frac{x-a}{c}} \mathcal{E}\mathcal{R}\mathcal{F}\mathcal{C} \left(\frac{x-a}{b} \right) \quad (5.11)$$

This normalized asymmetric function was chosen for its ability to allow good fits to the data, and thus give an accurate measure of the integrated signal intensity. Since the nature

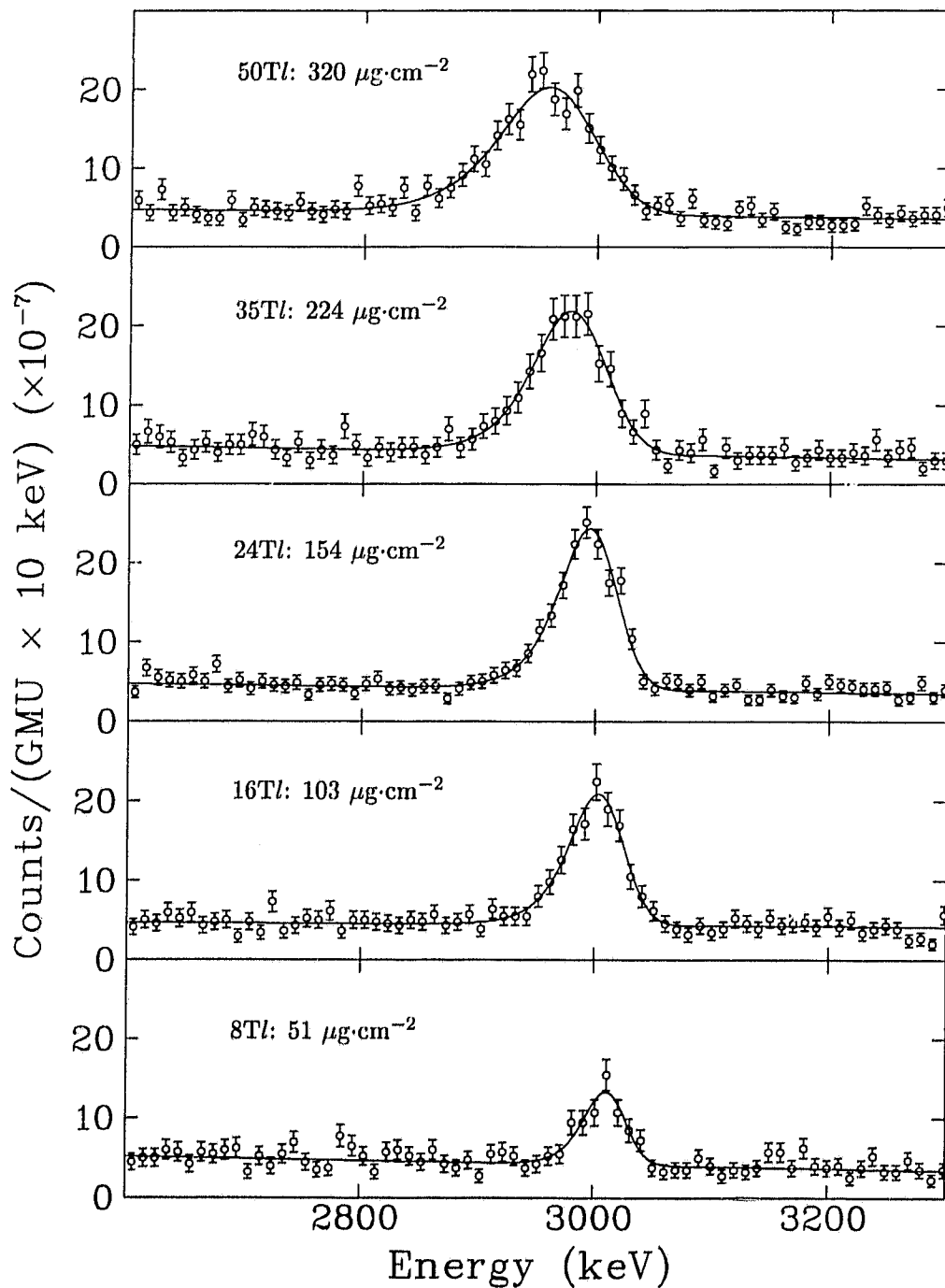


Figure 5.3.1: The energy spectra taken from the emission targets in the region containing the 3 MeV proton signal for times $t > 20$ ns. The variation in the proton signal as a function of the layer thickness can be seen.

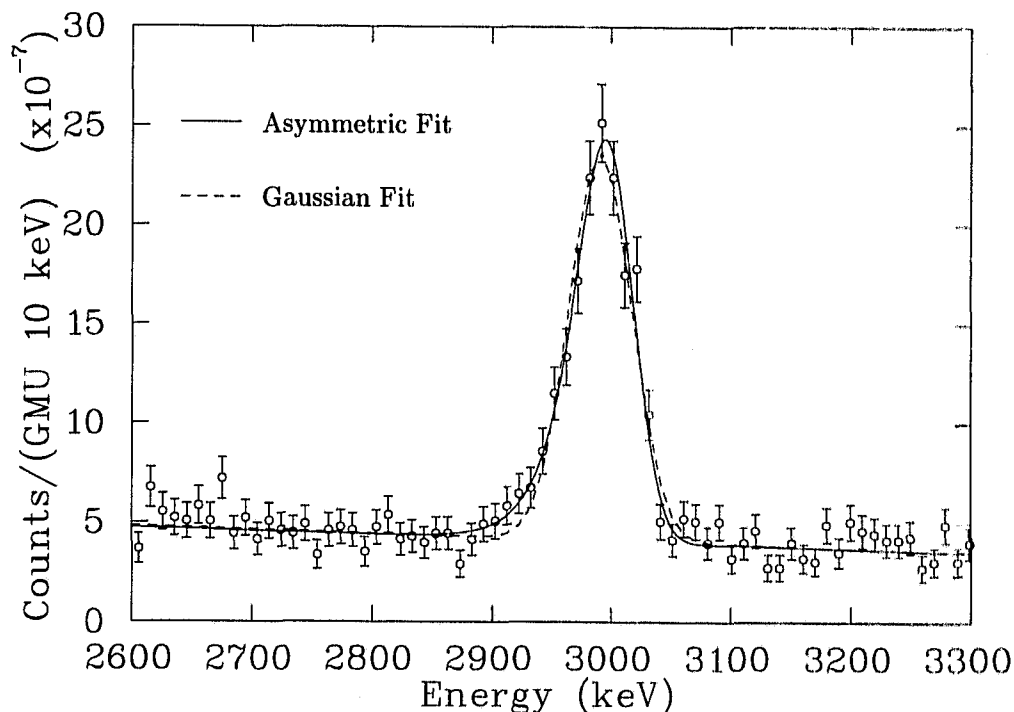


Figure 5.3.2: A comparison of the Gaussian and asymmetric fits to the 24 Tl surface layer energy spectrum. The difference in the fit to the low energy tail of the distribution is easily seen.

of the function yields strong correlations between the a , b , and c parameters, it was not a good method for finding the centroid of the energy signal. For that, the Gaussian fits were used since the asymmetry in the peaks is not extremely strong (cf. Fig 5.3.2).

The energy spectra were well fit by the asymmetric shape plus a linear background:

$$y = Y_i \cdot \text{TINA}(E, a, b, c) + b_1(E - 3000) + b_2, \quad (5.12)$$

where Y_i is the yield of signal found, and the linear background was fit about energy channel 3000 to help remove the correlation between the b_i parameters and to make the integral of the background about any interval symmetric to the offset simply the interval width multiplied by the b_2 value⁷.

After all of the spectra were fit to the expected energy shape given by Eq. (5.12) the observation was made that the background parameter b_1 (slope) did not change in a systematic way with time, and that to within the sensitivity of the fit to the centroid, there was no time dependent shift in the energy peak, an effect which would occur if the distribution of fusion position in the surface layer was time dependent.

The proton yields measured in the runs numbered 1122-1130 were strongly suppressed in comparison to the yields from seemingly identical targets in runs 1131-1153 (cf. Table V,

⁷Remember that $b_1(E - 3000)$ is an odd function about $E = 3000$.

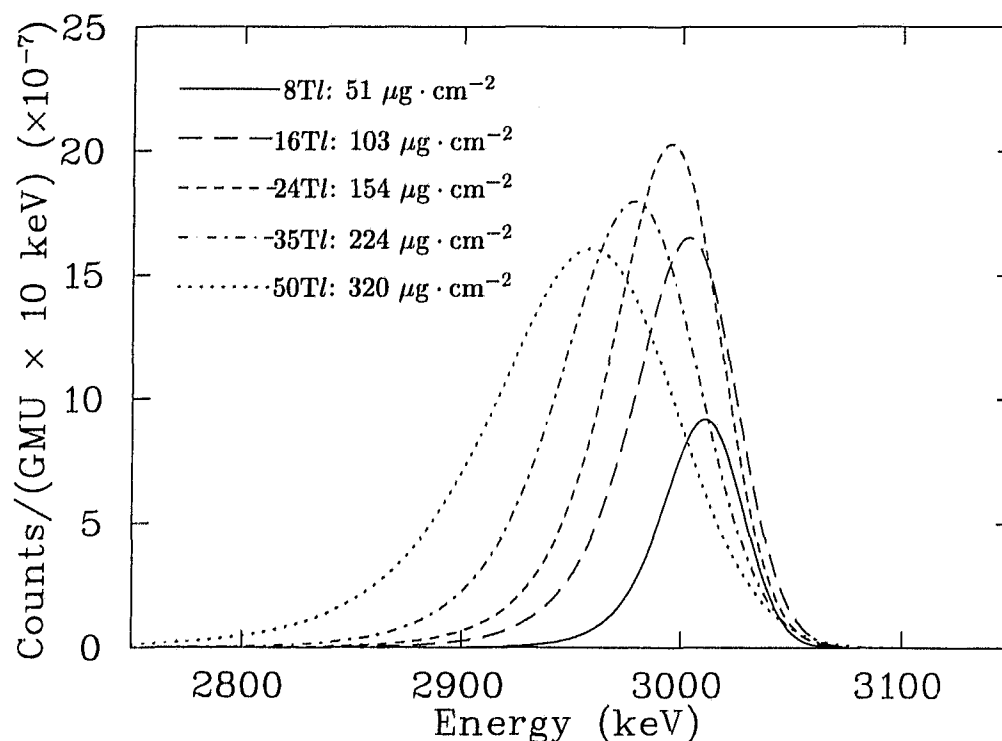


Figure 5.3.3: A plot of the curves fitted to the energy distributions for the successive surface layers. The centroid shift to lower energy, as well as the broadening of the signal, is clearly visible.

page 52). The Germanium spectrum taken during the runs show that there was a nitrogen contamination in the target used for runs 1122-1130 [59]. These runs were dismissed in favour of the runs which contained analyzable data.

Based on the fits to individual runs, the optimum time range for the signal from fusion protons was chosen to be $t > 20$ ns, which kept all of the signal, but removed the contribution from background before fusion signals were detected thus increasing the signal to background ratio. The individual runs which passed all of the consistency checks derived from the scaler values and which had no indications of having been affected by the S_{i2} position were used to provide the data for analysis. For separate runs with identical surface layers, the data were summed before analysis. The summed data sets, which are referenced by the surface layer thickness, were then normalized to the respective GMU scaler and used for further analysis. (It is in fact the summed data which is presented in Fig. 5.3.1.)

Figure 5.3.3 shows the curves resulting from the fits to the proton signal energy distributions. The shift to lower energy of the centroid, and the general broadening of the signal are clearly seen as the surface layer thickness increases.

The summed data sets were fit to the model of a yield signal (either Gaussian or asymmetric) plus a linear background signal [Eq. (5.12)] to give the best values of the

Layer	Centroid (channel)		Yield $\times 10^{-6}$		(cl) %	
	G	A	G	A	G	A
8	3063.1(2.2)	3059(22)	5.0(0.6)	4.4(0.5)	50	58
16	3053.9(1.5)	3054(9)	9.8(0.6)	10.3(0.5)	30	99
24	3045.4(1.2)	3046(8)	13.3(0.6)	13.4(0.6)	65	36
35	3027.6(2.5)	3023(15)	15.7(1.1)	15.0(0.8)	31	97
50	3004.4(2.6)	3005(16)	19.0(1.1)	17.8(0.9)	3	63

Table XI: A comparison of the Gaussian (G) and asymmetric (A) fit values for the key parameters of yield and centroid. The confidence levels (cl) for the fits are also given (probability of obtaining a worse value of χ^2/dof).

yields. In addition, the parametrizations of the signal and background shapes were saved since it was information required to properly complete the time signal analysis.

Table XI gives a comparison of the Gaussian and asymmetric fit parameters taken from the data. It is clear from the examination of the confidence level (i.e., the probability of obtaining a worse fit) that the Gaussian fit works well for the thin layers, but less well for the thicker layers.

The asymmetric fit yields have been used, along with the respective layer thicknesses, as points on the effective interaction curve defined by Eq. (2.15), repeated here:

$$Y = A_1 (1 - e^{-d/k}) + A_2 d. \quad (5.13)$$

Figure 5.3.4 shows the data, as well as the fits allowed by Eq. (5.13), for fixed values of the direct stop yield. The fitted parameters are summarized in Table XII. To account for the direct stopping of muons in the D_2 surface layer, three variations of the fit were made for arbitrarily chosen fixed A_2 values.

In addition, the effects arising from the known surface layer nonuniformity were investigated. The different values of the δd parameter were used as a simple way to understand the effect on the fitted parameters due to variations in the surface layer thickness. Although the actual thickness profile of the solid target layer has been measured for the central vertical section, the horizontal thickness profile is unknown (cf. Ref. [53]). The fusion protons are generated at some depth (z) in the surface D_2 layer and with an x y position distribution presumably reflecting the position intensity of stopped muons (emitted μd should not move large distances in the x y plane from the initial muon stop position). The silicon detector acceptance for the protons is a strong function of the x y position due to the perpendicular geometry of the detector to the target (cf. Fig. 3.4.1). The measured protons represent a convolution of the D_2 layer thickness profile, the position distribution of the emitted μd (as well as the average interaction depth), and the position dependent acceptance of the silicon detector. Allowing an uncertainty in the average thickness of the layer is the easiest way to account for this effect.

Because of the exponential dependence on the thickness d , even a small uncertainty

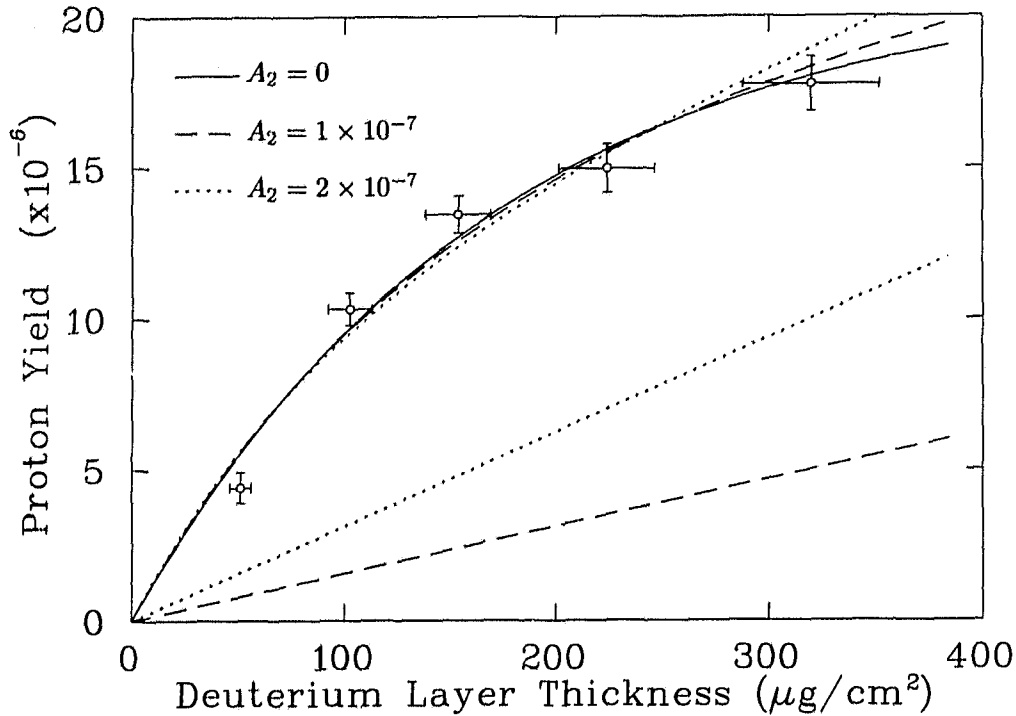


Figure 5.3.4: A plot of the yield as a function of the surface layer thickness, as well as fits to the yield given an assumption of the yield from direct stops (shown as the straight lines). Each of the fits defines an effective interaction length. The uncertainty shown on the thickness is 10%.

δd	A_2 (fixed)	k ($\mu\text{g} \cdot \text{cm}^{-2}$)	χ^2/dof (cl)
0%	0	168(40)	9.9/4 (4%)
	1×10^{-7}	126(36)	11/4 (2%)
	2×10^{-7}	88(36)	14/4 (0.6%)
5%	0	180(190)	1.0/4 (90%)
	1×10^{-7}	122(63)	1.2/4 (88%)
	2×10^{-7}	66(28)	3.4/4 (49%)
10%	0	179(370)	1.0/4 (91%)
	1×10^{-7}	122(115)	1.0/4 (90%)
	2×10^{-7}	60(32)	2.0/4 (75%)

Table XII: The effective interaction length derived from fits to the yield data for fixed values of the direct stop contribution A_2 [cf. Eq. (5.13)]. The addition of the small variation in the layer thickness has a dominant effect on the evaluation of the fits.

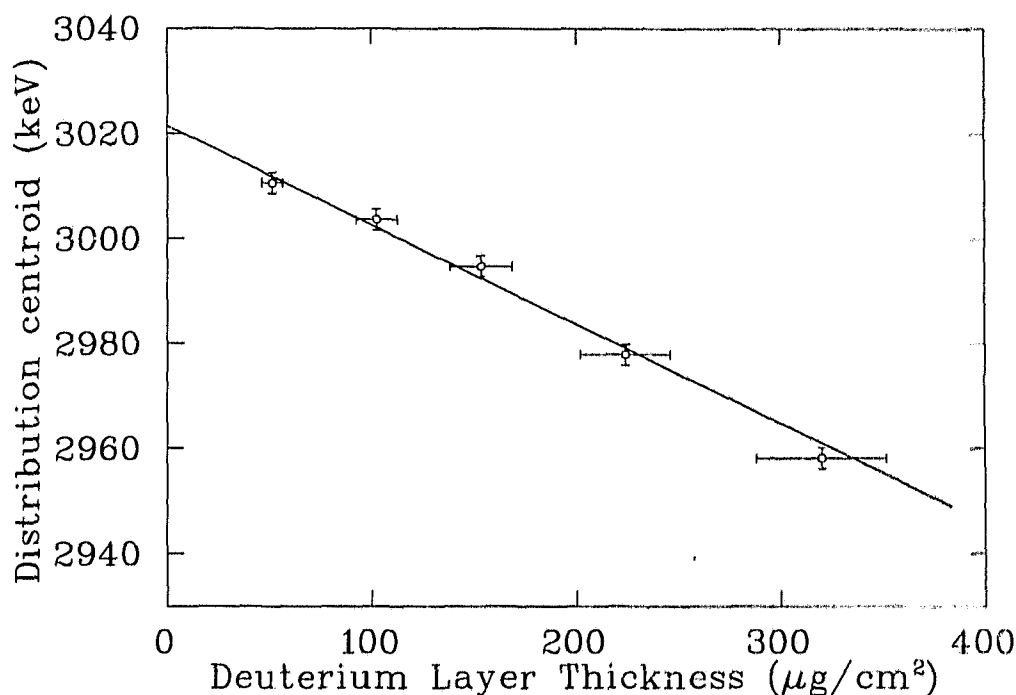


Figure 5.3.5: A plot of the energy distribution centroids as a function of the surface layer thickness, as well as linear fits to the thickness dependence. The points are taken from the Gaussian centroid values in Table XI and plotted with a 10% uncertainty in the thickness.

δd	slope ($\text{keV} \cdot \mu\text{g}^{-1} \cdot \text{cm}^2$)	Intercept (keV)	χ^2/dof (cl)
0%	-202(9)	3023(2)	3.3/3 (36%)
5%	-197(12)	3022(2)	2.3/3 (51%)
10%	-191(12)	3021(2)	1.3/3 (73%)
15%	-188(14)	3021(2)	0.7/3 (85%)

Table XIII: Values of the linear coefficients derived from fits to the data in Fig. 5.3.5. The fits are reasonably insensitive to the uncertainty in the layer thickness. The uncertainty in the slope does not include the systematic uncertainty in the conversion from Tl to $\mu\text{g} \cdot \text{cm}^{-2}$.

makes a large change in the evaluation of χ^2 . It does not, however, have a large effect on the measured k parameter, the variations of which are dominated by A_2 . The assumed 5 and 10% uncertainties are not unreasonable when compared to the measured nonuniformities in the frozen films [53].

It is clear that the measured data were insufficient to determine the three parameters in the model. Since the surface layer measurements were not continued for layers thicker than 50 Tl ($320 \mu\text{g} \cdot \text{cm}^{-2}$), the curve does not contain data which clearly indicates saturation. Because of this, the data do not allow an unambiguous determination of the A_2 parameter. A review of the analysis performed during the data collection indicates that the broadening and asymmetry in the peak prevented a proper measure of the yield. This

effect systematically lowered the yield at thick surface layers giving the impression that the curve had saturated. The thicknesses which were chosen for the experiment were determined by a calculation of the interaction length of a μd incident on deuterium nuclei (based on the cross sections of Bracci *et al.* [11]). Using the calculated value of the cross section, $2 \times 10^{-19} \text{ cm}^2$, and $6.4 \mu\text{g} \cdot \text{cm}^{-2} \cdot \text{Tl}^{-1}$ for the deuterium thickness, the derived interaction length for scattering reactions at normal incidence is 2.5 Tl . The data were collected for layers which exceeded that value by a factor of 20.

The effective length parameter represented by the k in Eq. (5.13) is not a simple interaction length. The emission of μd occurred with some angular distribution and as such the measured effective length includes an averaging over the distribution. It is possible that the chosen surface layers were such that only μd atoms emitted at relatively high angles had a significant probability of interaction. As the layer thickness was increased, the emission angles required to give an effective thickness leading to a fusion reaction would decrease and more of the emitted μd would generate fusion signals. This type of effect would mean that the probability of fusion for an emitted μd would increase with the emission angle. Thus the fusion yield depends on the angular distribution of the μd as well as on the simple fusion interaction length (distance a μd travels on average before fusion occurs). Effects such as this can only be verified by more extensive experimentation, and by simulation of the process by the Monte Carlo method. In any case, the interpretation of the k parameter should not be assumed trivially.

The centroid value and FWHM of the energy distributions contain information on the average depth of proton production in the different layers. Since the Bethe-Bloch energy loss for heavy charged particles is relatively well known, it is possible for a Monte Carlo which accurately reproduces the interaction point in the layer to make a prediction as to the shape of the resulting distribution. Figure 5.3.5 illustrates the shift in the centroid as a function of surface layer thickness. Table XIII gives the results of the fit for different assumed values of the layer nonuniformity. The shift is linear in the layer thickness and not sensitive to the variations in the layer thickness. A fit of the curve to the points gives the equation:

$$C = -202(22) \frac{\text{keV}}{\text{mg} \cdot \text{cm}^{-2}} \times d + 3022(2) \text{keV}, \quad (5.14)$$

where the possible effect of layer nonuniformity has been ignored, $\delta d = 0$, and the uncertainty is dominated by the conversion factor from Tl to $\mu\text{g} \cdot \text{cm}^{-2}$.

Unfortunately, the interpretation of this equation is difficult due not only to the fact that the protons are produced in a distribution throughout the surface layer, but that the protons which were detected had traveled at some angle through the remaining layer before being detected, and that angle depends on the geometrical position of the fusion with respect to the silicon detector. Monte Carlo calculations would be required for any accuracy, and the result is of questionable value.

A consistency check of the measured slope can be made. The measured value of the

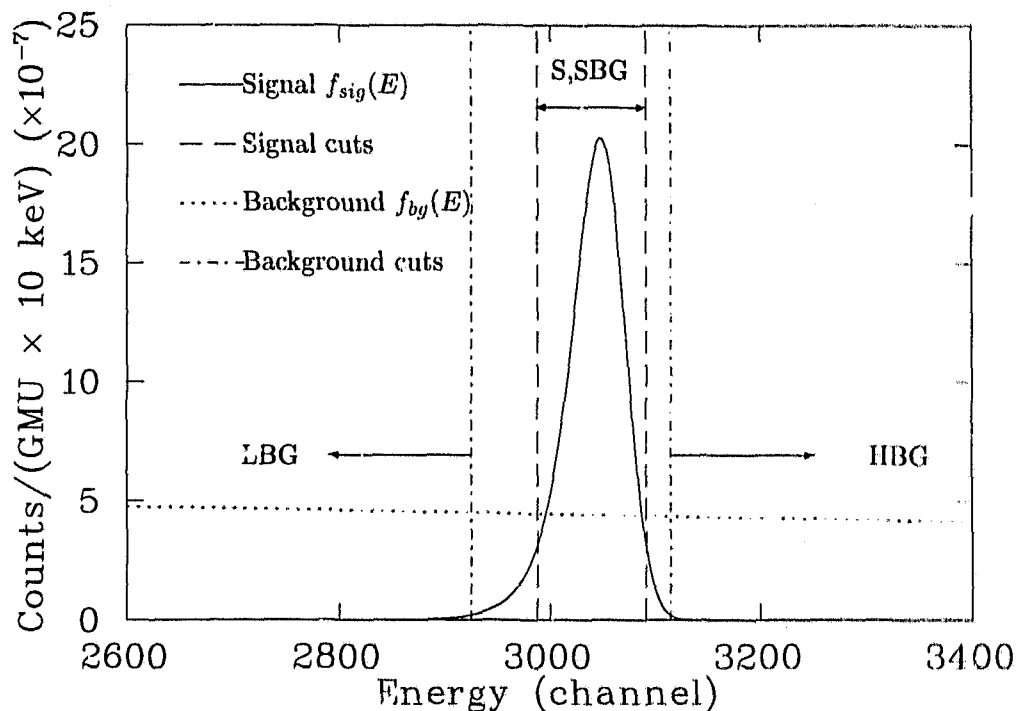


Figure 5.3.6: A plot of the signal and background curves found by the fit to the ^{24}Tl ($154 \mu\text{g} \cdot \text{cm}^{-2}$) data. Also shown are the cuts which define the time signal selection region (S, and SBG), the lower energy background region (LBG), and higher energy background region (HBG).

energy loss is 1.4 times larger than the generally accepted value for energy loss of a 3 MeV proton in deuterium ($140 \text{ keV} \cdot \text{mg}^{-1} \cdot \text{cm}^2$). If this difference were to correspond to an angular effect, the protons would be traversing the D_2 surface layer⁸ at an angle of about 70 degrees from normal. From Fig. 3.4.1, this angle between the normal to the target and the silicon detector position is not unusual and is consistent with the angle derived from the absolute yield calculations for protons from the thick solid D_2 layers.

5.3.2 Proton Time Spectra Features

The fits detailed above for both the proton signal energy spectra and the background spectra served a very important function in the determination of the time spectra to be analyzed. Since the number of signal counts was often limited, an attempt was made to optimize the signal-to-background ratio in the time spectra, and to provide a high confidence method of predicting the time dependent background which would be found contributing to the signal spectra.

Figure 5.3.6 illustrates the energy cuts associated with the selection of the time spectra

⁸And assuming that the protons really only traverse half of the layer, i.e., the average proton is produced in the middle of the surface layer.

to be analyzed. Given energy limits, the integrated energy function is equal to the total intensity of the time spectrum selected by the energy limits. The choice of the energy window from which to take the time spectrum of the proton signal was based on a figure of merit (FOM) which examined the total intensities of the time spectra as a function of the energy cuts which defined it. Once the signal window cuts were determined, the background contribution to the signal spectrum had to be accurately predicted.

Since both the proton signal and the background were parametrized as a function of energy for each surface layer, it was possible to examine the predicted signal intensity with respect to the background for any given set of energy window limits (c_1, c_2). The FOM used to decide on the values of the limits consisted of three factors⁹. The first was simply the signal-to-background ratio, and provided a term which was optimized for very thin energy windows centered on the energy peak. To maintain sufficient statistics, two factors which were optimized for larger energy windows were included. The first was the ratio of the signal selected in the window (i.e., the intensity of signal contained between c_1 to c_2) to the total available signal (the yield); the second was the relative decrease in precision of the selected signal. Defining the ratio of signal intensity between the $[c_1, c_2]$ limits to the total available signal (the yield) as a where:

$$a = \frac{\int_{c_1}^{c_2} f_{sig}(E) dE}{Y_i}, \quad (5.15)$$

then the FOM was:

$$\text{FOM} = \frac{a}{\sqrt{a^2 + (1-a)^2}} \frac{\int_{c_1}^{c_2} f_{sig}(E) dE}{\int_{c_1}^{c_2} f_{bg}(E) dE}. \quad (5.16)$$

The factor a in the numerator, and the ratio of the integrals of the proton signal counts, $f_{sig}(E)$, to background counts, $f_{bg}(E)$, are relatively straightforward to understand. The denominator $\sqrt{a^2 + (1-a)^2}$ measures the relative decrease in precision. For example, if $a = 0.5$, then the relative uncertainty in the selected signal is 1.41 times larger than in the full signal. This is based on the assumption that if $x \pm \delta x = y \pm \delta y + z \pm \delta z$ and $y = z = 0.5x$ then $\delta y = \delta z = \sqrt{2} \times \delta x$. This is a reasonable assumption when the quantities involved are counts which follow the $n \pm \sqrt{n}$ rule. This term was included in an effort to suppress large increases in the uncertainty of the intensity of the resulting time spectrum.

The FOM was examined as a function of the region where the proton signal was at least r times bigger than the background, and r was varied until the FOM was maximized. Table XIV summarizes the findings, and lists the energy cut values for each of the surface layers. Since it was necessary to make a prediction of the time signal of the background found under the proton signal, the energy regions close to the proton signal, where the

⁹This FOM was not derived in any more detail than a general optimization of the signal to background intensity ratio simply because the connection between the fit parameters in the time spectra, i.e., the things for which the selected data should be optimized, and the energy cut values is not a trivial function.

Layer (Tl)	Ratio $\frac{sig}{bg} > \dots$	bgll < LBG < bgllh		c_1 < SBG < c_2		bgll < HBG < bgllh		$\frac{I_{sbg}}{I_{lbg} + I_{hbg}}$
		bgll	bgllh	c_1	c_2	bgll	bgllh	
8	0.35	2600	2983	3023	3097	3114	3400	0.105(2)
16	0.55	2600	2942	2999	3098	3120	3300	0.184(6)
24	0.75	2600	2925	2988	3092	3115	3400	0.166(4)
35	0.70	2600	2887	2959	3088	3118	3400	0.222(10)
50	0.55	2600	2812	2911	3086	3124	3300	0.440(22)

Table XIV: A summary of the results from the figure of merit cut on the energy selection window. The values in the table denote energy channel number, and the column headings are explained in the text.

proton signal was less than 1% of its peak intensity, were chosen to supply the background time spectra.

Time spectra were collected for the three energy windows defined by the limits presented in Table XIV (cf. Fig. 5.3.6). The time spectra will be referred to as T_{lbg} , T_s , and T_{hbg} , which were collected from the LBG, (S,SBG), and HBG regions respectively. The time spectrum T_s contains not only the signals from the protons produced by fusions following the emission of μd atoms, but a contribution, T_{sbg} , from the background as well.

To predict the intensity of the background time spectrum, the integrals with respect to energy of the parametrized background function were found for the three regions; they will be referred to as I_{lbg} , I_{sbg} , and I_{hbg} . For comparison, the sum of the counts in the energy spectra over the LBG and HBG regions were taken as well, and will be referred to as E_{lbg} and E_{hbg} . Since it was simple to extract uncertainties for the sums of the experimental data, those uncertainties were assumed to apply to the calculated values for I_{lbg} and I_{hbg} ¹⁰. A test was done to see how consistently the total intensity, E_{hbg} , of the T_{hbg} time spectrum could be predicted from the expression:

$$E_{hbg} = E_{lbg} \frac{I_{hbg}}{I_{lbg}}, \quad (5.17)$$

and this was found to be accurate to better than 6%, which was consistent with the uncertainties in the data. Based on this, a weighting formula was developed to predict the intensity of the background which would be found in the signal (SBG) region. From this weighting, the actual time structure of the background was predicted to be

$$T_{sbg} = \frac{I_{sbg}}{I_{lbg} + I_{hbg}} (T_{lbg} + T_{hbg}). \quad (5.18)$$

It is the above ratio of I 's which is shown in the last column of Table XIV, along with an uncertainty derived from the experimental data. Since the background scaling

¹⁰Since the data were normalized to the GMU value, so were the fitted functions, so assigning uncertainties to the integrated fitting functions from scratch was more work and contained no more information than using the readily available uncertainties from the data.

Layer Tl	Amplitude N $\times 10^{-7}$	Rate Λ (μs^{-1})	t_0 (ns)	σ (ns)	cl
8	1.0(2)	13.6(2.6)	42(9)	12(10)	11%
16	2.7(2)	17.9(1.4)	54(6)	20(3)	91%
24	3.4(3)	17.1(1.4)	48(7)	20(3)	24%
35	3.9(3)	17.3(1.6)	43(4)	17(fixed)	36%
50	4.7(3)	15.7(1.0)	38(4)	15(3)	80%

Table XV: A summary of the fits of a single exponential to the emission data time spectra using Eq. (5.19). Compare the "late" t_0 and large σ values here with the values found from the background spectra (Table XVI).

is generally less than 1, and has a small uncertainty, it allows the time spectrum of the background, T_{sbg} , which contributed to the time signal T_s , to be known with relatively good precision.

The time spectrum data in T_s , for each of the different surface layer thicknesses, were fit to a single exponential decay

$$T_s = T_{sbg} + N \exp[-\Lambda(t - t_0)]. \quad (5.19)$$

For the actual fit, the exponential function was convoluted with a detector resolution and a step function indicating the muon arrival; see Appendix C on page 116. Two interesting effects were observed (cf. Table XV). The first was that the lifetime Λ chosen by the fit was the same, within uncertainties, for all of the different surface layer thicknesses. The second effect was that the fitting produced an unreasonably large detector resolution, 50 ns FWHM, and a t_0 value which was delayed when compared to the time resolution and t_0 value visible in the background.

The characteristics of the fit at early times are indicative of growth and decay effects and so the toy model of emission was employed (cf. §2.2.2). Since the lifetimes of the individual fits were very similar, the time spectra from the different surface layer thicknesses were summed to give a time spectrum with good statistics, referred to as τ_s . The individual T_{sbg} were summed to produce the overall background time spectrum, called τ_{sbg} .

To find the real detector resolution and t_0 value, the background spectrum τ_{sbg} was fit to a sum of three functions, a delta function at t_0 , and two exponential decay rates, Λ_1

Amplitudes $\times 10^{-6}$ /GMU			Λ_1	Λ_2	t_0	σ	χ^2/dof
Gaussian	Amp ₁	Amp ₂	(μs^{-1})	(μs^{-1})	(ns)	(ns)	
1.778(84)	17.6(1.3)	7.5(1.1)	11.8(1.5)	2.52(23)	20.64(50)	9.99(30)	3.67/14

Table XVI: The time signal background fit results. The time zero, t_0 , and detector resolution, σ , are accurately defined by this fit. The curiously low χ^2/dof , partially due to the uncertainty in the scaling factor in Eq. (5.18), implies that the uncertainties in the data are somehow overestimated by a factor of 2. The t_0 and σ values are independent of global scaling in the uncertainties.

Fit #	Amplitudes $\times 10^{-6}$ / GMU			R_1 (μs^{-1})	R_2 (μs^{-1})	δt (ns)	bgs	χ^2/dof (cl)
	Gaussian	K	$acorr$					
1	0	256(45)	0.98(18)	16.6(1.3)	64(23)	0	1	31/17 (2%)
2	1.0(7)	247(31)	1.59(69)	16.4(1.0)	88(34)	0	1	25.6/16 (6%)
3	0.7(4)	226(26)	1.25(50)	16.4(1.0)	97(43)	5	1	25.0/16 (7%)
4	0.8(3)	206(22)	0.97(50)	16.3(1.0)	112(71)	10	1	24.7/16 (8%)
5	0.6(6)	272(45)	1.46(49)	18.0(1.5)	77(26)	0	1.22(10)	20.0/15 (17%)
6	0.3(4)	245(36)	1.20(35)	17.9(1.4)	83(31)	5	1.22(10)	19.5/15 (19%)
7	0.3(3)	220(29)	0.96(34)	17.7(1.5)	95(48)	10	1.21(10)	19.3/15 (20%)
8	0.4(4)	198(26)	0.62(35)	17.6(1.4)	103(92)	15	1.21(10)	20.1/15 (16%)

Table XVII: A summary of the attempts to fit the toy model to the emission data. The Gaussian amplitude referred to a Gaussian centered at the t_0 value; δt was an offset allowing the proton signal growth to begin later than the t_0 value; bgs was a multiplier on the amount of background τ_{sbq} permitted in the fit; and $acorr$ is the relative ratio of the amplitudes of the two exponentials. A number presented without an uncertainty was held fixed during the fit.

and Λ_2 . After the convolution with the detector resolution, the delta function became a Gaussian with the same width as the detector resolution. The fit worked well and found the values given in Table XVI for the resolution and time zero.

The function used to fit the emission data was based on the toy model approximation Eq. (2.25), with three added features. The first was the appearance of a delta function at the t_0 position. After the convolution with the resolution function, the delta function became a Gaussian $\mathcal{G}(t-t_0)$ capable of modelling the protons produced by the direct stops of muons in the D_2 surface layer. Based on the information available from the thick D_2 layers, the muons stopped directly in the surface layer would produce protons with a lifetime of about $50 \mu\text{s}^{-1}$, with a yield per muon which was reduced due to the possibility that the μd would escape the layer. The fitting function for such a rapid lifetime, after convolution with the detector resolution, contains more information on the detector resolution than on the kinetics of the fusion resulting from direct stops. Thus only an amplitude was necessary to model the contribution from direct stops.

The second added feature was the possibility of a delay time, δt , in the onset of the exponential growth and decay curve. This was permitted in the fitting equations to allow for a delay in the arrival of the first μd atoms, a correction which should help the modelling of emission as a rate. Lastly, the possibility of multiplying the background τ_{sbq} by a global scaling factor, bgs (which was normally fixed at 1) was allowed. The fit equation was then:

$$\tau_s = K \left[e^{-R_1(t-t_0-\delta t)} - acorr \times e^{-R_2(t-t_0-\delta t)} \right] + G_{amp} \delta(t-t_0) + bgs \times \tau_{sbq}. \quad (5.20)$$

With the t_0 and detector resolution fixed at the values found from the background, the equations for the emission model, Eq. (5.20), after convolution, were fit to the data to find values for the decay lifetime R_1 and growth lifetime R_2 , as well as the relative amplitudes of the two exponentials, $acorr$. The fitting function used the integrated form

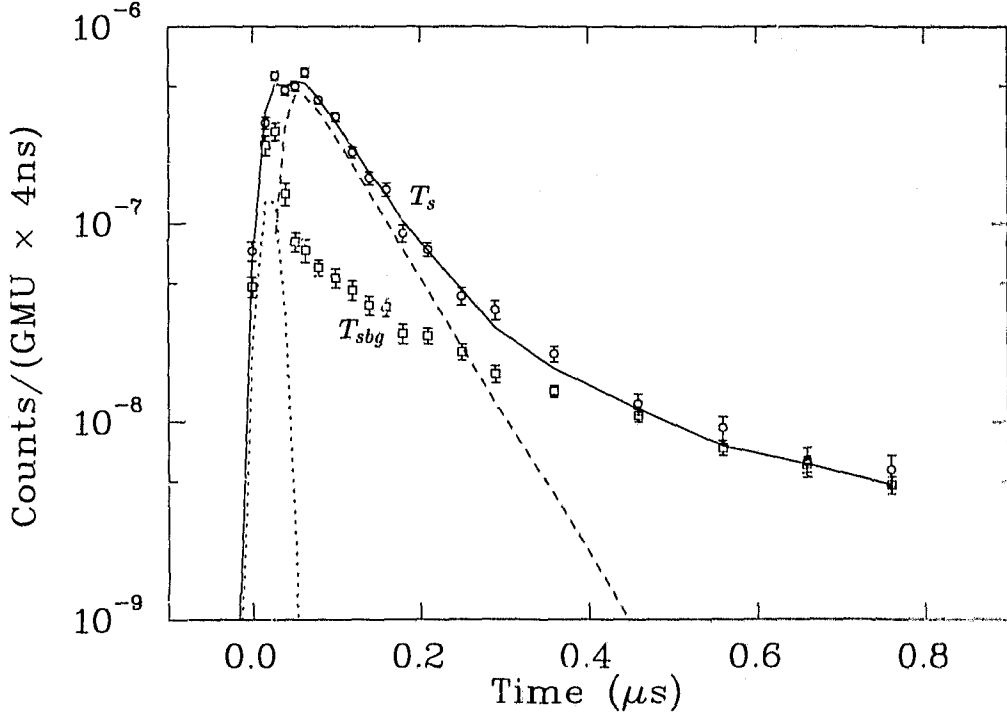


Figure 5.3.7: The τ_s (circles) and τ_{sbg} (squares) data, along with the best fit to the data (solid line, fit #2, Table XVII). The fit curve is made from the Gaussian at t_0 (dotted line), the τ_{sbg} , and the growth and decay curve (dashed line).

of the convolution to ensure that the finite width of the time bins had minimal effect on the fitted parameters (see Appendix C, page 116). The results of the fit are summarized in Table XVII. A plot of the data and the fit are shown in Fig. 5.3.7.

Reviewing the interpretation of the toy model via Eq. (2.28), and ignoring any possible effect of high Z contamination, it can be seen that the following relations should hold among the parameters in Table XVII if the model is viable.

$$R_1 \approx \lambda_o + \phi c_p \lambda_{p\mu p} + \phi c_d \lambda_{pd}, \quad (5.21)$$

$$R_2 - R_1 \approx \lambda_e - \phi c_d \lambda_{pd} + \phi c_d \lambda_{mf}, \quad (5.22)$$

$$acorr \approx 1 + (\lambda_e - \phi c_d \lambda_{pd} + \phi c_d \lambda_{mf}) \frac{\phi_d \lambda_{mf} + \lambda_{escape} + \tilde{\lambda}_f}{(\phi_d \lambda_{mf} + \lambda_{escape}) (\tilde{\lambda}_f)} \quad (5.23)$$

The R_1 value is relatively constant for all of the different variations of fitting conditions. Only the background scaling has a large effect, and it is still within the statistical uncertainties. The interpretation of the R_1 value as the μp disappearance rate will be commented on in the conclusions Chapter.

The difference between the rates $R_2 - R_1$ is, without exception, positive, and at least three times larger than the R_1 value itself. This has two consequences for the interpretation of the model. The first is that $\lambda_e + \phi c_d \lambda_{mf} > \phi c_d \lambda_{pd}$, which is consistent with the

assumptions required to model the emission as a rate. The second is that the value of $acorr$ should be greater than unity, which is only strictly true for fits #2, 3, 5, and 6. However, the large uncertainty in the $acorr$ and R_2 values permits consistency with the model (as well as destroys the predictive power of the model).

The $acorr$ and R_2 values have large uncertainties due primarily to the time resolution of the detector. With a resolution of 24 ns FWHM, the measurement of events that are occurring faster than $40 \mu s^{-1}$ becomes difficult, and sensitivity to the process is quickly lost. In addition to that, the early time data so critical to the determination of the factors has a strong contribution from the background, and an unknown contribution from fusions from direct stops.

Increasing the background contribution by 22% increases the quality of the fit (as is visible for fits #5-8), but such an increase is larger than the worst case uncertainty on the prediction of τ_{sbg} by a factor of three [cf. Eq. (5.17)], and is thus difficult to justify.

Allowing the proton signal from emission to start at a time later than the t_0 time (via the δt parameter) improved the quality of the fit by a small margin, but it decreased the value of $acorr$ and increased the values of R_2 . Since $acorr$ contains an $R_2 - R_1$ factor, a decrease of $acorr$ is inconsistent with an increase in R_2 . Overall, the emission model cannot be judged to have been entirely successful in its ability to fit to the data.

5.4 Monte Carlo Simulations

The complexity of the processes involved in the time evolution of a muonic atom in hydrogen poses an intractable problem for exact analysis. However, since the individual reactions involved are believed to be well understood, and calculations for each step have been carried out yielding either cross sections or rates, the processes are readily simulated by the Monte Carlo method.

Two Monte Carlo programs were used to aid in the analysis of this experiment. The first was designed and written by A. Adamczak and assumes an infinite homogenous target volume [44]. This specific Monte Carlo has no ability to model geometrical effects such as a muonic atom leaving one target layer and entering another, but it does use cross sections which were calculated explicitly for muonic atoms in a solid target. Since the calculation of the full set of cross sections of the processes in solid is still underway as this present work is prepared, the Monte Carlo was used only for the case where calculations existed, that is, for muons in pure deuterium.

The second Monte Carlo used in the analysis was written by V.E. Markushin [60-62]. This Monte Carlo considers a simple geometry with layer divisions along the z -axis, but there is no modelling of effects due to finite x - y distributions. Currently the program uses only the nuclear scattering cross sections (i.e., muonic atoms incident on free nuclei) and thus will not correctly account for solid state effects. It should, however, work reasonably

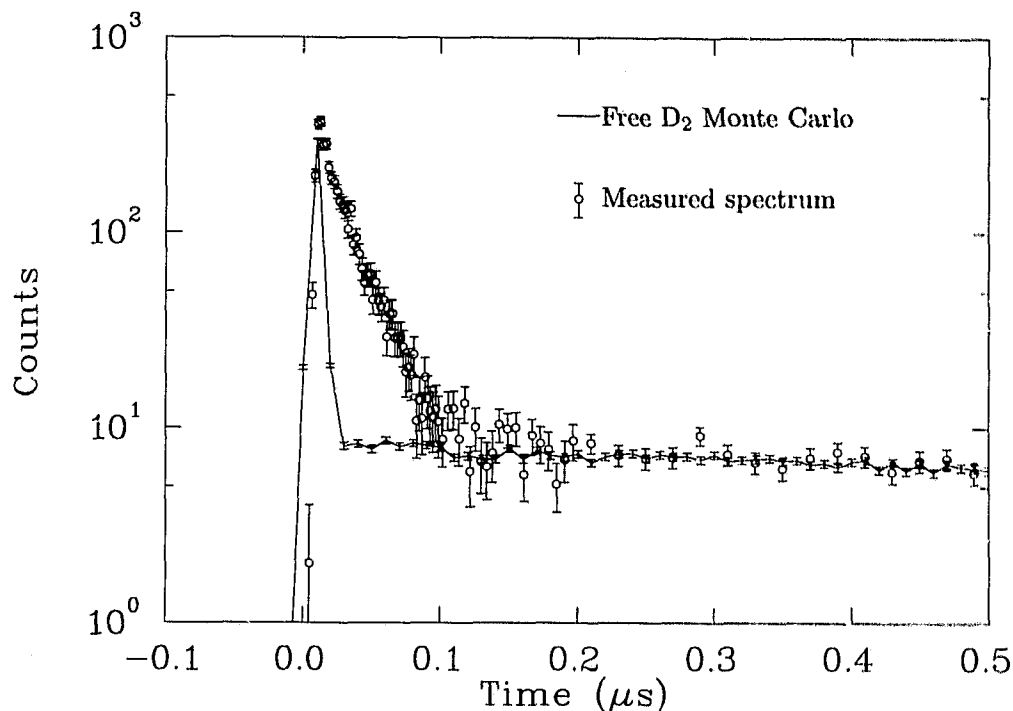


Figure 5.4.1: A plot of the neutron time distribution predicted by the Monte Carlo using the nuclear scattering cross sections. Also shown are the experimental data. The lack of agreement is clear.

well for muonic atoms of energy higher than a few tenths of an electron volt.

5.4.1 Monte Carlo of the Solid Deuterium

The Monte Carlo for solid deuterium was the first approach used to understand the solid state effects outlined in §2.1.4 (page 17). The first of the simulations was performed using the Markushin code which relied on the free nuclear cross sections that contain no corrections for molecular or solid state effects. A plot of the predicted neutron spectrum is shown in Fig. 5.4.1, along with the experimentally measured spectrum. The disagreement is clear.

Calculations for the scattering of μd atoms on D_2 contained in a solid have recently been completed [44]. These cross sections have been used in a Monte Carlo simulation in an attempt to accurately represent the energy loss processes and hence the energy distribution of the μd atoms in the solid as a function of time. The knowledge of the time dependence of the energy distribution then allows the resonant molecular formation and fusion to be modelled correctly.

The predicted effects of the collective nature of the solid state are shown in Fig. 5.4.2. The plot is of the *response function* of the solid. Given a process, in this case the scattering

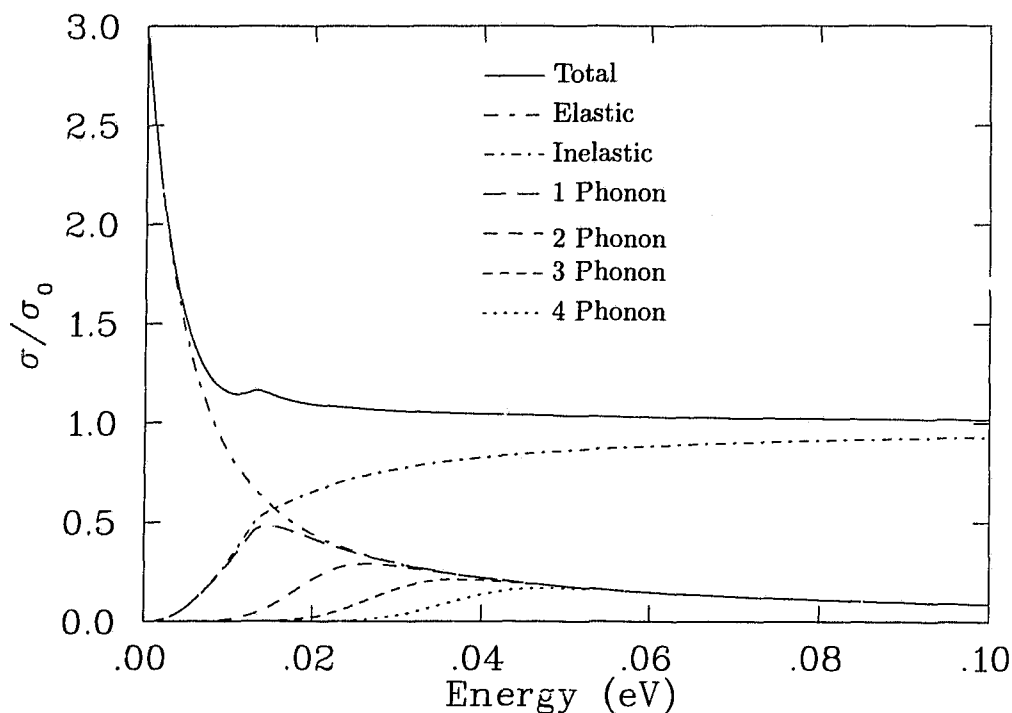


Figure 5.4.2: A plot of the response function for reactions in solid D_2 . The elastic, as well as the inelastic (phonon), response modes are shown normalized to an arbitrary free reaction cross section σ_0 . In the scattering reaction $\mu d + D_2$ the suppression of the inelastic, and hence thermalizing, response at low energies gives rise to the long times required to reach thermal equilibrium. The figure was provided by Adamczak [35].

of μd atoms by D_2 molecules bound in a lattice, the response function represents the correction factor which transforms the free molecular process into the process for molecules in the solid state. The individual curves represent the multiplicative factor which converts the free cross section into the solid state cross section with the appropriate number of phonons in the final state.

The reader will notice that each of the individual response functions (elastic, or 0 phonon, 1 phonon, and so on) tend to the same asymptotic curve as a function of energy. This behaviour is a consequence of the strong quantum nature of solid hydrogen and is expressed as an exponential decay called the Debye-Waller factor. Solid hydrogen is a quantum mechanical solid since the zero-point motion of the molecules in the crystal is large relative to the lattice spacing (15–18% of the average spacing which is ~ 0.5 nm). When interactions with the lattice occur on an extended spatial scale (many lattice sites) the position of the molecules is regular. This is what occurs for very low energy (long wavelength) processes. In the case of μd scattering, as a function of increasing energy, the effective wavelength of the scattering muonic atom spans less and less of the lattice and

hence becomes more sensitive to the variations of the molecules away from the ideal lattice sites¹¹. The Debye–Waller factor reflects this relative loss of periodicity by suppressing the effects due to the periodic structure.

Continuing with the example, the elastic scattering of a μd atom in the lattice is composed of the free molecular scattering cross section multiplied by the 0 phonon response function of the lattice (curve marked as *Elastic* in Fig. 5.4.2). At low energies (< 10 meV) the elastic scattering cross section exceeds the free scattering cross section by as much as a factor of three.

Inelastic scattering, the only energy loss mechanism available for the μd , proceeds via the excitation of phonons in the solid. From the graph it can be seen that as the energy of the μd decreases, the ability to create a phonon in the solid decreases and the muonic atom has fewer available energy loss mechanisms. This suppression of the energy loss mechanisms leads to the long time required for the muonic atoms to thermalize in the solid D_2 [44].

The Monte Carlo simulation required many input distributions during the simulation. Most important were the free molecular scattering reactions, $\mu d + D_2$, the energy dependence of the resonant molecular formation, and the initial energy distribution of the μd . The scattering cross sections for the $\mu d + D_2$ were taken from the work of Adamczak *et al.* and include such molecular effects as electron screening and rotational transitions in the D_2 ([63], and references therein). The molecular formation rates, correct for μd atoms incident on a D_2 gas at 3 K, were those of Faifman [64,25,26,36]. The initial energy distribution of the μd atoms was assumed to follow the Two-Maxwell model found from other experiments with exotic atoms [2,5]. The relative population of the thermal to epithermal distributions was a parameter varied in the simulation.

The simulations have led to a qualitative understanding of the observed rates. Although the initial energy loss of the μd is rapid ($\sim ns$), as the atom slows to the energy range of a few meV, the slowing down processes are suppressed. For $\mu d_{\frac{3}{2}}$, this slow thermalization allows time for the atom to participate in the lowest of the molecular formation resonances (cf. Fig. 2.1.2, page 13) and leads to an enhancement of the fusion rate.

Figure 5.4.3 shows both the experimental data and the simulation. The simulation has been fit with the same kinetics as the experimental data and good fits (as determined by the χ^2 value) to the two-exponential shape have been achieved. The values found for $\tilde{\lambda}_{\frac{3}{2}}$ have been in the range $2-3 \mu s^{-1}$, but this number scales directly with the initial ratio of epithermal to thermal μd atoms.

The slow thermalization implies a reinterpretation of the parameters in the two node approximation. The $\tilde{\lambda}_{\frac{3}{2}}$ rate is a measure of the time the μd atom spends at the resonant energy values convoluted with the size of the resonant formation at that energy. The $\tilde{\lambda}_{\frac{3}{2}\frac{1}{2}}$

¹¹The DeBroglie wavelength for a particle is $\lambda = \frac{2\pi\hbar}{p}$. For a μd at energy E (in eV) then $\lambda = \frac{0.02}{\sqrt{E}}$ nm. At 10 meV, $\lambda = 0.2$ nm, which is similar to the zero point oscillation size.

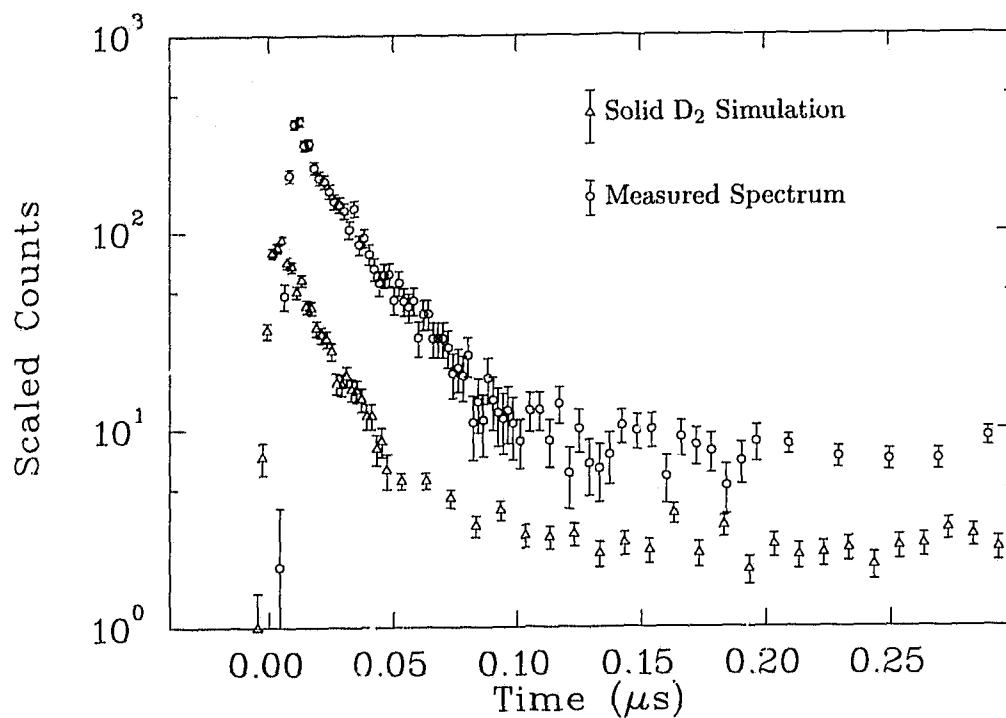


Figure 5.4.3: A comparison of the measured and simulated neutron fusion spectra in D_2 for the Monte Carlo of Adamczak. The simulation makes correct use of the slow thermalization predicted from the solid state effects to permit a significant amount of resonant formation. The scaling has been arbitrarily chosen so that the similarity between the data and the simulation for both resonant and nonresonant lifetimes can be seen.

value reflects all processes removing the epithermal μd atoms from the resonant energy region. This rate is composed of the spin flip to the lower hyperfine state (either by resonant formation and back decay, or by the direct spin exchange scattering) and thermalization by inelastic scattering.

The quantitative interpretation of these results is not clear at the moment. There is no consideration of geometry in the Monte Carlo simulation so effects such as μd loss due to the finite size of the solid layer is not taken into account. In addition, the molecular formation rates used in the simulation were calculated for free D_2 molecules so there is no correction for solid state effects in the formation rate. The solid state will likely have an effect on this rate since the availability of phonon modes in the final state changes the resonance energy requirements. Men'shikov *et al.* have suggested that this effect may be sufficiently strong to allow subthreshold molecular formation to play a role resulting in resonant formation for completely thermalized $\mu d_{\frac{3}{2}}$ atoms incident on D_2 molecules in the $J = 1$ rotational state [65].

5.4.2 Monte Carlo of the Emission Process

The Monte Carlo of Markushin was used to aid in the understanding of the emission data. Monte Carlo simulations of various surface layer thicknesses were done, and the resulting spectra of the fusion time distributions fit with the same fitting function as used for the experimental data.

The input values for the rates $\lambda_{pd}(= 17.3 \times 10^3 \mu\text{s}^{-1})$, and $\lambda_{p\mu p}(= 3.21 \mu\text{s}^{-1})$, were assumed to be energy independent and fixed at the values previously measured in solid hydrogen [66, 49]. The $\lambda_{p\mu d}$ rate was also assumed to be constant in energy and was set at the value $5.6 \mu\text{s}^{-1}$ [26]. The scattering cross sections, which were for muonic atoms on hydrogen nuclei only, were taken from Bracci *et al.* [11] and Chiccoli *et al.* [12]. All of these scattering cross sections were calculated for muonic atoms incident on 300 K gas, which should work well when the energy of the μd atom is high (> 30 meV) but for lower energy μd atoms the averaging of the 300 K thermal motion of the target D_2 molecules will be different than the thermal averaging appropriate for 3 K targets. The $d\mu d$ molecular formation rates, correct for μd atoms incident on a D_2 gas at 3 K, were taken from the work of Faifman [64, 25, 26, 36].

One important feature of the Monte Carlo is the ability to set the minimum energy which the muonic atoms can reach. Once the muonic atom has reached this value via energy loss in scattering reactions, subsequent scatterings cause no more energy loss. It is, in effect, a hard limit on the low energy thermalization of the muonic atoms. Two low energy cutoff values were investigated, 0.1 meV (≈ 1 K) and 1.0 meV (≈ 11 K). Note that this value is not the mean energy of a Maxwellian distribution, but is a δ function distribution.

The simulation was used in an effort to reproduce the relative yields of the different surface layer thicknesses. Figure 5.4.4 shows a plot of the measured yields, scaled by a constant chosen to make the simulation of the 50 Tl surface layer, for the case of 1.0 meV minimum energy, exactly match the 50 Tl yield data ($320 \mu\text{g} \cdot \text{cm}^{-2}$). The simulation which allowed the muonic atoms to thermalize to 0.1 meV was scaled by the same factor¹² to allow meaningful comparisons between the two simulations. Both simulations give the yield of protons resulting from emitted μd only, there is no contribution to the yield from direct stops. The agreement with the data for the 1.0 meV energy limit seems to indicate that the simulation is not too inaccurate when using the nuclear cross sections (unlike the case for the pure solid deuterium), but that the choice of the low energy limit is important. However, the simulation of the time spectra (see below) indicates that there are other problems with the simulation, hence further quantitative analysis was not done.

The time distributions generated by the Monte Carlo with the 1.0 meV low energy

¹²The factor was 0.0044. The solid angle of the silicon detector was ~ 0.02 , and the stopping fraction of GMU muons in the emission layer is ~ 0.2 , so the choice of scaling factor is consistent with that.

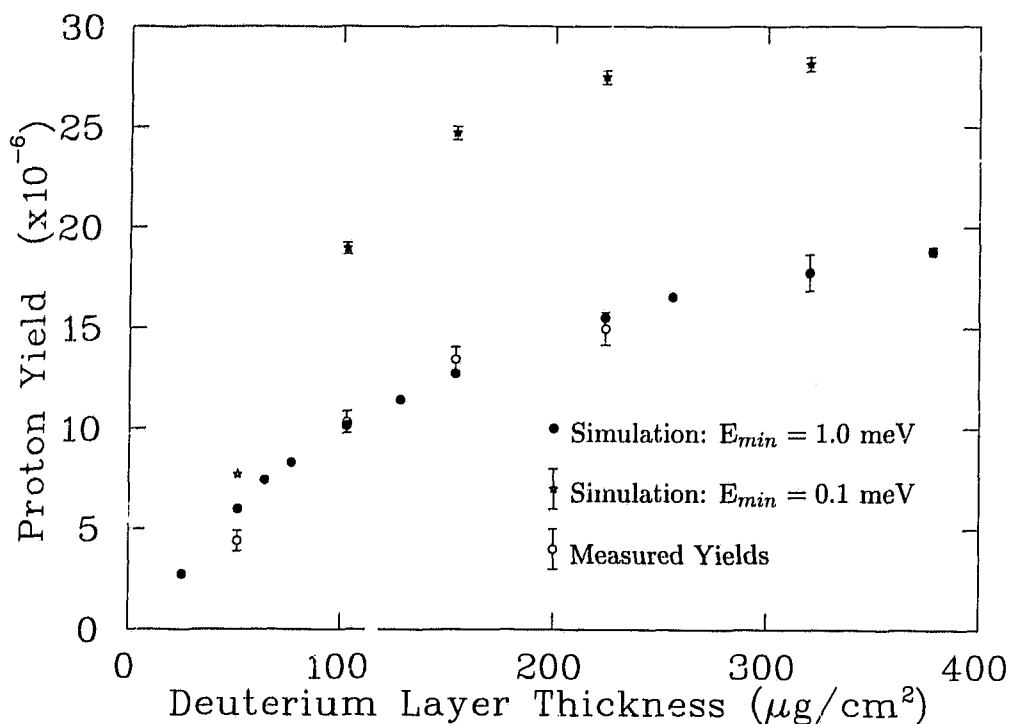


Figure 5.4.4: The Monte Carlo simulation of the proton yield as a function of the surface layer thickness. The simulations have been normalized to make the 50 Tl ($320 \mu\text{g} \cdot \text{cm}^{-2}$) point match exactly between the measurement and the simulation with the 1.0 meV minimum energy. Both simulations were scaled by the same factor. Neither simulation includes any contribution from muons stopping directly in the D_2 layer.

limit are shown in Fig. 5.4.5. The μp disappearance rate was the same for all of the surface layer thicknesses. A fit of an exponential decay function to the μp disappearance yielded a rate of $24.963(10) \mu\text{s}^{-1}$. Based on the input parameters, the expected disappearance rate was $24.9724 \mu\text{s}^{-1}$ [cf. R_1 in Eq. (2.20), page 25], in good agreement.

The production time of the protons, however, contains all of the effects of emission and molecular formation, including energy loss processes. Figure 5.4.5 shows the time of proton production as predicted by the simulation. The difference between the successive layer thicknesses is interesting, and is a function of the low energy limit chosen in the Monte Carlo. The appearance of fusions at long times, $t > 0.3 \mu\text{s}$, for layers thicker than 16 Tl is an effect not seen in the data, Fig. 5.3.7, page 90. Because of the long lifetime associated with the late time fusions, they are clearly due to nonresonant molecular formation from μd atoms thermalized in the thin deuterium layer (it is also possible in the simulation to know the arrival time of the μd in the surface layer, and μd atoms are not arriving late). Here again, the thermalization of the μd in the simulation is too rapid due to the inadequate cross sections.

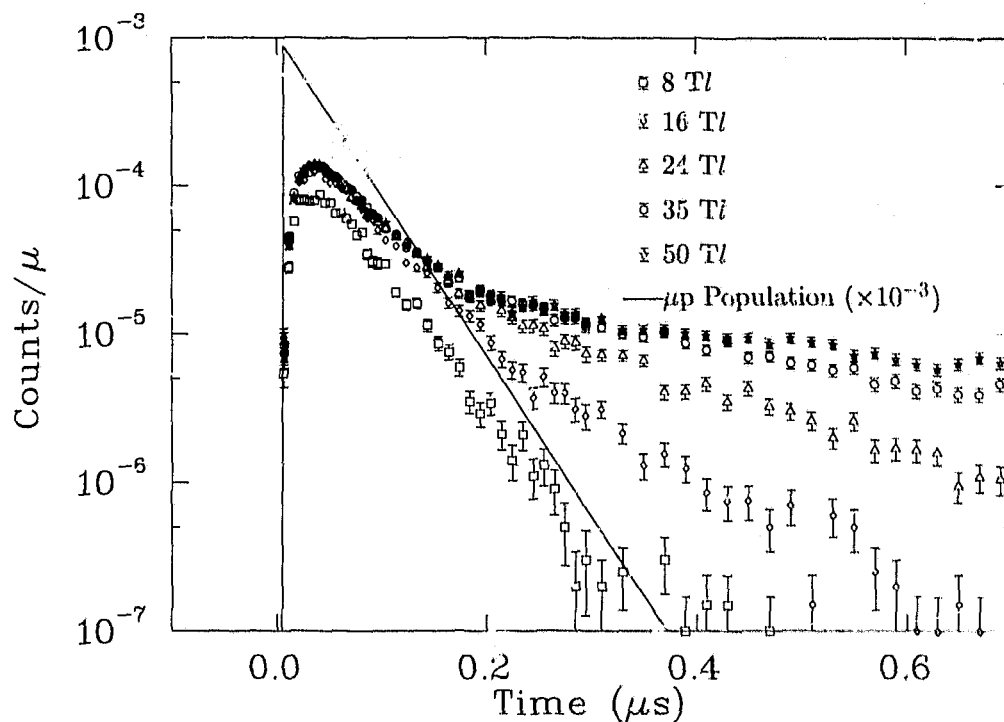


Figure 5.4.5: Time distributions of the protons produced by emitted muonic deuterium as predicted by the Monte Carlo. All of the simulations pictured above were run with the 1.0 meV minimum energy limit.

The simulations which allowed the μd atoms to lose energy until the 0.1 meV limit showed a much stronger contribution from late time fusions. The simulation of the 16 Tl layer with the 0.1 meV energy limit contained more counts from the long time fusions than the 50 Tl simulation pictured above. This is reflected in the plot of the simulated yields shown in Fig. 5.4.4, where the Monte Carlo with the lower energy limit strongly dominates over the simulation with the 1.0 meV minimum energy. Although both 0.1 and 1.0 meV are energies below the lowest of the molecular formation resonances, the extremely thin nature of the layer allows the 1.0 meV μd atoms to diffuse out of the layer more readily than the 0.1 meV atoms due to the difference in velocities, and muonic atoms which escape cannot contribute to the proton yield. This escape process is confirmed by the Monte Carlo.

Simulations for an 8 Tl and a 40 Tl surface layer, made with the 1.0 meV minimum energy, were fit with the emission model dynamics to see what the model revealed.

The simulations were fit twice, once with a simple exponential decay in order to find the decay rate in the region $0.05 \mu s < t < 0.3 \mu s$, and a second time with the full growth and decay model. Since the 40 Tl simulation contained the long lifetime fusion contribution not seen in the real data, its contribution to the spectrum was treated as a background since only the epithermal interactions were of interest. The fit time interval was short

Growth and Decay model							
Layer Tl	Amplitude $K \times 10^{-3}/\mu$	<i>acorr</i>	R_1 (μs^{-1})	R_2 (μs^{-1})	δt ns	<i>bgs</i> ($\times 10^{-7}$)	χ^2/dof (cl)
8	87(20)	1.091(21)	25.7(1.4)	46(4)	0	2.7(7)	81/65 (9%)
8	74(13)	1.040(11)	25.3(1.2)	48(4)	3	1.9(7)	76/65 (16%)
8	59(8)	0.987(9)	24.7(1.0)	53(4)	6	1.8(7)	71/65 (28%)
8	55(8)	0.931(14)	24.3(1.1)	54(5)	8	1.8(7)	83/65 (6%)
40	79(13)	1.198(43)	21.2(1.4)	55(5)	0	109(5)	80/75 (32%)
40	60(6)	1.112(19)	19.9(1.0)	69(6)	5	109(5)	69/75 (65%)
40	52(5)	0.842(35)	19.3(1.1)	71(11)	10	103(5)	82/75 (27%)
40	58(6)	1.112(20)	19.7(1.0)	71(8)	5.3(6)	107(5)	70/74 (62%)

Single Simple Exponential				
Layer Tl	Fit Range μs	Rate (μs^{-1})	Background ($\times 10^{-4}$)	χ^2/dof (cl)
8	0.06-0.3	22.48(75)	-0.3(6.0)	51/42 (14%)
8	0.04-0.3	21.07(58)	0.1(4.6)	65/46 (3%)
8	0.1-0.3	23.6(1.3)	0.4(5.2)	42/35 (18%)
40	0.06-0.3	18.1(1.2)	388(31)	42/45 (60%)
40	0.04-0.3	19.05(87)	388(24)	43/49 (71%)
40	0.1-0.3	22.1(2.4)	292(6.7)	32/38 (74%)
40	0.03-0.3	18.52(73)	396(24)	45/51 (72%)

Table XVIII: A summary of the attempts to fit the toy model to the Monte Carlo simulations.

enough that a constant was sufficient to represent it (use of an exponential was also tried, and the fits were not significantly different). The summary of the fit of the model to the simulation is given in Table XVIII.

According to this Monte Carlo, the μp disappearance rate is very closely modelled by the R_1 lifetime found from the proton time spectrum by the simple emission model. This predicted agreement is in contradiction with the previous work in neon, where the time structure of the x rays from transfer was found to differ from a pure exponential, due to the interactions of the μd atom in the emission layer and the subsequent emission time distribution. The Monte Carlo simulation used in that analysis included corrections to the nuclear cross section due to molecular effects [49, 67].

The values chosen for the μd energy limits were picked to investigate the effect that the limit has on the simulated spectra. Although choosing a higher value for the limit has the effect of suppressing the number of fusions occurring at long times allowing better agreement with the data, such a choice is arbitrary, and does not correctly model the physics of the situation, which is an energy distribution of the μd atoms (not a δ -function). For some choice of the low energy limit, near 3-4 meV, the molecular formation rate is resonant, and all of the emitted μd atoms will fuse rapidly. Clearly, more Monte Carlo work is required, but for it to be truly correct, the cross sections for the processes such as $\mu\text{d} + \text{D}_2 \rightarrow \mu\text{d} + \text{D}_2$ for D_2 held in a solid lattice of $^1\text{H}_2$ need to be used.

Chapter 6

Discussion and Conclusions

Like many experiments, the data and analysis presented herein have posed as many new questions as have been answered. The pertinent results will be recapitulated here, with an emphasis on the contribution made to the μ CF community, and on the proposals for work which can help clarify the presented results.

6.1 Results for Solid Deuterium

The results derived from our experiment show that the processes governing the fusion in the solid state are not completely understood in a quantitative sense, but that a qualitative consistency has been achieved with the only theory to date to explicitly examine fusion in the solid state.

Kinetics Parameters

Under the assumptions inherent in the two-node approximation, the values found for the kinetics parameters presented in Table IX (reiterated here in Table XIX) represent the first examination of the muon catalyzed fusion process in solid D_2 .

Parameter	Value
$\lambda_{\frac{3}{2}\frac{1}{2}}$	34.2(8) _{stat.} (1) _{sys.} μS^{-1}
$\lambda_{\frac{3}{2}}$	2.71(7) _{stat.} (32) _{sys.} μS^{-1}
$\phi_z \lambda_z$	0.320(10) _{stat.} (1) _{sys.} μS^{-1}
P_s	0.47(8) _{stat.} (6) _{sys.}
β_s	0.487(15) _{stat.} (11) _{sys.}
β_p	0.563(14) _{stat.} (11) _{sys.}

Table XIX: The kinetics values resulting from the simultaneous fits to both neutron and proton data from solid deuterium. The value of $\tilde{\lambda}_{\frac{1}{2}}$ ($= 0.044 \mu\text{S}^{-1}$) was fixed for all of the fits.

Parameter	Value
$\tilde{\lambda}_{\frac{1}{2}}$	0.052(8) _{stat.} (3) _{sys.} μS^{-1}
$\tilde{\lambda}_{\frac{3}{2}\frac{1}{2}}$	34.0(8) _{stat.} (1) _{sys.} μS^{-1}
$\lambda_{\frac{3}{2}}$	3.21(51) _{stat.} (16) _{sys.} μS^{-1}
$\phi_z \lambda_z$	0.320(10) _{stat.} (1) _{sys.} μS^{-1}

Table XX: The measurement of $\tilde{\lambda}_{\frac{1}{2}}$ from the simultaneous fits of neutron and proton spectra.

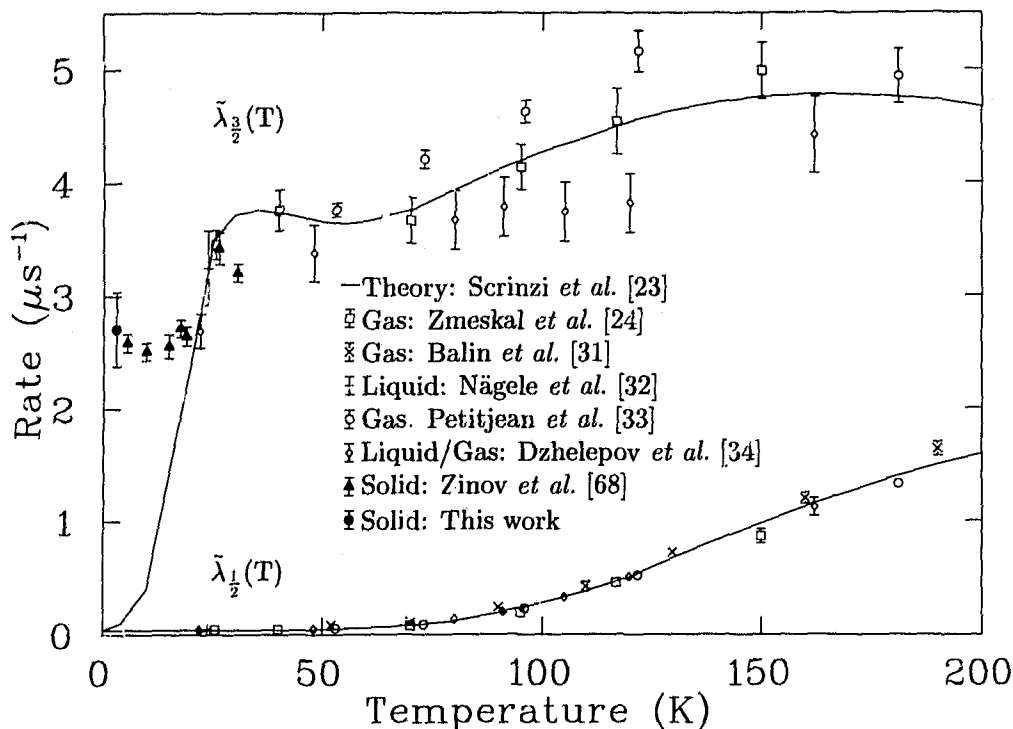


Figure 6.1.1: A graph of molecular formation rates as measured in solid, liquid and gas, and calculations for liquid and gas. The points of Zinov *et al.* do not include the systematic uncertainty associated with the $\tilde{\lambda}_{1/2}$ value.

The qualitatively successful Monte Carlo simulation of fusion in solid D_2 is a clear indication that the effects of the solid state on the fusion are important. What is perhaps most surprising is that the two-node approximation works at all in this situation.

The kinetics model is simple in the sense that time-independent rates are used, an assumption which can be challenged when the thermalization of the μd is slow. The indication from the solid D_2 Monte Carlo is that the thermalization is rapid until the μd reach relatively low energies (<10 meV) [44]. Since the $\mu\text{d}_{1/2}$ can only participate in nonresonant molecular formation when at energies below 10 meV (cf. Fig. 2.2.2, page 23), the assumption of the time-independent nonresonant rate is valid. The assumption is also consistent with the value measured for $\tilde{\lambda}_{1/2} [= 0.052(8)_{\text{stat.}}(3)_{\text{sys.}} \mu\text{s}^{-1}]$ which is in agreement with the nonresonant molecular formation rates measured in other experiments [33]. For the $\mu\text{d}_{3/2}$, the slow thermalization at the lowest energies allows the muonic atom to participate in the lowest of the molecular formation resonances. Even so, the spin deexcitation processes and the thermalization remove the μd from the resonant energy region at least ten times faster than the effective formation rate. Under such conditions, the sensitivity to the shape of the resonance is suppressed and a constant rate can model the reaction.

Indeed, the value of the $\tilde{\lambda}_{3/2}$ rate contains the spin flip from scattering, a contribution

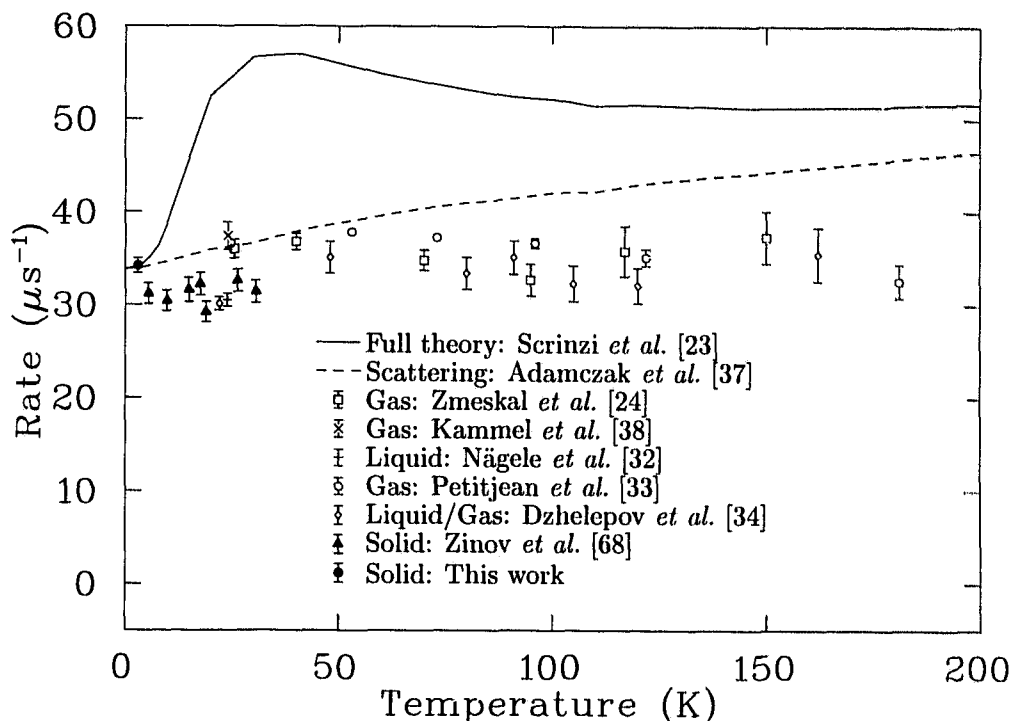


Figure 6.1.2: The comparison of $\tilde{\lambda}_{\frac{3}{2}\frac{1}{2}}$ to previously measured values.

from back decay, and the effective rate of energy loss for the $\mu d_{\frac{3}{2}}$ which are in the energy window of the lowest resonance. Since the measured value for the effective spin flip contains all of these effects, while at the same time is consistent with the calculation of spin flip by scattering alone, the measurement is an implication that the calculated rate is too large.

Emission of the μd from the layer is a loss mechanism that is not explicitly taken into account in the analysis, however the process would mimic the $\phi_z \lambda_z$ loss mechanism. The value found for $\phi_z \lambda_z$, coupled with the value for the transfer to nitrogen, $\lambda_z \approx 10^5 \mu s^{-1}$, implies a nitrogen contamination of about 1.5 ppm, a value which was independently measured for the thick deuterium target [69]. If the value were to represent only μd escape from the layer, then roughly one third of all the μd atoms are emitted from the layer. Given the current understanding of the scattering cross sections, this process is unlikely to give such a strong effect. A Monte Carlo which includes the cross sections corrected for solid state effects as well as an accurate modelling of the finite geometry of the targets is required before the quantitative reinterpretation of the $\tilde{\lambda}_{\frac{3}{2}}$ and $\tilde{\lambda}_{\frac{3}{2}\frac{1}{2}}$ rates in terms of thermalization will be possible.

An examination of Eq. (A.2) shows that an increase in $\tilde{\lambda}_f$, the deexcitation rate leading to fusion, for the resonantly formed $[(d\mu d)_{J\nu}^s, dee]$ will increase the effective formation rate by more successfully competing with the $\Gamma_{SF'}$ deexcitation mode (back decay). If there exists a sufficiently strong coupling of the rovibrational modes of the resonant six body

complex to the phonons in the solid, then there may be sufficient augmentation of the deexcitation rate to allow this effect. The molecular formation rate in solid has not yet been rigorously examined for solid state effects.

Zinov *et al.* [68] have presented values for μCF in solid deuterium over a range of temperatures, assuming a similar kinetics function. That experiment and this one are consistent, however the disagreement with theory indicates that comprehensive calculations for the molecular formation rate including solid state effects must be made. If the even-odd populations of D_2 angular momenta are as important as suggested in Ref. [65] then further experiments will certainly be required.

The next round of experiments will have to examine the thermalization process, as well as the possible para-ortho effects. The one predicted effect on the molecular formation for thermalized $\mu d_{\frac{3}{2}}$ only occurs for para- D_2 (i.e., $J = 1$) [65]. Using solid ortho- D_2 would help to verify or discount that effect.

In a solid hydrogen layer (i.e., where the density is fixed) the molecular formation rate is concentration dependent, $\propto c_d \phi N_o$, but the thermalization rate is not, since the scattering and energy loss processes for both $\mu d + D_2$ and $\mu d + {}^1H_2$ are similar for low energy μd in solid ($\propto (c_d + c_p) \phi N_o$, where $c_d + c_p = 1$). An experiment in a solid mixture of $D_2 + {}^1H_2$ with several values of the deuterium concentration will not yield the same reduced formation rate $\tilde{\lambda}_{\frac{3}{2}}$ if the slow thermalization process is responsible for the rate observed in pure D_2 . The experiment in a $D_2 + {}^1H_2$ mixture will be more difficult to analyze, since the μp to μd transfer and subsequent creation of an epithermal μd will change the initial intensity of the epithermal μd atoms, the effect believed to be responsible for the elevated $\tilde{\lambda}_{\frac{3}{2}}$ to begin with. Again, accurate simulations of the experiments will be necessary during the analysis.

Branching Ratios

There are three parameters that constitute the effective branching ratio β_F : β_s , β_p , and P_s , [cf. Eq. (A.5), page 113]. Table XIX contains the measured values of each of these parameters once the standard values are assumed for the other two.

The measurement of $\beta_p = 0.563(14)_{stat.}(11)_{sys.}$ is consistent with the previously measured values, but has an error two to three time larger than the previous measurements. The measurement of $\beta_s = 0.487(15)_{stat.}(11)_{sys.}$ is consistent with the prediction of Hale *et al.*, whose value was 0.470 [43].

Since the β_s and β_p values are consistent with the other measurements, it is best to assign them their standard values and from there derive a measurement of P_s for the first time. The theory of Faifman [26], predicts a value of 0.560 at very low energy. Our measurement at the value $0.47(8)_{stat.}(6)_{sys.}$ is lower than the prediction but the disagreement is not strong given the uncertainty. It should also be noted that the P_s value is dependent on the energy at which molecular formation occurs, so for μd atoms in the process of ther-

malizing a constant P_s does not accurately represent the true physics processes. Again, a comprehensive Monte Carlo study of the physics will be needed in order to compare the energy averaged $P_s(E)$ with the measured constant P_s .

6.2 Results from the Emission Measurements

Based on the analysis of the fusion proton energy spectra and the agreement of the relative yield predicted by the Monte Carlo (cf. Fig. 5.4.4, page 97), it appears that the calculated cross sections for the μd interactions are not grossly incorrect for the higher energy μd atoms. This conclusion must be tempered by the consideration that the simulated yield contains a component from fusions at long times (cf. Fig. 5.4.5, page 98) and none from direct stops. The experimental data, on the other hand, (cf. Fig. 5.3.7, page 90) do not indicate any contribution to the yield from fusions at long times, but will contain a contribution from direct stops. From the fit to the yield data as a function of layer thickness (cf. Table XII, page 82), the indication is that the ability to fit the data decreases as the contribution from direct stop fusions is increased (A_2 parameter). The size of the direct stop contribution found in the fit to the time spectrum is relatively small (cf. Gaussian Amplitude in Table XVII, page 89), which indicates that the direct stop contribution is not particularly important. Thus the agreement between data and simulation may be accidental since the data show no evidence of a large contribution to the yield from either direct stop or long time fusions, but the simulation contains a significant contribution from fusions at long times with a magnitude strongly dependent on the artificially chosen low energy limit in the Monte Carlo.

The measured value of R_1 , the decay rate defined in Eq. (2.20) (cf. Table XVII, page 89), can be used to compare to the measurements of the λ_{pd} and $\lambda_{p\mu p}$ rates found under the similar conditions for emission of the μd but with the D_2 surface layer replaced with a layer of neon.

From the previous work with neon, the decay rate of the muonic neon x rays measured for a $c_d = 0.1\%$ target (i.e., the same as for the measurement presented here) was $17.9(2.8) \mu s^{-1}$ which is remarkably close to the rates measured here in the time spectrum of the fusion protons [70]. Since the emission processes for the μd are the same for the two experiments, and the transfer reactions and subsequent x rays will be very rapidly generated for the μd atoms emitted into the neon layer, the similar lifetime in the proton spectrum indicates that the molecular formation and fusion in the D_2 surface layer is rapid. This confirms the second assumption necessary to the success of the toy model.

The Markushin Monte Carlo of the emission indicates that the lifetime measured in the proton time spectrum should be equal to the μp disappearance rate when the fusion in the surface layer is fast. This is in contradiction with the Monte Carlo used for the analysis of the neon data which indicates that the μp disappearance rate is somewhat

faster than the signal rate, and in fact, that the detected signals are not truly represented by an exponential decay [49]. This specialized Monte Carlo used cross sections which were corrected for the differences between the nuclear and molecular scattering processes [67]. The low energy differences in the cross sections have a large effect on the emission time, leading to a situation better modeled as diffusion of the μd to the surface layer rather than as an emission rate.

From Eq. (2.20) and using the values for $\lambda_{pd}(= 1.73 \times 10^4 \mu s^{-1})$ and the molecular formation rate $\lambda_{p\mu p}(= 3.24 \mu s^{-1})$, the R_1 rate is $\sim 26 \mu s^{-1}$, fully 50% larger than the measured R_1 rate (cf. Table XVII). This is an indication that the modeling of the emission process as a rate is inadequate. Since only one c_d was measured in this experiment, it is impossible to give a measurement of the $\lambda_{p\mu p}$ and λ_{pd} rates.

The consistency between the measured rates for the two very different signals indicating μd emission is good. The interpretation of the rates, especially here for the proton signals where only one c_d was measured, in terms of the μp disappearance rates is difficult and will again rely on a Monte Carlo which has cross sections which are correct for the low energy μd in solid hydrogen.

For the R_2 rate, and the rest of the interpretation of the parameters of the simple emission model, the accuracy is limited by the background and by the detector resolution. The somewhat large time resolution of ~ 24 ns FWHM means that reactions happening faster than about $40 \mu s^{-1}$ cannot be measured with good accuracy. For the *acorr* value, the correlations are very strong with the R_2 value so again the predictive power of the model was consumed by the poor timing resolution.

The proof in principle for the physics accessible by the emission measurements is clear. Given a better timing resolution, and the correct input for the Monte Carlo necessary for the completion of the analysis, the ability to access the reaction rates of muonic atoms in the [0.1–10] eV range is very promising.

6.3 Improvements and Future Directions

The solid D_2 targets were contaminated by nitrogen and thus sensitivity to a kinetics parameter was lost during the fits to the data. This contamination resulted from the difficulty of doing experiments which are strongly sensitive to nitrogen while at the bottom of a ocean of nitrogen gas and especially with equipment which leaked. Much of the problem with leaks resulted from the design and construction of the gas handling system, which had long sections of small diameter piping often under stress at the weld joints. A new tritium-compatible gas handling system has been constructed which has helped to alleviate the problem in the experiments done since the initial work presented here.

The effect of thermalization may possibly be examined by looking for the rates in $^1H_2/D_2$ mixtures where the low energy thermalization of the μd atoms is the same as in

pure D_2 , but the concentration c_d of D_2 is less than 1. If the resonant fusion rate falls off faster than a linear function of c_d , then there is evidence of slow thermalization as the source of the resonant fusion peak. The examination of the difference between ortho and para deuterium is also interesting.

A fully working Monte Carlo is necessary. It will have to include the ability to model the effects of the finite target geometry and use the cross sections corrected for molecular and collective effects (some of which are not yet calculated). It can be misleading to use the free molecule cross sections and assume that the results of the simulation apply when the evidence of solid state effects is so large.

The emission measurements were the first of their kind, and have subsequently been repeated and also used as a method to produce slow μ^- (muons with energy less than 10 keV) [22]. Until such time as a complete Monte Carlo becomes available to assist in the analysis, the results presented here can, at best, be taken as a qualitative indication that the calculated cross sections are accurate. More extensive experimentation, with more and thicker D_2 surface layers, and with different c_d concentrations, will be necessary for quantitative measurements to emerge. Some of the problems associated with the poor timing resolution of the silicon detectors has been overcome by the use of better cabling inside the vacuum system.

Tritium compatibility was built into the system to allow experiments with that radioactive isotope, and the emission of μt atoms from a tritium-doped 3H_2 layer has already been verified. The resulting energetic μt atoms were used for a time-of-flight experiment which has collected information on the molecular formation resonances in the dt system [71]. All in all, the solid layer target system has many applications in the experimentation with energetic μd and μt atoms.

Bibliography

- [1] J. S. Cohen, *Phys. Rev. A* **27**, 167 (1983).
- [2] E. C. Aschenauer *et al.*, *Phys. Rev. A* **51**, 1965 (1995).
- [3] V. E. Markushin, *Phys. Rev. A* **50**, 1137 (1994).
- [4] J. B. Kraiman *et al.*, *Phys. Rev. Lett.* **63**, 1942 (1989).
- [5] D. J. Abbott *et al.*, Diffusion of muonic deuterium and hydrogen atoms, in submission, *Phys. Rev. A.* (1995).
- [6] F. Mulhauser and H. Schneuwly, *J. Phys. B* **26**, 4307 (1993).
- [7] S. Jones *et al.*, *Phys. Rev. Lett.* **56**, 588 (1986).
- [8] W. Czaplinski *et al.*, *Phys. Rev. A* **50**, 518 (1994).
- [9] A. Adamczak *et al.*, *Muon Catal. Fusion* **7**, 309 (1992).
- [10] A. Adamczak and V. S. Melezhik, *Muon Catal. Fusion* **4**, 303 (1989).
- [11] L. Bracci *et al.*, *Muon Catal. Fusion* **4**, 247 (1989).
- [12] C. Chiccoli *et al.*, *Muon Catal. Fusion* **7**, 87 (1992).
- [13] J. S. Cohen and M. C. Struensee, *Phys. Rev. A* **43**, 3460 (1991).
- [14] J. S. Cohen, *Phys. Rev. A* **43**, 4668 (1991).
- [15] J. S. Cohen, *Phys. Rev. A* **44**, 2836 (1991).
- [16] L. W. Alvarez *et al.*, *Phys. Rev.* **105**, 1127 (1957).
- [17] E. A. Vesman, *Pis'ma Zh. Eksp. Teor. Fiz.* **5**, 113 (1967), [*JETP Lett.*, **5**, 91-93 (1967)].
- [18] W. H. Breunlich, P. Kammel, J. S. Cohen, and M. Leon, *Ann. Rev. Nucl. Part. Sci.* **39**, 311 (1989).

- [19] V. I. Korobov, I. V. Puzynin, and S. I. Vinitsky, *Muon Catal. Fusion* **7**, 63 (1992).
- [20] L. N. Bogdanova, ITEP Preprint 95-91 (1991), [Talk at the 13th European conference on Few-Body problems in physics, Elba, September 9-14, 1991].
- [21] M. C. Fujiwara *et al.*, Measuring sticking and stripping in muon catalyzed *dt* fusion with multilayer thin films, Proceedings of μ CF-95, Dubna, Russia, 1995.
- [22] P. Strasser, Ph.D. thesis, University of Tokyo, 1994, unpublished.
- [23] A. Scrinzi *et al.*, *Phys. Rev. A* **47**, 4691 (1993).
- [24] J. Zmeskal *et al.*, *Phys. Rev. A* **42**, 1165 (1990).
- [25] M. P. Faifman, L. I. Menshikov, and T. A. Strizh, *Muon Catal. Fusion* **4**, 1 (1989).
- [26] M. P. Faifman, *Muon Catal. Fusion* **4**, 341 (1989).
- [27] A. Scrinzi, *Muon Catal. Fusion* **5/6**, 179 (1990/91).
- [28] M. P. Faifman *et al.*, Quadrupole Corrections to Matrix Elements of Transitions in Resonant Reactions of mesic molecule Formation, Proceedings of μ CF-95, Dubna, Russia, 1995.
- [29] L. I. Ponomarev, *Contemp. Phys.* **31**, 219 (1990).
- [30] W. Kolos and L. Wolniewicz, *J. Chem. Phys.* **49**, 404 (1968).
- [31] D. V. Balin *et al.*, *Phys. Lett. B* **141**, 173 (1984).
- [32] N. Nägele *et al.*, *Nucl. Phys. A* **493**, 397 (1989).
- [33] C. Petitjean *et al.*, New precision measurements of *d μ d* fusion in *D₂* gas, Proceedings of μ CF-95, Dubna, Russia, 1995.
- [34] V. P. Dzhelepov *et al.*, *Zh. Eksp. Teor. Fiz.* **101**, 1105 (1992), [*Sov. Phys. JETP*, **74**(4), 589-595 (1992)].
- [35] A. Adamczak, (private communication).
- [36] M. P. Faifman, (private communication).
- [37] A. Adamczak, *Muon Catal. Fusion* **4**, 31 (1989).
- [38] P. Kammel *et al.*, *Phys. Lett. B* **112**, 319 (1982).
- [39] M. Leon, *Hyp. Int.* **82**, 151 (1993).
- [40] A. Adamczak and V. S. Melezhik, *Muon Catal. Fusion* **5/6**, 65 (1990/91).

- [41] B. P. Ad'yasevich *et al.*, *Yad. Fiz.* **33**, 1167 (1981), [*Sov. J. Nucl. Phys.*, **33**, 619–621 (1981)].
- [42] D. V. Balin *et al.*, *Pis'ma Zh. Eksp. Teor. Fiz.* **40**, 318 (1984), [*JETP Lett.*, **40**, 1112–1114 (1984)].
- [43] G. M. Hale, *Muon Catal. Fusion* **5/6**, 227 (1990/91).
- [44] A. Adamczak, *Thermalization of muonic hydrogen in hydrogen targets*, Proceedings of μ CF-95, Dubna, Russia, 1995.
- [45] S. S. Geistein *et al.*, *Zh. Eksp. Teor. Fiz.* **78**, 2099 (1980), [*Sov. Phys. JETP*, **51**(6), 1053–1058 (1980)].
- [46] B. M. Forster *et al.*, *Hyp. Int.* **65**, 1007 (1990).
- [47] G. M. Marshall *et al.*, *Z. Phys. C* **56**, 44 (1992).
- [48] G. M. Marshall *et al.*, in *Muonic Atoms and Molecules*, edited by L. A. Schaller and C. Petitjean (Birkhäuser Verlag, CH-4010, Basel, 1993), pp. 251–260, [Proceedings of the Centro Stefano Franscini, Ascona].
- [49] R. Jacot-Guillarmod *et al.*, *Muon molecular formation and transfer rate in solid hydrogen-deuterium mixtures*, Proceedings of μ CF-95, Dubna, Russia, 1995.
- [50] A. Pifer, T. Bowen, and K. R. Kendall, *Nucl. Instrum. Methods* **135**, 39 (1976).
- [51] M. Hendry, University of Victoria, Physics 429 Directed study (unpublished).
- [52] P. E. Knowles *et al.*, *A windowless frozen hydrogen target system*, accepted for publication in *Nucl. Instrum. Methods*, June 30, 1995.
- [53] M. C. Fujiwara, Master's thesis, University of British Columbia, 1994, unpublished.
- [54] V. V. Verbinski *et al.*, *Nucl. Instrum. Methods* **65**, 8 (1968).
- [55] M. Lifshitz and P. Singer, *Phys. Rev. C* **22**, 2135 (1980).
- [56] L. Lyons, *Statistics for Nuclear and Particle Physicists* (Cambridge University Press, Cambridge, 1986).
- [57] The American Physical Society, *Phys. Rev. D* **50**, (1994).
- [58] C. Petitjean *et al.*, *Muon Catal. Fusion* **2**, 37 (1988).
- [59] P. E. Knowles *et al.*, *Hyp. Int.* **82**, 521 (1993).
- [60] V. E. Markushin, PSI Preprint 94-38 (1994).

- [61] V. E. Markushin *et al.*, *Hyp. Int.* **82**, 373 (1993).
- [62] V. E. Markushin, E. I. Afanasieva, and C. Petitjean, *Muon Catal. Fusion* **7**, 155 (1992).
- [63] A. Adamczak, *Hyp. Int.* **82**, 91 (1993).
- [64] M. P. Faifman, *Muon Catal. Fusion* **2**, 247 (1988).
- [65] L. I. Men'shikov, *Proceedings of μ CF-95, Dubna, Russia, 1995.*
- [66] F. Mulhauser *et al.*, submitted to *Phys. Rev. A*.
- [67] J. Woźniak *et al.*, Study of muonic hydrogen transport in TRIUMF Experiment 742 by Monte Carlo method, *Proceedings of μ CF-95, Dubna, Russia, 1995.*
- [68] V. G. Zinov *et al.*, Measurement of spin and temperature dependence of $dd\mu$ molecule formation rate in gaseous, liquid, and solid deuterium, *Proceedings of μ CF-95, Dubna, Russia, 1995.*
- [69] R. Jacot-Guillarmod, (private communication).
- [70] R. Jacot-Guillarmod *et al.*, *Hyp. Int.* **82**, 501 (1993).
- [71] G. M. Marshall *et al.*, Time-of-flight measurement of resonant molecular formation in Muon Catalyzed dt fusion, *Proceedings of μ CF-95, Dubna, Russia, 1995.*
- [72] L. I. Man'shikov *et al.*, *Zh. Eksp. Teor. Fiz.* **92**, 1173 (1987), [*Sov. Phys. JETP*, **65**(4), 656-663 (1987)] (Although spelled Man'shikov in this journal, the more common translation of the author's name is Men'shikov).
- [73] A. M. Lane, *Phys. Lett. A* **98**, 337 (1983).

Appendix A

Notation for the Rates

Like all branches of physics, μCF has many different notations conventions. A notation system based closely on the work of Men'shikov [72] and Zmeskal [24] has been adopted. In general, a rate λ is made from a cross section σ via $\lambda = \sigma v N$ where v is the velocity of the interacting bodies and N is the number density of target particles. For experiments in hydrogen, where different experiments use very different conditions of concentration and density, the convention has been adopted of expressing results with respect to unit concentration, $c = 1$, and the nominal liquid density of hydrogen, $N_0 = 4.25 \times 10^{22} \text{ cm}^{-3}$. The experimental density is given as a product ϕN_0 , where ϕ is the relative density. Thus the reduced rates here are related to the measured rates via

$$\frac{\lambda_{\text{measured}}}{c\phi} = \lambda_{\text{reduced}} = \sigma v N_0.$$

The following symbols will be used:

- λ_0 : The muon decay rate in free space, $= 0.455160(8) \mu\text{s}^{-1}$.
- λ_z : The transfer rate to high-Z contaminating atoms.
- λ_f : Fusion rate from $J = \nu = 1$ rovibrational state of a $d\mu d$ molecule.
- λ_{FS} : Formation rate of a $d\mu d$ molecule in spin state S from μd in the hyperfine state F .
- $\lambda_{FF'}$: Spin flip rate from state F to state F' due to processes other than resonance molecular scattering.
- $\Gamma_{SF'}$: The decay rate for a $d\mu d$ muonic molecule of spin S into μd with hyperfine state F' .
- Γ_S : The decay rate for $d\mu d$ of spin S into any of the entrance channels:

$$\Gamma_S = \sum_{F'} \Gamma_{SF'}.$$

- λ_{pd} : The rate for the transfer process $\mu p + D_2 \rightarrow \mu d(43.3 \text{ eV}) + p(91.4 \text{ eV}) + dee$.
- $\lambda_{p\mu p}$: Formation rate of a $p\mu d$ molecule.
- β_s and β_p : The branching ratios for fusion in the $d+d$ reaction from either the s wave or p wave initial state to produce neutrons in the final state.

$$\beta_l := \frac{(d+d)_{l\text{ wave}} \rightarrow n + {}^3\text{He}}{(d+d)_{l\text{ wave}} \rightarrow \text{Anything}} \quad (\text{A.1})$$

- P_s : The measure of the probability of s wave bound state formation from the non-resonant formation process. See the entry for β_F below.

For the measurements considered here, the above rates, each associated with a single physical process, are not the best parametrizations. For example, it is impossible to know the spin S of a $d\mu d$ molecule when it is formed. Such a molecule could then fuse to release a detectable fragment, or decay into a μd state ($\Gamma_{SF'}$) thus imitating the spin flip reaction $\lambda_{FF'}$. Averaging over the real physical processes to produce effective rates is the practical approach to the problem and leads to the two-node approximation of the kinetics. The effective rates and their composition are as follows.

- $\tilde{\lambda}_f$: The effective fusion rate for resonantly formed $d\mu d$. For resonant $d\mu d$ formation, the fusion channel must compete with the resonance scattering channel Γ_S (the so called and somewhat misnamed *back decay*) and so the sum of the deexcitation rates which eventually lead to fusion of the $d\mu d$ must be compared to Γ_S [73]. The exchange symmetry of the dd system excludes the normally rapid electric dipole transition as a deexcitation mechanism. The comparison of widths of the decay channels of the $[(d\mu d)dee]$ become more important since the normally dominant $E1$ transition is missing.

A resonantly formed $d\mu d$ is initially in the $J = \nu = 1$ state where p wave fusion occurs at a rate of $440 \mu s^{-1}$ and deexcitation to the $\nu = 0$ state occurs at a rate of $20 \mu s^{-1}$ (once deexcitation to the $\nu = 0$ state has occurred, fusion occurs at a rate of $1500 \mu s^{-1}$). For the calculations here $\tilde{\lambda}_f = 460 \mu s^{-1}$, a value composed of the direct $\nu = 1$ fusion rate, and the $\nu = 0$ deexcitation rate [24]. Any contribution to the deexcitation rate due to solid state effects has not yet been investigated. The value of $\tilde{\lambda}_f$ is important since it enters into the equations below for the effective rates of formation [Eq. (A.2)] and spin flip [Eq. (A.3)].

- $\tilde{\lambda}_F$: The reduced rate of formation of $d\mu d$ molecules from a μd atom in the hyperfine state F . It represents molecular formation that leads to fusion and is composed of the nonresonant formation rate and the fraction of resonantly formed molecules which

successfully fuse instead of scattering as characterized by Γ_S .

$$\tilde{\lambda}_F = \lambda_{nr} + \sum_S \lambda_{FS} \frac{\tilde{\lambda}_f}{\tilde{\lambda}_f + \Gamma_S} \quad (\text{A.2})$$

- $\tilde{\lambda}_{FF'}$: The reduced hyperfine transition rate from state F to F'. The regular scattering transitions are strongly enhanced by the Γ_S decay branch of the molecular formation reaction.

$$\tilde{\lambda}_{FF'} = \lambda_{FF'} + \sum_S \lambda_{FS} \frac{\Gamma_{SF'}}{\tilde{\lambda}_f + \Gamma_S} \quad (\text{A.3})$$

- β_F : A parametrization of the branching ratio for $d\mu d$ molecules formed from a μd in hyperfine state F where β_F is given by:

$$\beta_F = \frac{\mu d_F + D_2 \rightarrow \mu + {}^3\text{He} + n}{(\mu d_F + D_2 \rightarrow \mu + p + t) + (\mu d_F + D_2 \rightarrow \mu + {}^3\text{He} + n)}. \quad (\text{A.4})$$

Since a μd_F is expected to generate $d\mu d$ molecules in a distribution of angular momentum states dependent on F , and the branching ratio for the fusion reaction depends on the angular momentum state, the branching ratios for the different hyperfine states F will differ. The β_F 's are convenient parameters when writing the kinetics, and are composed of the more fundamental s and p wave branching ratios, along with the ratio of s to p wave bound state formation. The nonresonant fusion will lead to a distributed population of s and p wave $d\mu d$ bound states which will produce fusion products reflecting the weighting of the s and p wave branching ratios. Resonance formation always produces the p wave molecular state.

$$\beta_F = \frac{\lambda_{nr}}{\tilde{\lambda}_F} [P_s \beta_s + (1 - P_s) \beta_p] + \frac{\tilde{\lambda}_F - \lambda_{nr}}{\tilde{\lambda}_F} \beta_p. \quad (\text{A.5})$$

The reduced rates approach above has changed the basically unmeasurable physical parameters ($\tilde{\lambda}_f$, $\lambda_{FF'}$, λ_{FS} , and $\Gamma_{SF'}$) into parameters ($\tilde{\lambda}_F$ and $\tilde{\lambda}_{FF'}$) which can be used in a kinetics fit to time spectra. It should be noted, however, that extracting physical rates from the reduced rates makes one sensitive to the assumptions in the spin sums.

Appendix B

Matrix Exponentiation

This section is added for completeness and can be skipped if the details of the solution method are uninteresting to the reader.

Presented with the task of exponentiation a matrix, one needs the decomposition of the matrix into the following form:

$$A = PUP^{-1}$$

where A is the matrix, U is the diagonal matrix of eigenvalues, $U_{ij} = L_i\delta_{ij}$, and P is the matrix composed of eigenvectors. The exponentiation can be examined in terms of the power series expansion from which the following relation is trivially derived:

$$e^A = Pe^UP^{-1}.$$

Further examination of the power-series representation of the exponent is sufficient to show that for a matrix $a_i\delta_{ij}$, the exponent is simply $(\exp a_i)\delta_{ij}$.

For the matrix presented in Eq. (2.3) the eigenvalues have already been presented [Eq. (2.8)] so we have

$$U = \begin{bmatrix} L_{\frac{3}{2}} & 0 \\ 0 & L_{\frac{1}{2}} \end{bmatrix}$$

and hence

$$e^U = \begin{bmatrix} e^{L_{\frac{3}{2}}} & 0 \\ 0 & e^{L_{\frac{1}{2}}} \end{bmatrix}.$$

The matrices of eigenvectors and its inverse can be found after some algebra and are:

$$P = \begin{bmatrix} \frac{B}{\sqrt{B^2 + (L_{\frac{3}{2}} + A)^2}} & \frac{B}{\sqrt{B^2 + (L_{\frac{1}{2}} + A)^2}} \\ \frac{CB}{(L_{\frac{3}{2}} + D)\sqrt{B^2 + (L_{\frac{3}{2}} + A)^2}} & \frac{CB}{(L_{\frac{1}{2}} + D)\sqrt{B^2 + (L_{\frac{1}{2}} + A)^2}} \end{bmatrix} \quad (\text{B.1})$$

$$P^{-1} = \frac{\sqrt{\left[B^2 + \left(L_{\frac{3}{2}} + A\right)^2\right] \left[B^2 + \left(L_{\frac{1}{2}} + A\right)^2\right]}}{B \left(L_{\frac{3}{2}} - L_{\frac{1}{2}}\right)} \begin{bmatrix} \frac{-CB}{\left(L_{\frac{1}{2}} + D\right) \sqrt{B^2 + \left(L_{\frac{1}{2}} + A\right)^2}} & \frac{B}{\sqrt{B^2 + \left(L_{\frac{1}{2}} + A\right)^2}} \\ \frac{CB}{\left(L_{\frac{3}{2}} + D\right) \sqrt{B^2 + \left(L_{\frac{3}{2}} + A\right)^2}} & \frac{-B}{\sqrt{B^2 + \left(L_{\frac{3}{2}} + A\right)^2}} \end{bmatrix}. \quad (\text{B.2})$$

Armed with the above it is relatively easy to find the solutions for \vec{N} via the relation

$$\vec{N}(t) = P e^{Ut} P^{-1} \vec{N}(t=0)$$

remembering that the eigenvalues have the relations

$$\left(L_{\frac{3}{2}} + D\right) \left(L_{\frac{1}{2}} + D\right) = -BC$$

and

$$\left(L_{\frac{3}{2}} + A\right) \left(L_{\frac{3}{2}} + D\right) = BC.$$

Appendix C

Resolution Functions

The experimental resolution of the detector used to see the fusion fragments must be taken into account in any fits done to data, for that purpose we convolute the expected data shape with a Gaussian resolution function and introduce two fitting parameters, time zero (via a step function Θ), and the resolution width. All of the time functions used in the work presented here were exponentials, so the general form of the convolution for an exponential $e^{\lambda t}$ was:

$$I(t) = \int_{-\infty}^{\infty} d\tau \frac{\Theta(\tau - t_0)}{\sqrt{2\pi\sigma^2}} e^{\lambda\tau} \exp\left[-\frac{(\tau - t)^2}{2\sigma^2}\right] \quad (\text{C.1})$$

where σ is the standard deviation of the detector resolution (related to the FWHM via $\text{FWHM} = \sigma\sqrt{8\ln 2}$) and the t_0 represents the time when the process becomes active.

Integrating:

$$I(t) = \frac{1}{2} \mathcal{E}\mathcal{R}\mathcal{F}\mathcal{C} \left[-\frac{(t - t_0) + \lambda\sigma^2}{\sqrt{2\sigma^2}} \right] \exp \left[\lambda(t - t_0) + \frac{(\lambda\sigma)^2}{2} \right] \quad (\text{C.2})$$

where $\mathcal{E}\mathcal{R}\mathcal{F}\mathcal{C}$ is the complementary error function defined by

$$\mathcal{E}\mathcal{R}\mathcal{F}\mathcal{C}(x) = \frac{2}{\sqrt{\pi}} \int_x^{+\infty} \exp(-x^2) dx. \quad (\text{C.3})$$

The total yield in the spectrum from t_i to t_f is obtained after integrating Eq. (C.2). The integrated form of the function is useful when fitting to data with time binning which is so wide that the value of the function is not adequately represented by its value at the midpoint of the bin (i.e., approximating the function as linear over the size of the bin is not adequate).

The function representing that integral is:

$$\begin{aligned} \int_{t_i}^{t_f} dt I(t) = & \frac{1}{2\lambda} \left\{ \mathcal{E}\mathcal{R}\mathcal{F}\mathcal{C} \left[-\frac{(t_i - t_0)}{\sqrt{2\sigma^2}} \right] - \mathcal{E}\mathcal{R}\mathcal{F}\mathcal{C} \left[-\frac{(t_f - t_0)}{\sqrt{2\sigma^2}} \right] \right. \\ & + \exp \left[\lambda(t_f - t_0) + \frac{(\lambda\sigma)^2}{2} \right] \mathcal{E}\mathcal{R}\mathcal{F}\mathcal{C} \left[-\frac{(t_f - t_0) + \lambda\sigma^2}{\sqrt{2\sigma^2}} \right] \\ & \left. - \exp \left[\lambda(t_i - t_0) + \frac{(\lambda\sigma)^2}{2} \right] \mathcal{E}\mathcal{R}\mathcal{F}\mathcal{C} \left[-\frac{(t_i - t_0) + \lambda\sigma^2}{\sqrt{2\sigma^2}} \right] \right\} \quad (\text{C.4}) \end{aligned}$$

Appendix D

Calibration Data

D.1 Neutron Detector Calibration

The neutron detectors were calibrated by a two point method, since the absolute calibration was not critically important to the experiment. The gamma sources ^{60}Co and ^{137}Cs were used. In addition, there was a strong background of 511 keV photons in the experimental area, and its spectrum was recorded as well to provide a check on the calibration.

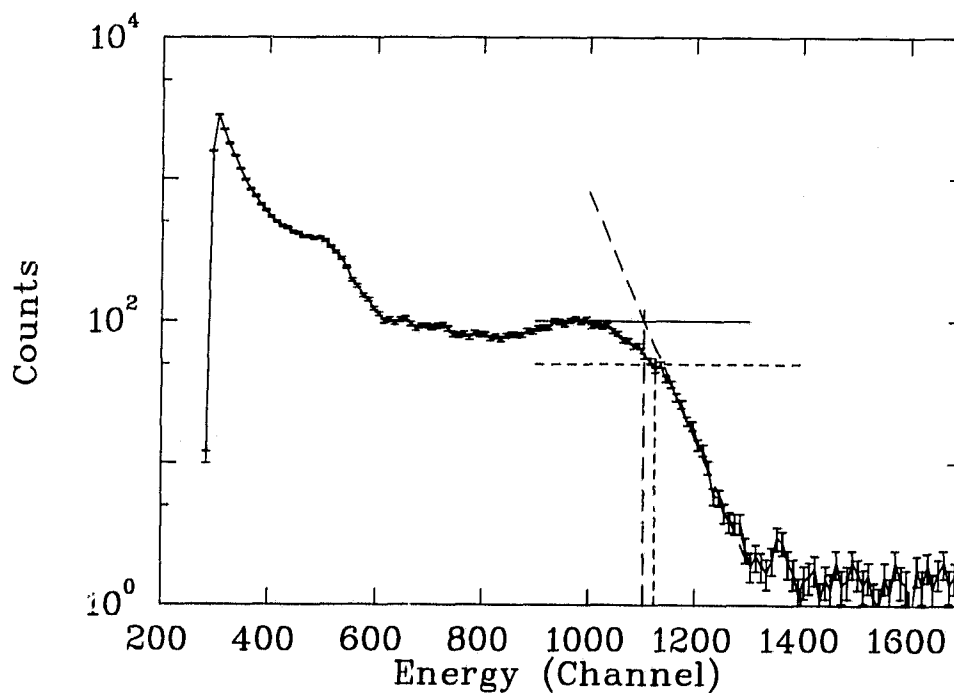


Figure D.1.1: The ^{60}Co photon energy spectrum as seen by the neutron detector. The lines indicate the method used to find the half-height intersection point.

Source	Energy	Compton Edge	Detector
^{60}Co	1173, 1332	963, 1118	1160
^{137}Cs	662	478	530
511 keV	511	341	420

Table XXI: Gamma source photon energies, Compton energies, and equivalent detector energies at the half-maximum intensity point. Energies are given in keV. Note that ^{60}Co has two lines of equal strength which are averaged to get the detector response.

As mentioned in the text, the effective energy of the sources in the detector was found after extensive Monte Carlo studies, and response curves of many different gamma sources. The source, its lines, the true Compton edge, and the energy of the edge in the detector are given in Table XXI.

The determination of the channel number corresponding to the half height of the effective compton edge was determined two ways as illustrated in Fig. D.1.1. The first method was simply to find the average peak height over the maximum region, plot a line at half that value and accept the intersection of the edge and the line as the channel. The second method was to fit a straight line to the edge and choose the intersection point of that line with the horizontal line defining the maximum (This algorithm works on logarithmic

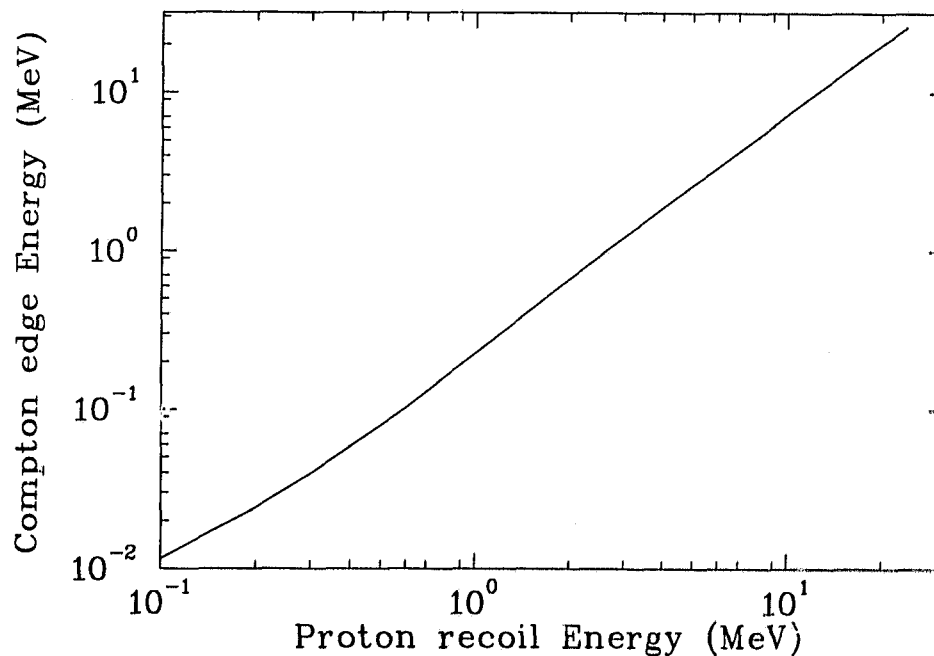


Figure D.1.2: A plot of the equivalent light output for NE-213 scintillator. The data are taken from Verbinski et al. [54].

plots, and is the “quick-and-dirty” method used during runtime). Both methods yield the same channel number to within 5%, which is acceptable since the energy calibration is not critically important to the measurement.

The equation for the gamma calibration of the detector is

$$E_{\gamma} = 1.23 \frac{\text{keV}}{\text{ch}} (\text{ch} - 231). \quad (\text{D.1})$$

The graph from Ref. [54], Fig. D.1.2, can be used to convert E_{γ} into the proton recoil energy (pulse height).

D.2 Silicon Detector Calibration

During the data collection in FEB92, calibration data were taken for the silicon detector by using a precision pulser signal sent to the detector preamplifier to measure the linearity of the device while an absolute scale was determined by the use of a small americium source. In this case, due to size and convenience, the americium source from a common household smoke detector was used. Sources of this type have heavy protective coatings on their surfaces, and do not provide a very accurate calibration scale. The more accurate method is to assume that the most energetic fusion proton seen is 3.02 MeV and use it as the scale reference.

Figure D.2.1 shows both the pulser data, and the ^{241}Am spectrum obtained during the FEB92 runtime. Table XXII shows the measured values for the centroids of the four pulser peaks. The ratio of the pulser peaks is assumed to be well known, so the centroid values of the peaks define a linear scale which allows the origin of the energy scale to be accurately found. The Fit 0 value given in the table, derived from the fit of line to the centroid channel versus pulser input, was then subtracted from the centroid value of the known energy peak (either source, or fusion protons) and from there the calibration equation was calculated.

The following calibration was obtained for the FEB92 setup using the 8 T fusion protons as the known signal (cf. Table XI, page 81):

$$E = 0.993(3) \frac{\text{keV}}{\text{channel}} (\text{channels} - 23(3)) \quad (\text{D.2})$$

Peak	centroid (channels)	Note
Pulser 30.00	1632.2(1)	$\sigma = 14$ Channels
Pulser 60.00	3235.0(1)	$\sigma = 13$ Channels
Pulser 90.00	4843(1)	$\sigma = 12$ Channels
Pulser 120.00	6454.0(1)	$\sigma = 12$ Channels
Pulser Fit 0	23(3)	
^{241}Am Source	4636(3)	Energy=4.55(10) MeV

Table XXII: Centroid values and widths from the FEB92 pulser data. The Fit 0 value indicates where the scale begins, the σ measures the intrinsic width of the electronics.

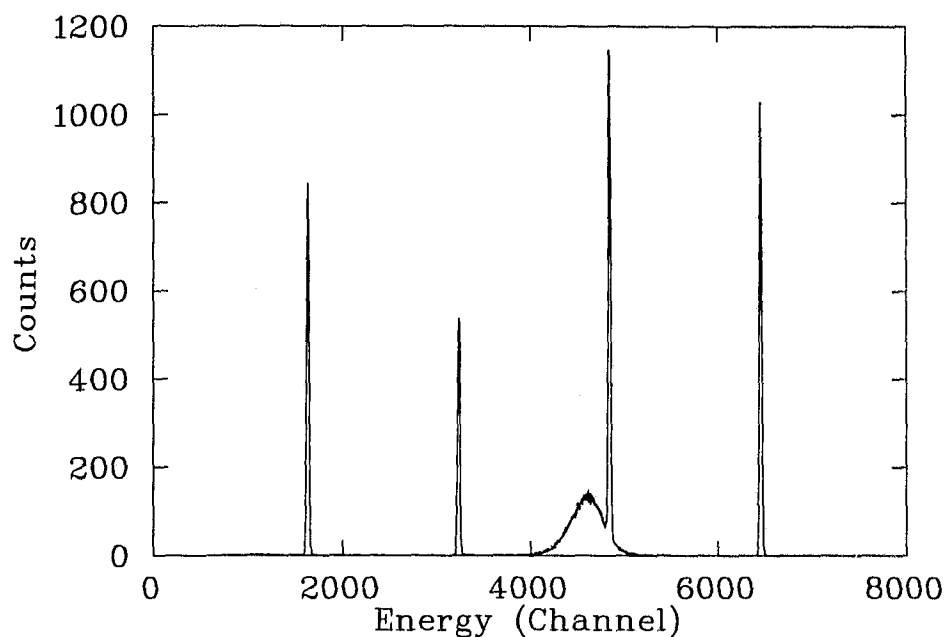


Figure D.2.1: *The pulser and americium spectrum in the silicon detector for the FEB92 run period.*

Using the source as the energy signal gave:

$$E = 0.99(2) \frac{\text{keV}}{\text{channel}} (\text{channels} - 23(3)) \quad (\text{D.3})$$

Based on the widths of the pulser peaks, the FWHM energy resolution was about 30 keV.

Likewise, the silicon detector in the AUG92 runtime had the following calibration:

$$E = 0.71(5) \frac{\text{keV}}{\text{channel}} (\text{channels} + 5(1)) \quad (\text{D.4})$$

However, for this particular configuration, the electronics contributed a detector resolution FWHM of about 170 keV.

Appendix E

List of Abbreviations

Table XXIII: Abbreviations used in the thesis.

1AT2	Beam line 1, Target # 2
ADC	Analogue-to-digital converter
AMP	Signal amplifier
ATT	Signal attenuator
\overline{BF}	Busy signal fanout
cl	Confidence level (%); Probably of a worse χ^2 in a fit
CLF	Clear pulse fanout
CnY(H/L)	Wirechamber n Y-coordinate High/Low time
CnZ(H/L)	Wirechamber n Z-coordinate High/Low time
CINH	Computer generated inhibit
CnF	Wirechamber n signal fanout
COIN	Signal coincidence module
CPINH	Clear Pulse Inhibit
del.e	Delay decay electron coincidence
del.tel	Delay decay electron coincidence with energy cut
DISC	Signal discriminator
DYN14	Dynode 14 from the neutron phototube
DS	Downstream target foil
E1Ni, E2Ni	Plastic scintillators in front of Ni (i=1,2)
EB	End of Busy
EEVG	End of Event Gate
EEVGF	End of event gate fan
EI	Extended computer inhibit
EVENA	End of event gate timing output
EVG	Event Gate
EVTO	Neutron detector charge veto
EVCL	Event Clear
EVTR	Event Trigger

continued on next page

FAN	Signal fanout
GMU	Good muon (no pileup during the event)
GN1	Good N1 anticoincidence
HINH	Hardware inhibit
LIN AMP	High quality spectroscopy amplifier
MINA	20 cm diameter Sodium Iodide crystal
N1, N2	Neutron detectors 1 and 2
1/N	Prescaled trigger
1/NF	Fanout module for the above
NIM	Nuclear Instrument Module; logic levels 0 mA=off, -16 mA=on
PSD	Pulse shape discrimination
PSD-5010	Pulse shape discrimination hardware module
PSD SHIFT	Pulse shape discrimination DC voltage level adaptor
PUG	Pile up gate
T1	Particle entry scintillator
TIAMP	Particle entry energy loss amplifier
TIATT	Particle entry energy loss attenuator
TIHI	Particle entry with high threshold
TIIF	Particle entry signal fanout
TBI	Particle entry, no busy, no inhibits
TBIF	Signal fanout for the above
TBS	Tritium barrier space
TF AMP	Timing filter amplifier
Tl	Torr x liter
TPn	Trigger pulse from detector n
TRGn	Trigger signal n
TRGF	Trigger signal collection and fanout
TTL	Transistor-Transistor Logic: 5 V logic levels
US	Upstream target foil
WCINH	Wire chamber high-voltage-failure inhibit

Vita

Surname: Knowles
Given Names: Paul Evan
Place of Birth: Windsor, Nova Scotia, Canada
Date of Birth: 15th of September, 1968

Educational Institutions Attended:

1990-1995 University of Victoria, Victoria, British Columbia.

1986-1990 Acadia university, Wolfville, Nova Scotia

1990 Granted the degree of Bachelor of Science with Honours in Physics

Honours and Awards:

President's scholarship	University of Victoria	1993-94
NSERC PGSB	University of Victoria	1992-94
Carl H. Westcott Memorial Fellowship	University of Victoria	1992-93
NSERC PGS2	University of Victoria	1991-92
President's scholarship	University of Victoria	1991-92
NSERC PGS1	University of Victoria	1990-90
President's scholarship	University of Victoria	1990-91
R. M. Pearce Memorial scholarship	University of Victoria	1990-91
NSERC undergraduate research grant	TRIUMF	1990
Named a University Scholar	Acadia University	1990
Bronze medal in Physics	Acadia University	1990
Beveridge scholarship	Acadia University	1989-90
NSERC undergraduate research grant	TRIUMF	1990
Kennith A. Killam Scholarship	Acadia University	1988-89
Ralph M. Hunt memorial prize for Physics	Acadia University	1988-89
NSERC undergraduate research grant	Acadia University	1988
Lieutenant Governor's medal	Nova Scotia	1986

a) Publications and refereed conference proceedings (published or accepted):

1. P.E. Knowles, *et al.*, A Windowless Frozen Hydrogen Target System, accepted for publication in Nuclear Instruments and Methods, June 30th, 1995.
2. P.E. Knowles, *et al.* Producing μd and μt in vacuum, Hyperfine Interactions **82**, 521-527 (1993). [presentation by P.E. Knowles at the INTERNATIONAL WORKSHOP ON MUON CATALYZED FUSION, μCF -92, Uppsala, Sweden, June 28-July 3, 1992]
3. R. Jacot-Guillarmod, *et al.*, Muon transfer from hot muonic hydrogen atoms to neon, Hyperfine Interactions **82**, 501-506 (1993). [presentation by R. Jacot-Guillarmod at the INTERNATIONAL WORKSHOP ON MUON CATALYZED FUSION, μCF -92, Uppsala, Sweden, June 28-July 3, 1992]
4. G.M. Marshall, *et al.*, Experiments with energetic μd and μt emitted from solid hydrogen, Hyperfine Interactions **82**, 529-538 (1993). [TRI-PP-92-118] [invited presentation by G.M. Marshall at the INTERNATIONAL WORKSHOP ON MUON CATALYZED FUSION, μCF -92, Uppsala, Sweden, June 28-July 3, 1992]
5. G.M. Marshall, *et al.*, Reactions of muonic hydrogen isotopes in *The Future of Muon Physics*, eds. K. Jungmann, V.W. Hughes, and G. zu Putlitz, Z. Phys. C - Particles and Fields **56**, S44-S47 (1992). [TRI-PP-91-70] [presentation by G.M. Marshall at the WORKSHOP ON THE FUTURE OF MUON PHYSICS, Heidelberg, May 7-9, 1991]

b) Other publications, including those submitted or in press:

6. F. Mulhauser, *et al.*, Measurement of Muon Transfer from Proton to Triton and $pp\mu$ Molecular Formation in Solid Hydrogen, submitted to Phys. Rev. A (in Review).
7. P.E. Knowles, *et al.* Muon Catalyzed Fusion in Deuterium at 3 K, To be published in Hyperfine Interactions. [presentation by P.E. Knowles at the INTERNATIONAL SYMPOSIUM ON MUON CATALYZED FUSION, μCF -95, Dubna, Russia, June 19-24, 1995]

c) Completed and unpublished material, including nonrefereed publications and presentations:

8. G.M. Marshall, *et al.*, Time of flight spectroscopy with muonic hydrogen, LAMPF Report LA-12698-C, compiled by M. Leon, Los Alamos, NM, 221-227 (1994). [TRI-PP-93-76] [invited presentation by G.M. Marshall at the WORKSHOP ON LOW ENERGY MUON SCIENCE, LEMS-93, Santa Fe, NM, April 5-8, 1993]
9. R. Jacot-Guillarmod, *et al.* Detection of hot muonic atoms emitted in vacuum using x-rays, in *Muonic Atoms and Molecules*, eds. L.A. Schaller and C. Petitjean, 261-266, Birkhäuser Verlag, Basel (1993). [presentation by R. Jacot-Guillarmod at the ASCONA WORKSHOP ON MUONIC ATOMS AND MOLECULES, Ascona, April 5-9, 1992]
10. G.M. Marshall, *et al.*, Hot muonic deuterium and tritium from cold targets, in *Muonic Atoms and Molecules*, eds. L.A. Schaller and C. Petitjean, 251-260, Birkhäuser Verlag, Basel (1993). [TRI-PP-92-87] [invited presentation by G.M. Marshall at the ASCONA WORKSHOP ON MUONIC ATOMS AND MOLECULES, Ascona, April 5-9, 1992]

Partial Copyright Licence

I hereby grant the right to lend my dissertation to users of the University of Victoria Library, and to make single copies only for such users, or in response to a request from the Library of any other university or similar institution, on its behalf or for one of its users. I further agree that permission for extensive copying of this dissertation for scholarly purposes may be granted by me or a member of the university designated by me. It is understood that copying or publication of this dissertation for financial gain shall not be allowed without my written permission.

Title: **Muonic Processes in Solid Hydrogen Films**

Author: Paul Knowles

/ _____
January 22nd, 1996

(Date)